UC Berkeley
UC Berkeley Electronic Theses and Dissertations

Title
Mechanical Behaviors of Alloys From First Principles

Permalink
https://escholarship.org/uc/item/1xv2n9dw

Author
Hanlumyuang, Yuranan

Publication Date
2011

Peer reviewed|Thesis/dissertation

Mechanical Behaviors of Alloys From First Principles

by

Yuranan Hanlumyuang

A dissertation submitted in partial satisfaction of the
requirements for the degree of
Doctor of Philosophy

in

Materials Sciences and Engineering

in the

Graduate Division

of the

University of California, Berkeley

Committee in charge:

Professor Daryl C. Chrzan, Chair
Professor John W. Morris, Jr.
Professor Tarek I. Zohdi

Fall 2011

Mechanical Behaviors of Alloys From First Principles

Copyright 2011
by
Yuranan Hanlumyuang

Abstract

Mechanical Behaviors of Alloys From First Principles

by

Yuranan Hanlumyuang

Doctor of Philosophy in Materials Sciences and Engineering

University of California, Berkeley

Professor Daryl C. Chrzan, Chair

Several mesoscale models have been developed to consider a number of mechanical properties and microstructures of Ti-V approximants to Gum Metal and steels from the atomistic scale. In Gum Metal, the relationships between phonon properties and phase stabilities are studied. Our results show that it is possible to design a BCC (β-phase) alloy that deforms near the ideal strength, while maintaining structural stability with respect to the formation of the ω and α'' phases. Theoretical diffraction patterns reveal the role of the soft $N-$point phonon and the BCC$\rightarrow$HCP transformation path in post-deformation samples. The total energies of the path explain the formation of the giant faults and nano shearbands in Gum Metal.

In the study of steels, we focus on the carbon-solute dislocation interactions. The analysis covers the Eshelby's model of point defects and first principles calculations. It is argued that the effects of chemistry and magnetism, omitted in the elasticity model, do not make major contributions to the segregation energy. The predicted solute atmospheres are in good agreement with atom probe measurements.

To my parents, sisters, and brother, who made it all worthwhile...

Contents

List of Figures

List of Tables

Acknowledgments

I have had tremendous support throughout my graduate studies. This research project represents the work of many individuals. First of all, I want to thank Daryl C. Chrzan, my advisor, for introducing me to the field of computational materials science. His guidance and patience provided the right atmosphere in order for me to explore my interest while producing high-quality research. My interactions with him have benefited me immensely. I would also like to thank my dissertation committee, Prof. John W. Morris, Jr. and Prof. Tarek I. Zohdi for taking the time to review this work.

My credit goes to the many members of the Chrzan research group. Shuo Chen, Cosima Boswell, and Carolyn Sawyer gave me insightful comments and invaluable assistances on numerous occasions. The dissertations of Elif Ertekin, Mark H. Jhon, and Tianshu Li have guided me several points in the course of my study. I also own a special thank to Matthew P. Sherburne, his research and administrative skills have helped me since my first day at Berkeley.

I would also like to extend my gratitude to Rohini Sankaran and Elizabeth A. Withey. Their excellent experimental data has given me much excitement in the field.

Lastly, my parents, brother and sisters have been a source of encouragement throughout my education, especially in the last few months. Their love and support are an integral part to all my success.

Chapter 1

Introduction

Much work has been done in predicting mechanical properties of alloys from the top-down or the microscale approach. Dislocation theory is capable of explaining plasticity [1]. The micromechanics theory of inclusions and inhomogeneities is able to estimate the stress and strain profiles around the precipitates [2, 3, 4]. Elasticity theory predicts the the stress distribution near the singularity of a crack tip, enabling the idea of toughening the material by adjusting the energy release rate.

From the bottom-up perspective, solid-state physicists and chemists have modeled successfully the atomic structures of materials. First principles analysis and molecular dynamics have become practical tools for exploring small-scale systems. These techniques are based on a few fundamental approximations to the many-body problem of interacting electrons and protons; for example, (1) the Born-Oppenheimer approximation assumes the immobile nuclei in comparison to the electrons, (2) the electronic ground state is determined by the density functional methods [5], (3) the exchange-correlation energy of the electrons are estimated by either the generalized gradient approximation or the local density approximation and beyond, and (4) the potentials of the nuclei is represented by pseudopotentials, determined by the atomic numbers and only a few other physical inputs. Over the past fifty years, atomistic models have yielded satisfying descriptions of the electronic and chemical properties of new semiconductor devices, phonon and energy transport, and the origins of exotic nanostructures such as carbon nanotube, graphene, etc. However, despite a few problems such as as the elastic constants, the elastic instability and ideal strength of elemental materials, much of the relationship of the atomistic models to large scale mechanical properties and microstructures remains unclear.

The connection between atomistic models and the mechanical properties and microstructures of materials is an interesting area of exploration. Obviously, we cannot examine the vast arrays of problems existing in the mechanics community, but only a few representative ones. The class of materials and problems considered in this dissertation are motivated by industrial research; Gum Metal (Ti-Nb based alloys) developed by Toyota [6], and steels for ExxonMobil [7]. For Gum Metal, the mechanical behaviors and microstructures relating to

the phase stabilities and phonons are considered. In the case of steels, the scope includes the dislocation-carbon interactions and the solute distributions at different temperatures.

Gum Metal is a body-centered-cubic (BCC) Ti-Nb based alloy that exhibits many super properties, such as a large elastic limit, large ductility, and high strength [8]. These properties are obtained by alloying such that the number of valence electrons per atom is about 4.3, and are realized after substantial coldworking has been applied. Surprisingly, a close examination of the post-deformation samples reveals no obvious dislocation activity. These observations lead to the creators of Gum Metal to conclude that Gum Metal is a bulk material that deforms at ideal strength. If so, Gum Metal represents a new type of structural alloy. The novelty of Gum Metal arises from the rich relationship among phase stability, elastic anisotropy, and phonons in the material.

Mechanical properties of ferritic Fe-C alloys such as yield points, ductilities, and toughnesses are influenced by the solute atmosphere around dislocations. In addition to lattice friction, solutes may exert pinning forces that further impede dislocation plasticity. Sharp yield points or strain aging results from static atmosphere at low temperature, while mobile atmospheres at intermediate temperatures result in dynamics strain aging or the Portevin-Le Chatelier effect [1]. Designing new ferritic alloys or other materials depends on the accuracy of probing and predicting the properties of the solute atmosphere, a technique which has been made possible only recently by the seminal development of atom probe tomography [9].

It is known that opportunities to analyze mechanical theory from atomic level are rare because phenomena in real materials involve multiple length and time scales. However, for Gum Metal it has already been suggested that the mechanical behavior is governed by the ideal strength, a material property that can be studied exclusively from first principles. The ideal strength of Gum Metal is represented well by the average Ti-V approximant within the virtual-crystal approximation [6]. In the case of steels, atom probe tomography allows direct imaging of dislocations and the encompassing solute atmosphere, a quantity which can be computed from a statistical mechanics model if solute-dislocation interactions are known.

The central theme of this dissertation is to bridge the macroscopic behaviors to atomistic calculations in order to describe certain aspects of Gum Metal and steels. The first principles calculations in this work are largely motivated by the fundamental understanding at the mesoscale. From this intermediate scale, physical descriptions are then used to describe materials behaviors at the larger scale. The theoretical results in this dissertation are tested by a variety of suitable methods, including comparative studies, experiment, literature, and empirical models whenever possible. Despite the experiments, the pool of validating methods only serves as self-consistent checks for the models.

Some of this dissertation is devoted to review. The background knowledge for this work ranges over a broad literature. The rederivations presented throughout this work are mainly aimed to consolidate the notation used in different fields. The author has tried to section the text, and provide references to aid further study and distinguish new contributions to the body of knowledge in structural materials.

Chapters 2-4 deal with Gum Metal. Chapter 2 focuses mainly on the properties of

phonons in the material. First, a harmonic model is outlined in conjunction with an application of group theory. The model provides a framework to obtain the phonon dispersion relations from first principles. Secondly, phonon dispersions a variety of Ti-V approximants to Gum Metal are computed. The analysis of phases initiated by different phonon modes is presented. Lastly, a clue to the unique microstructures of the post-deformation Gum Metal samples is discussed.

Chapters 3 and 4 are devoted to the study of the Burgers transformation path in Gum Metal. The suitable tool to study the solid-solid phase transformation is the nudged-elastic-band method (NEB) [10]. The theoretical background of the method is presented in Chapter 2. The beginning of Chapter 2 reviews the concepts of the NEB. Then, from the quantum theory of stresses and forces, it is argued that the parameters needed for the NEB can be obtained straightforwardly from existing total energy calculation packages. Chapter 3 first focuses on the validation of the NEB by comparative study of the Bain path in Gum Metal, and the Burgers path in sodium. It closes with the discussion on the Burgers path in Gum Metal and its relation to the microstructure of the post-deformation samples.

In Chapter 5, a study of dislocation-solute interaction in steels is presented. The chapter starts with a summary of earlier similar work from the literature. The mesoscopic view (empirical potential study) of the problem is then given in comparison to the atomistic approach. The importance of magnetic/electronic contributions to the interaction energy between the dislocations and carbon atoms is studied. Lastly, the first principles predictions of the solute atmosphere is compared with experimental results.

From the atomic scale, we are able to offer insights into mechanical properties of alloys. Nevertheless, we have not yet exhausted all the problems; some aspects remain to be addressed more extensively. Fundamentally, we manage to start from first principles and deduce workable explanations to a number of mechanical properties in Gum Metal and steels. By limiting the assumptions going into the models, we believe this work has found a solid ground for further study. All the theoretical methods developed are not limited to Gum Metal and steels. We envision the use of these tools to gain insights into plasticity, phase transformations, and kinetics of other structural materials.

Chapter 2

Phonons in Gum Metal

2.1 Introduction to Gum Metal

Key features of Gum Metal deformation [8] have led further experimental and theoretical investigations. (1) Dislocations are not activated during the deformation. Post-deformation samples reveals no substantial dislocation activity. (2) The deformation is reportedly not accompanied by phase transformation [8, 11], and (3) deformation in Gum Metal progresses by formation of giant faults formed near the plane of the maximum shear stress, and not on any BCC slip systems. Instead high-magnification TEM images of cold-worked specimens reveal local disturbances along the $\langle 111 \rangle$ direction [8, 12]. The size of the disturbances is in the order of 1-2 nm. One of the goals of this dissertation is to gain theoretical insight into these features.

The elastic constant $C_{11} - C_{12}$ of Gum Metal is low compared to that of conventional BCC metals [6]. The ideal shear strength for a shear in a [111] direction of a BCC crystal is given by

$$\tau \approx 0.11 \frac{3C_{44}(C_{11} - C_{12})}{C_{11} - C_{12} + 4C_{44}}. \tag{2.1}$$

The ideal shear strength scales directly with $C_{11} - C_{12}$. For normal metals, the ideal strengths are several dozen times the actual strength, where as for Gum Metal it is estimated to be so small as to be comparable to the actual strength. Hence Gum Metal is believed to deform at the ideal strength.

However, recent *in situ* synchrotron X-ray diffraction and transmission electron microscopy offer an alternative conclusion that the β-Ti alloy Gum Metal undergoes a reversible stress-induced face-centered-orthorhombic $\alpha'' -$ transformation [13]. If this conclusion is correct, the deformation of Gum Metal is not particularly novel as originally proposed by the creators. A theoretical analysis of the elastic energy associated with the $\beta(\text{BCC})$-α'' phase under loads shows that while the transformation is favored in the single crystal pulled in the $\langle 110 \rangle$ direction, it is suppressed along the other directions and in the polycrystalline samples

[11]. Furthermore, the study of the compression of nano-pillars using *in situ* transmission electron microscopy reveals no correlation between the intensity of the diffracted beams of the α''-phase and the load versus displacement curve [14, 15]. Hence, it remains plausible that Gum Metal deforms at ideal strength.

The relationship between elastic anisotropy, phase transformation, and plastic deformation of Gum Metal is an interesting area of exploration. Phonon dispersion relations shed light into the energy associated with lattice vibrations and the stability of the structure. The vibrational modes play a key role in the initiation of phase transition. Theoretically, the transformation path congruent with soft modes is more likely to occur.

The current trend in calculating phonon dispersion relations is to employ linear response theory [16], a method that quantum *ab inito* packages provide. However, this approach is challenging for Gum Metal due to the abundance soft modes. In this chapter, we calculate the phonon dispersions empirically using a harmonic model, incorporating parameters obtained from first principles.

There is an extensive array of literature describing the concepts of harmonic oscillations in crystals [17, 18, 19, 20, 21]. However, only few of these focuses on the symmetry relations of the vibrational modes to the elastic anisotropy [22, 20]. For completeness, some of the developments are rederived here, putting the emphasis on various symmetry relations. It is later shown that the first principles calculations provide necessary parameters to obtain reasonable phonon dispersion relations of Ti-V approximants to Gum Metal. To check for consistency, the dispersion relations over a range of compositions are calculated. The theoretical diffused scattering patterns from the calculated dispersions agree with a transmission electron diffraction pattern.

In the last section of this chapter, the nature of the vibrational modes leading to BCC-HCP, and BCC-ω transformations in Gum Metal are considered. The relationship of the phonons to the elastic anisotropy and phase stability is then discussed.

2.2 Vibrations in Solids

Some of the seminal developments of the vibrations in solids needed to obtain a phonon dispersion relation are presented in this section. More detail can be found textbooks and monographs, including those authored by Meradudin [18] Ashcroft and Mermin [23], Brüesch [20], and Feynman [21].

2.2.1 Elementary Introduction

Since an average BCC symmetry representation of Gum Metal is considered, the lattice of interest has one atom per unit cell. It is known that a system of N atoms requires $3N$ coordinates to fully explain all the vibrational modes. The number of normal mode is then

$3N$. The atomic position of the ground state in terms of the lattice vectors $\mathbf{a}, \mathbf{b}$, and $\mathbf{c}$ are

$$\mathbf{R}(l, m, n) = l\mathbf{a} + m\mathbf{b} + n\mathbf{c} \equiv \mathbf{R} \tag{2.2}$$

where l, m, n is a triplet of integers. The vibrational modes displace the atoms to new positions by

$$\mathbf{r}(l, m, n) = \mathbf{R} + \mathbf{u}(l, m, n) \equiv \mathbf{R} + \mathbf{u}(\mathbf{R}). \tag{2.3}$$

The Hamiltonian of the this many-body problem is

$$\mathcal{H} = \frac{1}{2} \sum_{\mathbf{R}, \alpha} \frac{p_\alpha^2(\mathbf{R})}{2m} + \frac{1}{2} \sum_{\substack{\mathbf{R}, \mathbf{R}' \\ \alpha, \beta}} \mathcal{K}_{\alpha\beta}(\mathbf{R} - \mathbf{R}') u_\alpha(\mathbf{R}) u_\beta(\mathbf{R}'), \tag{2.4}$$

where

$$\mathcal{K}_{\alpha\beta}(\mathbf{R} - \mathbf{R}') = \frac{\partial^2 \mathcal{V}}{\partial u_\alpha(\mathbf{R}) \partial u_\beta(\mathbf{R}')}, \tag{2.5}$$

and $\mathcal{V}$ is the crystal potential. The second derivative of the potential only depends on the difference $\mathbf{R} - \mathbf{R}'$ by the translational symmetry of the crystal.

It is useful to define reduced units where the mass is incorporated into the definition of the displacement,

$$\mathcal{H} = \frac{1}{2} \sum_{\mathbf{R}, \alpha} \dot{u}_\alpha^2(\mathbf{R}) + \frac{1}{2} \sum_{\substack{\mathbf{R}, \mathbf{R}' \\ \alpha, \beta}} \mathcal{K}_{\alpha\beta}(\mathbf{R} - \mathbf{R}') u_\alpha(\mathbf{R}) u_\beta(\mathbf{R}'). \tag{2.6}$$

The equations of motion of this Hamiltonian are

$$\ddot{u}_\alpha(\mathbf{R}) = -\sum_{\mathbf{R}', \beta} \mathcal{K}_{\alpha, \beta}(\mathbf{R} - \mathbf{R}') u_\beta(\mathbf{R}') \tag{2.7}$$

The solution of the above differential equation is

$$u_\alpha(\mathbf{R}) = a_\alpha(\mathbf{q}) e^{-i\omega t} e^{i\mathbf{q} \cdot \mathbf{R}} \tag{2.8}$$

where $\mathbf{q}$ is a wavevector expressing the relative phases between unit cells. By substituting Eq.(2.8) into (2.7), we have

$$\omega^2 a_\alpha = \sum_\beta \left[\sum_{\mathbf{R}'} \mathcal{K}_{\alpha\beta}(\mathbf{R} - \mathbf{R}') e^{i\mathbf{q} \cdot (\mathbf{R}' - \mathbf{R})} \right] a_\beta, \tag{2.9}$$

which is the main eigenvalue problem defining the dispersion relation $\omega = \omega(\mathbf{q})$. Since the potential is invariant by the inversion symmetry, $\mathcal{K}_{\alpha\beta}(\mathbf{R} - \mathbf{R}') = \mathcal{K}_{\alpha\beta}(\mathbf{R}' - \mathbf{R})$. Also, by summing over $\mathbf{R}$ on both sides, and use $\sum_{\mathbf{R}, \mathbf{R}'} = N \sum_{\mathbf{R}}$

$$\omega^2 a_\alpha = \sum_\beta \left[\sum_{\mathbf{R}} \mathcal{K}_{\alpha\beta}(\mathbf{R}) e^{i\mathbf{q} \cdot \mathbf{R}} \right] a_\beta. \tag{2.10}$$

Let

$$\gamma_{\alpha\beta}(\mathbf{q}) = \sum_{\mathbf{R}} \mathcal{K}_{\alpha\beta}(\mathbf{R})e^{i\mathbf{q}\cdot\mathbf{R}}. \tag{2.11}$$

The matrix $\gamma_{\alpha\beta}$ is the *dynamical matrix*. The form of $\gamma_{\alpha\beta}$ is restricted further by the point group symmetries. We will explore the symmetry restrictions in the later section. For the moment, the eigenvalue problem is

$$\omega^2 a_\alpha = \sum_{\beta} \gamma_{\alpha\beta}a_\beta. \tag{2.12}$$

Hence, we must solve the 3×3 characteristic equation:

$$\det \|\gamma_{\alpha\beta} - \omega^2\delta_{\alpha\beta}\| = 0. \tag{2.13}$$

The translational symmetry reduces the dimension of $3N \times 3N$ eigenvalue problem to 3×3.

$$\omega^{(r)}(\mathbf{q}) = \omega_{\mathbf{q}}^{(r)}. \tag{2.14}$$

For a particular mode $\mathbf{q}$ and polarization (r), the motion is described by

$$u_\alpha^{(r)}(\mathbf{q}) = a_\alpha^{(r)}(\mathbf{q})e^{-i\omega_{\mathbf{q}}^{(r)}t}e^{i\mathbf{q}\cdot\mathbf{R}}. \tag{2.15}$$

The general solution is thus

$$u_\alpha(\mathbf{R}) = \sum_{\mathbf{q},r} \frac{C(\mathbf{q})}{\sqrt{N}}a_\alpha^{(r)}(\mathbf{q})e^{-i\omega^{(r)}(\mathbf{q})t}e^{i\mathbf{q}\cdot\mathbf{R}}. \tag{2.16}$$

In summary, the dispersion relation can be determined once the dynamical matrix is identified. This matrix relates to the stiffness of the harmonic potential approximation to the solid, hence it is dictated by symmetry. The next section exploits such symmetry properties and shows that, by the symmetry argument, many components of the dynamical matrix vanish.

2.2.2 Applications of Group Symmetry

The extensive study of the application of group theory to to a general crystal (a lattice with multiple basis) can be found in [18, 20]. Here, only the case of BCC crystal is considered while emphasizing on a more transparent index notation. Note that the final relations in Eq.(2.32) of this subsection are also listed without proof in [19]. We derive them here for completeness.

For a general crystal structure, the dispersion relation is determined by solving the eigenvalue-value problem of the the matrix in Eq.(2.11),

$$\gamma_{\alpha\beta}(\mathbf{q}) = \sum_{\mathbf{R}} \mathcal{K}_{\alpha\beta}(\mathbf{R})e^{i\mathbf{q}\cdot\mathbf{R}} = \mathcal{K}_{\alpha\beta}(\mathbf{0}) + \sum_{\mathbf{R}\neq\mathbf{0}} \mathcal{K}_{\alpha\beta}(\mathbf{R})e^{i\mathbf{q}\cdot\mathbf{R}} \tag{2.17}$$

where we center the origin at some lattice point and perform the sum over the nearest neighbors, next nearest neighbors, and so on. In this section, we consider the analytical form of $\mathcal{K}_{\alpha\beta}$ from group theory.

The main premise of group theory is that a symmetry operation $\hat{\mathcal{O}}$ on a solid leaves it invariant. Suppose $\hat{\mathcal{O}}$ consists of a lattice translation and a proper or improper rotation, denote by $\hat{\mathcal{T}}$ and $\hat{\Theta}$ respectively. Mathematically,

$$\hat{\mathcal{O}} = \hat{\Theta}\hat{\mathcal{T}}. \tag{2.18}$$

Operating $\hat{\mathcal{O}}$ on an actual position of atom results in

$$\begin{aligned}
\hat{\mathcal{O}}\mathbf{r} &= \hat{\Theta}\mathbf{r} + \mathcal{T} = \hat{\Theta}\mathbf{R} + \hat{\Theta}\mathbf{u} + \mathcal{T} \\
&= \hat{\mathcal{O}}\mathbf{R} + \hat{\Theta}\mathbf{u},
\end{aligned} \tag{2.19}$$

where $\mathcal{T} = m\mathbf{a} + n\mathbf{b} + o\mathbf{c}$ is a lattice vector. The vector $\hat{\mathcal{O}}\mathbf{R}$ is also a lattice vector since it is obtained by an operation in a space group of the solid.

Since the potential energy is invariant under a symmetry operation, we have

$$\begin{aligned}
\mathcal{V}[\{\mathbf{r}\}] &= \mathcal{V}[\{\hat{\mathcal{O}}\mathbf{r}\}], \quad \text{or} \\
\mathcal{V}[\{\mathbf{R} + \mathbf{u}(\mathbf{R})\}] &= \mathcal{V}[\{\hat{\mathcal{O}}\mathbf{R} + \hat{\Theta}\mathbf{u}\}].
\end{aligned} \tag{2.20}$$

Confining to the harmonic approximation, the Taylor series expansion of the right-hand side of Eq.(2.20) is

$$\mathcal{V} = \frac{1}{2} \sum_{\substack{\mathbf{R},\mathbf{R}' \\ \alpha,\beta}} \sum_{\kappa,\delta} \mathcal{K}_{\alpha\beta}(\hat{\mathcal{O}}\mathbf{R}, \hat{\mathcal{O}}\mathbf{R}')[\hat{\Theta}_{\alpha\kappa}u_\kappa(\mathbf{R})][\hat{\Theta}_{\beta\delta}u_\delta(\mathbf{R}')]. \tag{2.21}$$

Also, for left-hand side it is

$$\mathcal{V} = \frac{1}{2} \sum_{\substack{\mathbf{R},\mathbf{R}' \\ \kappa,\delta}} \mathcal{K}_{\kappa\delta}(\mathbf{R}, \mathbf{R}')u_\kappa(\mathbf{R})u_\delta(\mathbf{R}'). \tag{2.22}$$

By comparing Eq.(2.21) and (2.22), the invariance of the potential energy requires

$$\begin{aligned}
\mathcal{K}_{\kappa\delta}(\mathbf{R}, \mathbf{R}') &= \sum_{\alpha\beta} \hat{\Theta}_{\alpha\kappa}\hat{\Theta}_{\beta\delta}\mathcal{K}_{\alpha\beta}(\hat{\mathcal{O}}\mathbf{R}, \hat{\mathcal{O}}\mathbf{R}'), \quad \text{and} \\
\mathcal{K}_{\alpha\beta}(\hat{\mathcal{O}}\mathbf{R}, \hat{\mathcal{O}}\mathbf{R}') &= \sum_{\kappa\delta} \hat{\Theta}_{\alpha\kappa}\hat{\Theta}_{\beta\delta}\mathcal{K}_{\kappa\delta}(\mathbf{R}, \mathbf{R}').
\end{aligned} \tag{2.23}$$

Eq.(2.23) helps to eliminate some elements of the dynamical matrix. By applying the symmetry operation to the dynamical matrix $\mathcal{K}_{\alpha\beta}$, the number of parameters needed to determine the phonon dispersion relations reduce significantly as we shall see next.

Applying Eq.(2.23) to each atomic neighboring pair and denoting $\mathcal{K}(l,m,n) \equiv \mathcal{K}(l\mathbf{a} + m\mathbf{b} + n\mathbf{c})$, the force constant matrices of a BCC structure extending to the third-nearest neighbors are (A few examples of how to derive these matrices are shown in Appendix A),

$$\mathcal{K}(\frac{1}{2}, \frac{1}{2}, \frac{1}{2}) = \begin{pmatrix} -\mathcal{A}_1 & -\mathcal{C}_1 & -\mathcal{C}_1 \\ -\mathcal{C}_1 & -\mathcal{A}_1 & -\mathcal{C}_1 \\ -\mathcal{C}_1 & -\mathcal{C}_1 & -\mathcal{A}_1 \end{pmatrix}, \quad \mathcal{K}(-\frac{1}{2}, \frac{1}{2}, \frac{1}{2}) = \begin{pmatrix} -\mathcal{A}_1 & \mathcal{C}_1 & \mathcal{C}_1 \\ \mathcal{C}_1 & -\mathcal{A}_1 & -\mathcal{C}_1 \\ \mathcal{C}_1 & -\mathcal{C}_1 & -\mathcal{A}_1 \end{pmatrix}$$

$$\mathcal{K}(\frac{1}{2}, -\frac{1}{2}, \frac{1}{2}) = \begin{pmatrix} -\mathcal{A}_1 & \mathcal{C}_1 & -\mathcal{C}_1 \\ \mathcal{C}_1 & -\mathcal{A}_1 & \mathcal{C}_1 \\ -\mathcal{C}_1 & \mathcal{C}_1 & -\mathcal{A}_1 \end{pmatrix}, \quad \mathcal{K}(\frac{1}{2}, \frac{1}{2}, -\frac{1}{2}) = \begin{pmatrix} -\mathcal{A}_1 & -\mathcal{C}_1 & \mathcal{C}_1 \\ -\mathcal{C}_1 & -\mathcal{A}_1 & \mathcal{C}_1 \\ \mathcal{C}_1 & \mathcal{C}_1 & -\mathcal{A}_1 \end{pmatrix}$$

$$\mathcal{K}(1, 0, 0) = \begin{pmatrix} -\mathcal{A}_2 & 0 & 0 \\ 0 & -\mathcal{B}_2 & 0 \\ 0 & 0 & -\mathcal{B}_2 \end{pmatrix}, \quad \mathcal{K}(0, 1, 0) = \begin{pmatrix} -\mathcal{B}_2 & 0 & 0 \\ 0 & -\mathcal{A}_2 & 0 \\ 0 & 0 & -\mathcal{B}_2 \end{pmatrix}$$

$$\mathcal{K}(0, 0, 1) = \begin{pmatrix} -\mathcal{B}_2 & 0 & 0 \\ 0 & -\mathcal{B}_2 & 0 \\ 0 & 0 & -\mathcal{A}_2 \end{pmatrix}$$

$$\mathcal{K}(1, 1, 0) = \begin{pmatrix} -\mathcal{A}_3 & -\mathcal{C}_3 & 0 \\ -\mathcal{C}_3 & -\mathcal{A}_3 & 0 \\ 0 & 0 & -\mathcal{B}_3 \end{pmatrix}, \quad \mathcal{K}(1, 0, 1) = \begin{pmatrix} -\mathcal{A}_3 & 0 & -\mathcal{C}_3 \\ 0 & -\mathcal{B}_3 & 0 \\ -\mathcal{C}_3 & 0 & -\mathcal{A}_3 \end{pmatrix}$$

$$\mathcal{K}(0, 1, 1) = \begin{pmatrix} -\mathcal{B}_3 & 0 & 0 \\ 0 & -\mathcal{A}_3 & 0 - \mathcal{C}_3 \\ 0 & -\mathcal{C}_3 & -\mathcal{A}_3 \end{pmatrix}, \quad \mathcal{K}(-1, 1, 0) = \begin{pmatrix} -\mathcal{A}_3 & \mathcal{C}_3 & 0 \\ \mathcal{C}_3 & -\mathcal{A}_3 & 0 \\ 0 & 0 & \mathcal{B}_3 \end{pmatrix}$$

$$\mathcal{K}(-1, 0, 1) = \begin{pmatrix} -\mathcal{A}_3 & 0 & \mathcal{C}_3 \\ 0 & -\mathcal{B}_3 & 0 \\ \mathcal{C}_3 & 0 & -\mathcal{A}_3 \end{pmatrix}, \quad \mathcal{K}(0, -1, 1) \begin{pmatrix} \mathcal{B}_3 & 0 & 0 \\ 0 & -\mathcal{A}_3 & \mathcal{C}_3 \\ 0 & \mathcal{C}_3 & -\mathcal{B}_3 \end{pmatrix}. \tag{2.24}$$

It should be noted that by the inversion symmetry $\mathcal{K}_{\alpha\beta}(\mathbf{R}) = \mathcal{K}_{\alpha\beta}(-\mathbf{R})$. The force constant matrices of crystals with basis atoms can be derived by the same procedure with some extra attention to the indices.

Next, we explore another fundamental symmetry of the harmonic potential. Recall that the force of a harmonic potential is (2.7)

$$\Gamma_\alpha(\mathbf{R}) = -\frac{\partial \mathcal{V}}{\partial u_\alpha(\mathbf{R})} = -\sum_{\mathbf{R}', \beta} \mathcal{K}_{\alpha\beta}(\mathbf{R} - \mathbf{R}') u_\beta(\mathbf{R}') \tag{2.25}$$

By applying an arbitrary rigid translation $\mathbf{u} = \mathbf{c}$ to the body of the solid, the force becomes

$$\Gamma_\alpha(\mathbf{R}) = \sum_\beta c_\beta \sum_{\mathbf{R}'} \mathcal{K}_{\alpha\beta}(\mathbf{R} - \mathbf{R}') \tag{2.26}$$

However, a rigid translation of the body adds no additional force to the atoms. It follows that

$$\sum_{\mathbf{R}',\beta} \mathcal{K}_{\alpha\beta}(\mathbf{R} - \mathbf{R}') = 0 \tag{2.27}$$

Returning, to the problem of evaluating the dynamical matrix. From Eq.(2.27) and rearranging the order of the terms in the summation,

$$\mathcal{K}_{\alpha\beta}(\mathbf{0}) = -\sum_{\mathbf{R}\neq 0} \mathcal{K}_{\alpha\beta}(\mathbf{R}). \tag{2.28}$$

Substituting Eq.(2.28) in (2.17), we obtain

$$\gamma_{\alpha\beta}(\mathbf{q}) = \sum_{\mathbf{R}\neq 0} \mathcal{K}_{\alpha\beta}(\mathbf{R}) \left(e^{i\mathbf{q}\cdot\mathbf{R}} - 1\right) \tag{2.29}$$

Since $\gamma_{\alpha\beta}(\mathbf{q})$ is real,

$$\gamma_{\alpha\beta}(\mathbf{q}) = \sum_{\mathbf{R}\neq 0} \mathcal{K}_{\alpha\beta}(\mathbf{R}) \left(\cos(\mathbf{q}\cdot\mathbf{R}) - 1\right) \tag{2.30}$$

By expanding the summation of the element $\gamma_{11}(\mathbf{q})$ to the second nearest neighbor atoms and introducing the vector $\mathbf{p} = (p_1, p_2, p_3)$ by the definition, $\mathbf{q} = (q_x, q_y, q_z) \equiv \frac{2\pi}{a}(p_1, p_2, p_3)$, the component $\gamma_{11}(\mathbf{q})$ of the dynamical matrix can be written more compactly as

$$\begin{aligned}
\gamma_{11}(\mathbf{q}) =\, & 8\mathcal{A}_1 \left(1 - \cos \pi p_1 \cos \pi p_2 \cos \pi p_3\right) \\
& + 2\mathcal{A}_2(1 - \cos 2\pi p_1) \\
& + 2\mathcal{B}_2(2 - \cos 2\pi p_2 - \cos 2\pi p_3),
\end{aligned} \tag{2.31}$$

Similarly,

$$\gamma_{12}(\mathbf{q}) = 8\mathcal{C}_1 \sin \pi p_1 \sin \pi p_2 \cos \pi p_3. \tag{2.32}$$

The other elements of $\gamma_{\alpha\beta}(\mathbf{q})$ can be obtained from cyclic permutations:

$$\begin{aligned}
& \gamma_{22}(\mathbf{q}) = \gamma_{11}(p_2, p_3, p_1),\ \gamma_{33}(\mathbf{q}) = \gamma_{11}(p_3, p_1, p_2) \\
& \gamma_{23}(\mathbf{q}) = \gamma_{12}(p_2, p_3, p_1),\ \gamma_{31}(\mathbf{q}) = \gamma_{12}(p_3, p_1, p_2) \\
& \gamma_{13}(\mathbf{q}) = \gamma_{12}(p_1, p_3, p_2),\ \gamma_{32}(\mathbf{q}) = \gamma_{12}(p_3, p_2, p_1) \\
& \gamma_{21}(\mathbf{q}) = \gamma_{12}(p_2, p_1, p_3).
\end{aligned} \tag{2.33}$$

2.2.3   The Dispersion Relations and Elastic Anisotropy

With an exception of a few [22, 20], most literature does not emphasize the relationship between the phonon modes and the elastic anisotropy. In this subsection, this concept is established. The idea follows directly from De Fontaine [22] and Brüesch [20].

In the elastic continuum theory, the potential energy $\mathcal{V}$ due to a small displacement is given by

$$\mathcal{V} = \frac{1}{2} \int \mathrm{d}^3 \mathbf{r} \sum_{\alpha\beta\kappa\lambda} c_{\alpha\kappa\beta\lambda} \partial_\kappa u_\alpha \partial_\lambda u_\beta = \frac{\Omega}{2} \sum_{\mathbf{q}} \sum_{\alpha\beta\kappa\lambda} c_{\alpha\kappa\beta\lambda} q_\kappa q_\lambda \tilde{u}_\alpha^*(\mathbf{q}) \tilde{u}_\beta(\mathbf{q}), \qquad (2.34)$$

In the all- and long-wavelength versions of the harmonic models in Eq.(2.4) and (2.34) must match at small $\mathbf{q}$. From the long-wavelength limit the dynamical matrix is

$$\gamma_{\alpha\beta}(\mathbf{q}) \approx \frac{\Omega}{N} \sum_{\kappa,\lambda} c_{\alpha\kappa\beta\lambda} q_\kappa q_\lambda = v \sum_{\kappa,\lambda} c_{\alpha\kappa\beta\lambda} q_\kappa q_\lambda. \qquad (2.35)$$

For a cubic material, the component $\gamma_{11}(\mathbf{q})$ and $\gamma_{12}(qv)$ are

$$\gamma_{11}(\mathbf{q}) = \frac{a^3}{2} \left[C_{11} q_1^2 + C_{44}(q_2^2 + q_3^2) \right]$$
$$\gamma_{12}(\mathbf{q}) = \frac{a^3}{2} \left(C_{12} + C_{44} \right) q_1 q_2. \qquad (2.36)$$

where C_{11}, C_{12}, and C_{44} are the cubic elastic constants.

For the all-wavelength harmonic model, at small $q_i = (2\pi/a)p_i$ the component γ_{11} and γ_{12} of the dynamical matrix in Eq.(2.31) and (2.32) reduce to

$$\gamma_{11}(\mathbf{q}) \simeq a^2 \left(\mathcal{A}_1 + \mathcal{A}_2 \right) q_1^2 + a^2 \left(\mathcal{A}_1 + \mathcal{B}_2 \right) \left(q_2^2 + q_3^2 \right)$$
$$\gamma_{12}(\mathbf{q}) \simeq 2a^2 \mathcal{C}_1 q_1 q_2, \qquad (2.37)$$

By matching Eq.(2.36) to (2.37), the major relations which determine the dynamical matrix are

$$2\mathcal{A}_1 + 2\mathcal{A}_2 = aC_{11}$$
$$2\mathcal{A}_1 + 2\mathcal{B}_2 = aC_{44} \qquad (2.38)$$
$$4\mathcal{C}_1 = a(C_{12} + C_{44}),$$

which is a simple set of three linear equations with four unknowns. The dynamical matrix can be determined within this approximation by solving Eq.(2.38), provided that one can find a relation for the fourth parameter.

In summary, the seminal developments in [22] and [20] provide analytical relation between the elastic anisotropy (C_{11}, C_{12} and C_{44}) to the dynamical matrix of a solid. Within the second-order approximation, this relation can be solved nearly uniquely after the remaining degree of freedom has been determined by some other method. The natural method to fix this degree of freedom is the first principle calculations. The dispersion relations for various Ti-V approximants to Gum Metal are obtained in the next section

2.3 The Phonon Dispersion Relations in Gum Metal

2.3.1 Computational Details

The inputs to Eq.(2.38) are obtained from first principles. The elastic constants C_{11}, C_{12} and C_{44} of Gum Metal have already been presented Li *et al.* [6]. The remaining degree of freedom of Eq.(2.38) is fitted to the high-energy phonon frequency obtained by a frozen phonon calculation [24].

The sizes and shapes of the calculating cells are governed by the propagating direction $\mathbf{q}$, and the polarization directions are determined from the eigenvectors of the dynamical matrix. The preliminary dynamical matrix is obtained by matching the acoustic modes at the long wavelengths to the elastic properties of the solids. The elastic wave in an cubic medium is obtained by solving the wave equation in an anisotropic medium [23]:

$$\sum_{\alpha} \sum_{\gamma\lambda} \left(c_{\alpha\gamma\beta\lambda} q_\gamma q_\lambda - \delta_{\alpha\beta}\rho\omega^2 \right) u_\beta = 0. \tag{2.39}$$

where ρ is the crystal density. For the acoustic waves along the [110] direction of a BCC crystal , it follows that:

$$\omega_L^2 = \frac{(C_{11} + C_{12} + 2C_{44})}{2\rho}q^2, \quad \text{with the eigenvector } \mathbf{a}^{(1)} = (1,1,0)/\sqrt{2}$$

$$\omega_{T_1}^2 = \frac{(C_{11} - C_{12})}{2\rho}q^2, \quad \text{with the eigenvector } \mathbf{a}^{(2)} = (-1,1,0)/\sqrt{2} \tag{2.40}$$

$$\omega_{T_2}^2 = \frac{C_{44}}{\rho}q^2, \quad \text{with the eigenvector } \mathbf{a}^{(3)} = (0,0,1).$$

The wave speeds are the group velocity obtained from these branches at small $\mathbf{q}$. Relationships like Eq.(2.40) hold true in all directions, although different combinations of elastic constants are required. The initial parameter $\mathcal{A}_1$ in Eq.(2.31) is obtained by matching ω_L, ω_{T_1}, and ω_{T_2} obtained from Eq.(2.40) to those obtained by solving Eq.(2.31). Numerical results show that the eigenvectors of the short wavelength phonons do not change directions. The effect of changing the parameter $\mathcal{A}_1$ (in Eq.(2.31)) simply shifts the phonon frequencies while maintaining the polarization directions. Two phonon dispersion relations are plot in Fig. 2.1 for different values of $\mathcal{A}_1$.

The eigenvectors are obtained by solving the relations like those yielding Fig. 2.1. The low-energy and wavelength modes for the frozen phonon calculations are the $\mathbf{q}_\omega$, and the $N-$point phonon. The first Brillouin zone and an adjacent zone is displayed in Fig. 2.2. The amplitudes of vibrations are set arbitrarily to a few percent of the atomic plane spacing. The structures of the unit cells dictated by the propagating vectors $\mathbf{q}$'s are displayed in Fig. 2.3. The cells representing the $H-$point, $\mathbf{q}_\omega$, and $N-$point phonons contains two, three , and three atoms as displayed.
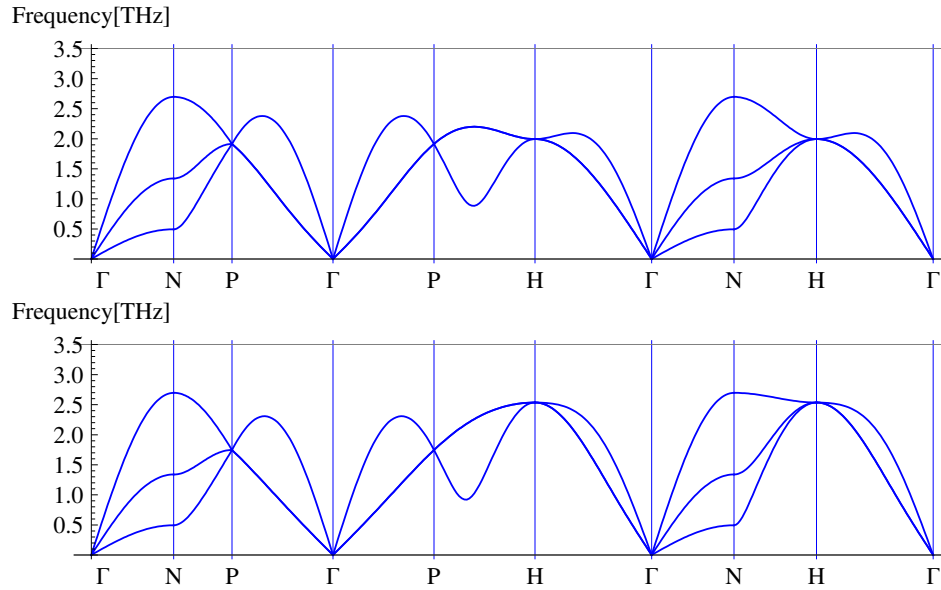
Figure 2.1: The dispersion relations obtained by solving Eq.(2.31) while setting (a) $\mathcal{A}_1 = 0.4$ eV/Å, and (b) $\mathcal{A}_1 = 0.8$ eV/Å. The elastic constants are $C_{11} = 0.91$, $C_{12} = 0.83$, and $C_{44} = 0.29$ eV/Å^3, corresponding to Ti-V alloy with the number of valence electron per atom ratio of 4.25.
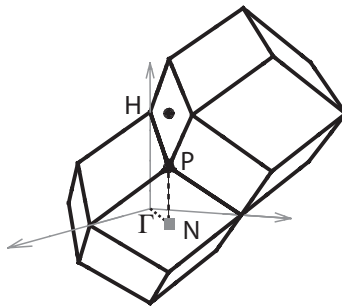
Figure 2.2: A particular stacking of two BZ of the BCC structure. The black dot displays the point $\mathbf{q} = \left(\frac{1}{2}\frac{1}{2}1\right)$, which is symmetrically equivalent to the $N-$point phonon.
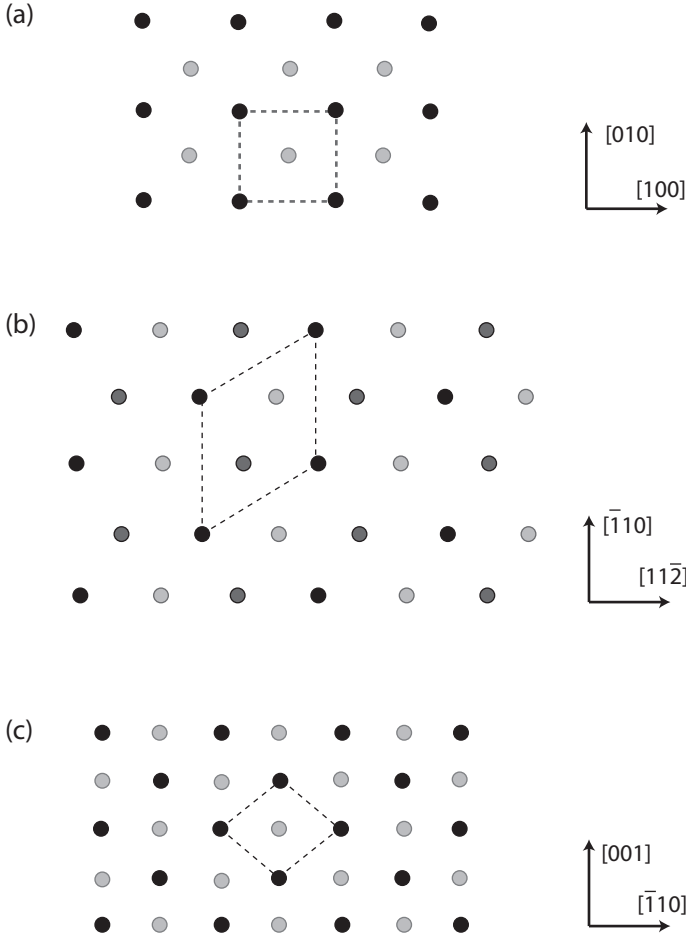
Figure 2.3: The unit cells for calculating the (a) H-point phonon, (b) the $\mathbf{q}_\omega$ phonon, and (c) the N-point phonon. The different gray scales distinguish atomic planes

The matching of the acoustic modes is removed by the empirical fitting at the high-energy H-point. The frozen phonon data is obtained using the Quantum Espresso package [25], and the virtual crystal approximation for Ti-V alloys [6]. The Troullier-Martin psedopotentials are employed. The energy cutoff of the frozen phonon calculations is 1560 eV. For calculations of the H-point phonon, the density of the $\mathbf{k}$ points is $16 \times 16 \times 16$. The $\mathbf{k}$-point grid is generated by the Mohkhorst-Pack scheme. The shape of the repeating unit cells of the $\mathbf{q}_\omega$ and $N-$point phonon are different from the $H-$point phonon. The number of the converging $\mathbf{k}$-grid in the $\mathbf{q}_\omega$ and $N-$point phonon calculations are $13 \times 13 \times 21$ and $18 \times 18 \times 11$ respectively. Both choices of energy cut-offs and numbers of $\mathbf{k}$ points lead to the energy convergence of less than 0.03 meV/atom. The atomic relaxations are conducted with Fermi-Dirac smearing of 0.27 eV. The dispersion relations along the high symmetry paths of this bcc structure are displayed in Fig. 2.4.

2.3.2   Computer Results and Discussion

Two anomalies are evident from the dispersion relations in Fig. 2.4: (1) The transverse mode close to (but not exactly) $\mathbf{q} = \left(\frac{1}{3}, \frac{1}{3}, \frac{2}{3}\right)$ has a dip in energy, and (2) the transverse branch from Γ to N with $[1\bar{1}0]$ polarization has an unusually low energy extending from the center to the zone edge.

Consider first the transverse mode with the propagation vector close to $\mathbf{q} = \left(\frac{1}{3}, \frac{1}{3}, \frac{2}{3}\right)$. The lowest energy eigenvalue corresponds to the $[11\bar{1}]$ polarization. This transverse mode is symmetrically equivalent to the longitudinal one with $\mathbf{q} = \left(\frac{2}{3}, \frac{2}{3}, \frac{\bar{2}}{3}\right)$. The atomic displacements along the $\langle ppp \rangle$ direction by this phonon mode result in two of the three neighboring (111) planes moving toward each other, whereas every third plane remains at rest. This structural transformation leads to ω phase, hence this type of phonon is named the $\mathbf{q}_\omega$ phonon. The same transformation mechanism has been reported in other BCC alloys [19].

The calculated total energy as a function of the displacement amplitude for $\mathbf{q} = \mathbf{q}_\omega$ frozen phonon for the composition $\text{Ti}_{25}\text{V}_{75}$, $\text{Ti}_{50}\text{V}_{50}$, and $\text{Ti}_{75}\text{V}_{25}$ is displayed in Fig. 2.5. The energy functions of $\text{Ti}_{25}\text{V}_{75}$ and $\text{Ti}_{50}\text{V}_{50}$ are close to parabolic near zero displacement, indicating nearly harmonic behavior. The calculated vibrational frequencies of these two compositions are closed to the harmonic model as shown in Fig. 2.4. The energy rises sharply in the direction of oscillation away from the ω structure, while on the other side it rises to a local maximum at the amplitude of ~ 0.45 Å, required for ω-phase formation. The energy-amplitude relations suggest that the ω phase is unstable in Gum Metal.

The N-point phonon mode is revealed in diffraction patterns. By stacking two adjacent Brillouin zone as in Fig. 2.2, it is clear that the transverse N-point phonon mode is also equivalent to the $\mathbf{q} = (\frac{1}{2}, \frac{1}{2}, 1)$ mode with the [110] polarization. The dispersion relation at the point of type $(\frac{1}{2}, \frac{1}{2}, 1)$ (i.e. the point $(m/2,\ m/2, m)$, where m is an odd integer) can be seen on the (110) section of the $q-$space. The diffraction patterns on the $(1\bar{1}0)$ plane of Gum Metal is shown Fig. 2.6(a). The minor peaks at $\mathbf{q} = (\frac{1}{2}, \frac{1}{2}, 1)$ correspond to the HCP phase,
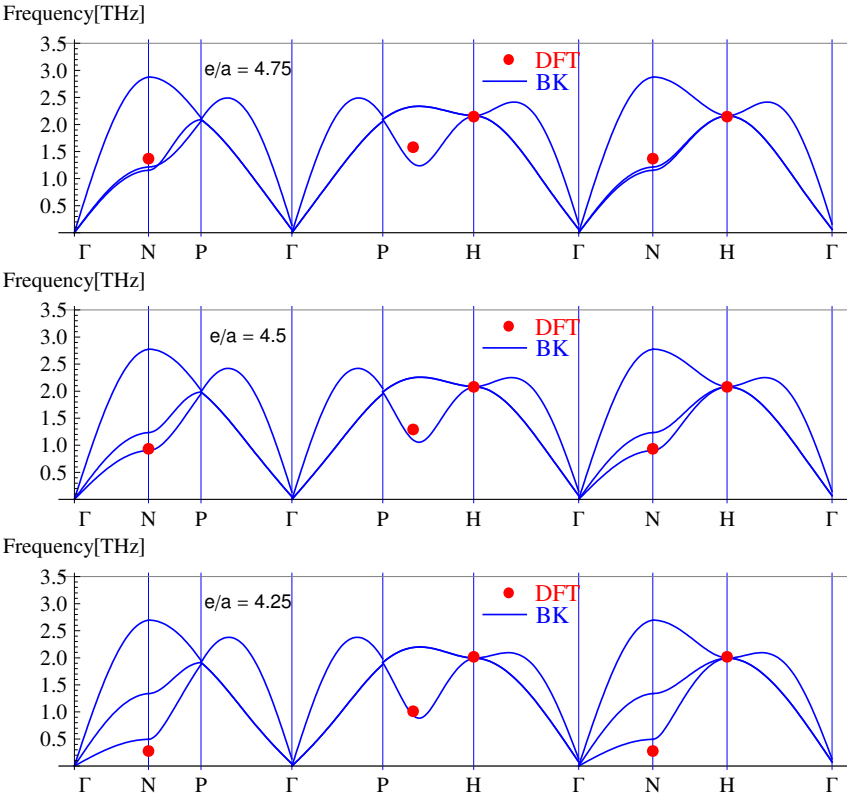
Figure 2.4: Dispersion relations over a range of the ratio (e/a) of the Ti-V alloys. The ratio $e/a = 4.75, 4.50,$ and 4.25 corresponds to the composition $Ti_{25}V_{75}$, $Ti_{50}V_{50}$, and $Ti_{75}V_{25}$ respectively. The blue lines are the Born-von Karman(BK) harmonic approximations, while the red dots are obtained from frozen phonon calculations.
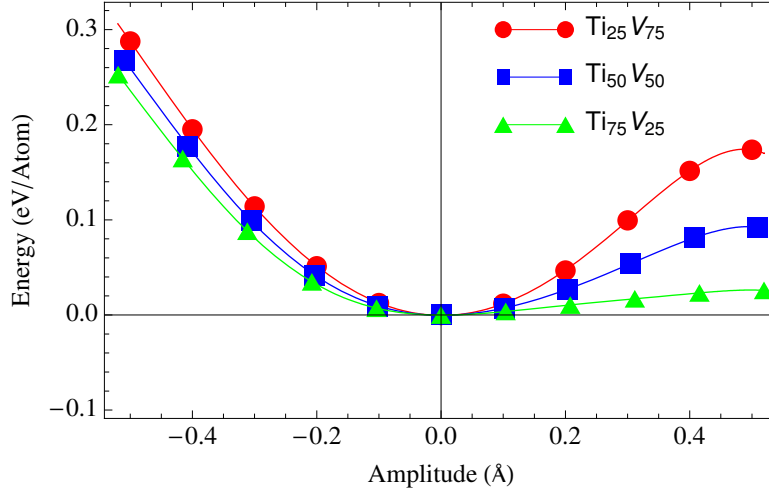
Figure 2.5: Total energy of $\left(\frac{2}{3}, \frac{2}{3}, \frac{2}{3}\right)$ phonon as a function of displacement amplitude.

while the weak intensities at $\mathbf{q} = \left(\frac{1}{3}, \frac{1}{3}, \frac{2}{3}\right)$ and $\left(\frac{2}{3}, \frac{2}{3}, \frac{4}{3}\right)$ corresponds to stable ω-phase.

It is believed that the lower intensity excitations at the points of type $\left(\frac{1}{2}, \frac{1}{2}, 1\right)$ are indicative of the N-point phonon as dark field imaging yields no evidence of the HCP phase. The theoretical intensity of diffraction patterns of phonon scattering are obtained to confirm this hypothesis. The intensity obtained from the thermal average of the displacement fluctuations is give by

$$I(\mathbf{q}) = I_o(\mathbf{q}) + I_1(\mathbf{q}) + I_2(\mathbf{q}) + \dots \tag{2.41}$$

where

$$
\begin{aligned}
I_o(\mathbf{q}) =& N e^{-2W(\mathbf{q})} \sum_R e^{i\mathbf{q}\cdot\mathbf{R}} \\
I_1(\mathbf{q}) =& \frac{N}{m} e^{-2W(\mathbf{q})} \sum_r \left|\mathbf{q}\cdot\mathbf{a}^{(r)}(\mathbf{q}-\mathbf{G})\right|^2 \frac{\langle E_r(\mathbf{q}-\mathbf{G})\rangle}{\omega^{2(r)}(\mathbf{q}-\mathbf{G})} \\
I_2(\mathbf{q}) =& \frac{1}{2m^2} e^{-2W(\mathbf{q})} \sum_{\mathbf{k},r} \sum_{r'} \left|\mathbf{q}\cdot\mathbf{a}^{(r)}(\mathbf{k})\right|^2 \left|\mathbf{q}\cdot\mathbf{a}^{(r)}(\mathbf{G}-\mathbf{k}-\mathbf{q})\right|^2 \\
& \frac{\langle E_r(\mathbf{k})\rangle}{\omega^{2(r)}(\mathbf{k})} \frac{\langle E_r(\mathbf{G}-\mathbf{k}-\mathbf{q})\rangle}{\omega^{2(r')}(\mathbf{G}-\mathbf{k}-\mathbf{q})}.
\end{aligned}
\tag{2.42}
$$

Here, the average energy of a single oscillator is $\langle E_r(\mathbf{q})\rangle = (\hbar\omega/2)\coth(\hbar\omega/2k_B T)$. The index $r = 1, 2, 3$ labels the polarization of the phonon mode, and $W(\mathbf{q})$ is the Debye-Waller factor [18]. For the sake of completeness, the derivation of these expressions can be found in Appendix B.

Theoretical diffraction patterns on the $(1\bar{1}0)$ section are displayed in Fig.2.6(a) and (b). An experimental diffraction of solution-treated Gum Metal is shown in Fig. 2.6(c). The
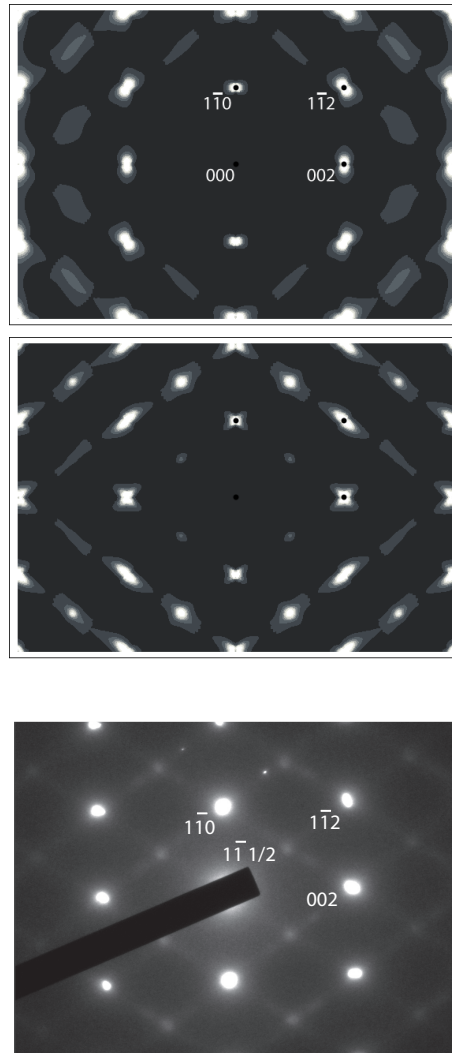
Figure 2.6: (a)Theoretical diffraction pattern of $Ti_{25}V_{75}$, and (b)$Ti_{85}V_{15}$. (c)The (110) transmission electron diffraction pattern of solution-treated Gum Metal.
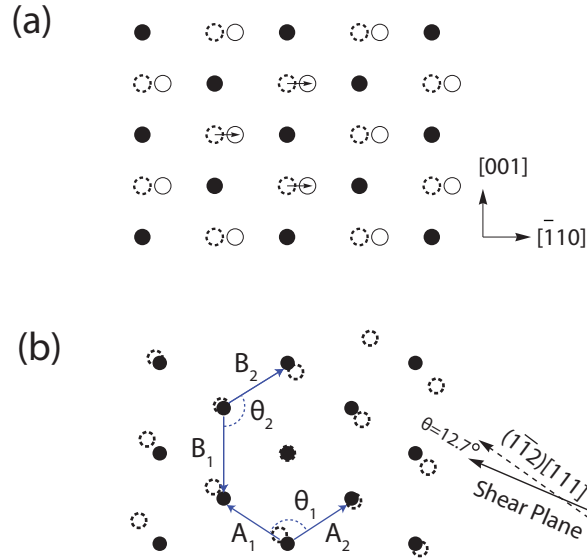
Figure 2.7: (a) The transverse $[\frac{1}{2}\frac{1}{2}0]$ mode with the $[1\bar{1}0]$ polarization. The arrows show the direction of the vibration of the alternating planes along [110]. (b)The atomic deformation on the (110) plane due to a long-wavelength shear close to the type $[1\bar{1}1](\bar{1}12)$.

pattern of $Ti_{75}V_{25}$ shows that there are minor intensities at points of type $\left(\frac{1}{2}, \frac{1}{2}, 1\right)$, while no $\mathbf{q}_\omega$ peaks are found. These results suggest that the experimental intensities at $\left(\frac{1}{2}, \frac{1}{2}, 1\right)$ are due to lattice fluctuations and not the formation of the α'' phase as suggested in [13]. On the other hand, the diffraction spots at the points of type $\mathbf{q}_\omega$ are due to stable ω-phase triggered by $\mathbf{q}_\omega$ phonon and some unknown mechanism. This result shows that it is possible for BCC alloy to maintain linear stability with respect to the formation of both the α'' and ω phase even in the limit where its ideal strength approaches zero.

2.3.3   Hints of The Influence of The Burgers Path

The short-wavelength fluctuations at the $N-$point result in displacements of two neighboring (110) plane in opposite $[1\bar{1}0]$ direction as shown in Fig.2.7(a). Viewing along the [110] direction, the $N-$point phonon leads to a structure close to hexagonal (α' phase). The angle between the atomic bonds in the basal plane are $109.47°$ and $125.27°$. The precise $120°$ angles required for forming a HCP structure can be achieved by applying a simple shear close to the type $[\bar{1}11](1\bar{1}2)$ as shown in Fig. 2.7(b). This transformation path is known as the Burgers path [26]. Surprisingly, the orientation of this simple shear, which is inclined from the $\langle 111 \rangle \{112\}$ by the angle about $13°$, resembles the observed microstructures of the giant faults and nano shear bands [8, 12].

From Fig. 2.7, the optimal shear angles and magnitude are obtained by solving two constraining functions which uniformly transform the angle between the vector $\mathbf{A}_1$ and $\mathbf{A}_2$,

and $\mathbf{B}_1$ and $\mathbf{B}_2$ (defined in Fig. 2.7), which are $\theta_1 = 109.47\,^\circ$ and $\theta_2 = 125.27\,^\circ$ respectively, to $120\,^\circ$.

A simple shear in the frame $\hat{\mathbf{e}}_1 = [\bar{1}\bar{1}\bar{1}]/\sqrt{3}$ and $\hat{\mathbf{e}}_2 = [1\bar{1}2]/\sqrt{6}$ is represented by the deformation gradient:

$$\mathbf{F}_\gamma = \begin{pmatrix} 1 & \gamma & 0 \\ 0 & 1 & 0 \\ 0 & 0 & 1 \end{pmatrix}. \tag{2.43}$$

An active transformation by an angle θ_γ rotates the the deformation gradient to

$$\mathcal{F}(\gamma, \theta_\gamma) = \mathbf{Q}^T \mathbf{F} \mathbf{Q}, \tag{2.44}$$

where

$$\mathbf{Q} = \begin{pmatrix} \cos\theta_\gamma & -\sin\theta_\gamma & 0 \\ \sin\theta_\gamma & \cos\theta_\gamma & 0 \\ 0 & 0 & 1 \end{pmatrix}. \tag{2.45}$$

The deformation gradient $\mathcal{F}$ transform a vector $\mathbf{r}$ to $\mathbf{r}'$ by

$$\mathbf{r}' = \mathcal{F}(\gamma, \theta_\gamma)\mathbf{r}. \tag{2.46}$$

In the Burgers transformation the vector pairs $\mathbf{A}_1$ and $\mathbf{A}_2$, and $\mathbf{B}_1$ and $\mathbf{B}_2$ are sheared by $\mathcal{F}$ to

$$\begin{aligned} \mathbf{A}'_1 &= \mathcal{F}(\gamma, \theta_\gamma)\mathbf{A}_1, \quad \text{and} \quad \mathbf{A}'_2 = \mathcal{F}(\gamma, \theta_\gamma)\mathbf{A}_2 \\ \mathbf{B}'_1 &= \mathcal{F}(\gamma, \theta_\gamma)\mathbf{B}_1, \quad \text{and} \quad \mathbf{B}'_2 = \mathcal{F}(\gamma, \theta_\gamma)\mathbf{B}_2, \end{aligned} \tag{2.47}$$

respectively. The resultant inner angles of the basal plane of the HCP structure are $2\pi/3$.

Defining two constraining functions

$$\begin{aligned} f_1(\mathbf{A}'_1, \mathbf{A}'_2) &= \cos^{-1}(\mathbf{A}'_1 \cdot \mathbf{A}'_2) - 2\pi/3 \equiv F_1(\gamma, \theta_\gamma) \\ f_2(\mathbf{B}'_2, \mathbf{B}'_2) &= \cos^{-1}(\mathbf{B}'_1 \cdot \mathbf{B}'_2) - 2\pi/3 \equiv F_2(\gamma, \theta_\gamma) \end{aligned} \tag{2.48}$$

The necessary geometric condition for BCC-to-HCP transformation requires that both $F_1(\gamma, \theta_\gamma)$ and $F_2(\gamma, \theta_\gamma)$ are simultaneously zeros when the transformation is complete. The zeros of these functions can be solved numerically for the optimal γ^* and θ_γ^*. The plots of $F_1(\gamma^*, \theta_\gamma)$ and $F_2(\gamma^*, \theta_\gamma)$ are displayed in Fig. (2.8). The solution of the shear system of $\theta_\gamma^* = -12.7\,^\circ$ and $\gamma^* = 0.20$ relative to the $[\bar{1}11](1\bar{1}2)$ slip system coincides with the orientation of the observed giant faults and nano shearbands. Since our solution method concerns no energy principle, both faults should be the results of the compatibility within the material.

Also, both length scales of the giant faults and nano shear bands are consistent with the long-wavelength shear mode. The resemblance to the giant faults and shear bands indicates that both faults result from the $N-$point phonon and the long-wavelength shear close to
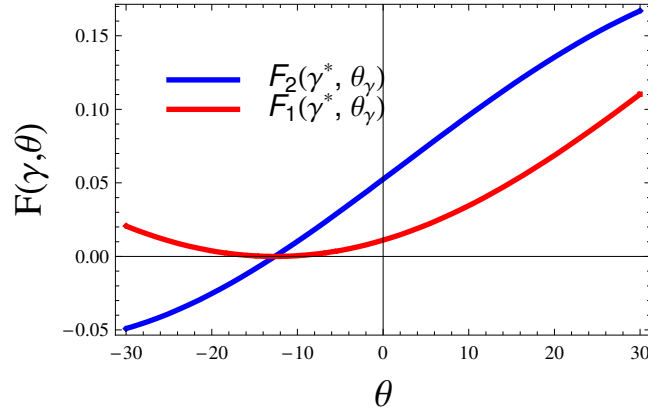
Figure 2.8: Two constraining functions $F_1(\gamma^*, \theta_\gamma)$ and $F_2(\gamma^*, \theta_\gamma)$. The zeros of the functions corresponds to the optimal shear angle $\theta_\gamma^* = -12.7\,^\circ$ which transform the internal angles $\theta_1 = 109.47\,^\circ$ and $\theta_2 = 125.27\,^\circ$ of the BCC basal plane into $120\,^\circ$.

$\langle 111 \rangle \{112\}$, as the structure is relaxing to a HCP phase. Considering the deformation led by the $N-$point phonon, supercell calculations of a dislocation dipole in Ti-V alloys reveals similar $\langle 111 \rangle \{112\}$ shear bands [12]. Similar influence of the soft $N-$point phonon is also found in potassium [27].

In summary, phonon dispersion relations, obtained from a harmonic model in conjunction with first principles calculations provide insights into potential structural transformation in Gum Metal. The soft $\mathbf{q}_\omega$ phonon leads to the ω phase. The transformation to the α'' is associated with a transverse $N-$point phonon. However, the alloys can be designed so that they are linearly stable with respect to the formation of both phases. Furthermore, even though the BCC structure us linearly stable, the soft phonons can lead to diffuse scattering in diffraction experiments. Theoretical predictions for this diffuse scattering give patterns similar to that observed during electron diffraction experiments of solution treated Gum Metal. By analyzing the geometry of the N-point mode with the $[1\bar{1}0]$ polarization and examining the microstructures of the post-deformation Gum Metal, the role of the $N-$point phonon becomes apparent. The giant faults and the nano shearbands are formed by the compatibility condition while the structure relaxes along the Burgers path (BCC $\to$ HCP or $\beta \to \alpha'$ phase).

The next two chapters quantify the energies, and other properties of this path. In chapter 3, the computational tool is explained. Chapter 4 explores the Burgers path in Ti-V approximants to Gum Metal. The computational results are verified by by comparative study of the Bain path in Ti-V alloys [6] and the Burgers path in sodium [28].

Chapter 3

Searching for A Minimum Energy Path

As shown in the previous chapter that the BCC-to-HCP transformation plays an important role in the formation of the giant faults and nano shearbands. One of the goals of this dissertation is to elucidate this mechanism. The studying tool is a minimum energy path (MEP) searching method called the nudged-elastic-band (NEB) [10]. The energies, stiffness, and structural properties of a solid can be obtained by this method. It has been shown that the NEB method successfully explains a variety of materials science problems, for example: a diffusion of Cu atoms [10], the transformation of iron under hydrostatic stresses [29], and the study of dislocation mobility in face-centered cubic materials [30].

This chapter is aimed at developing the underlying theory to our own extension of the NEB method. Section 3.1 gives a short account of the NEB formalism. In sections 3.2.1 and 3.2.2, we add that, by carefully choosing parameters describing the atomic motions, the generalized forces for solid-solid transformations can be obtained directly from the first-principles calculations. This conclusion is achieved by considering the quantum mechanical theory of stresses and forces.

The application of the NEB method is validated and used to describe the BCC-to-HCP transformation in a Ti-V approximant to Gum Metal in chapter 4.

3.1 The Nudged Elastic Band Method

An important problem in studying phase transition is to determine the minimum energy path (MEP) connecting one phase to the others. The Hamiltonian of an N-particles system is

$$\mathcal{H}(\mathbf{q}^{3N}, \mathbf{p}^{3N}) = \sum_{i}^{3N} \frac{p_i^2}{2m_i} + \mathcal{V}(\mathbf{q}^{3N}), \tag{3.1}$$
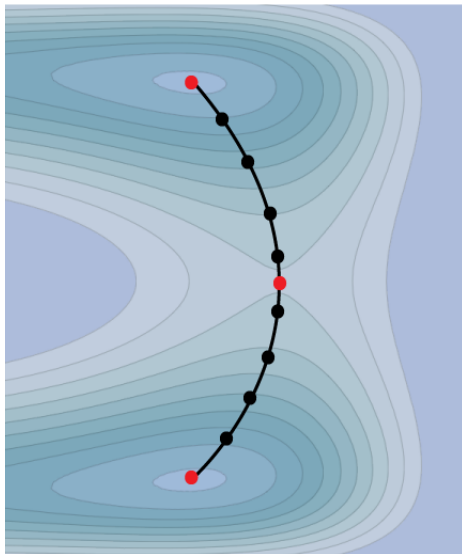
Figure 3.1: The optimal chain of states passing through the transition state or the saddle point of an energy surface.

where $\mathbf{q}^{3N}$ is a vector of length $3N$ containing all three components of the generalized positions of the N particles, and similarly for the momentum $\mathbf{q}^{3N}$. The summation is performed over all the elements in these two vectors. The first term is the kinetic energy term, while $\mathcal{V}(\mathbf{q}^{3N})$ is the potential. The Hamiltonian determines the structure and dynamics of the system.

A common procedure to determine the MEP between two energy minima starts with building a chain of states connecting them. An objective function is then defined to optimize the energy of the chain, while updating the interaction between the states within the chain. Here, each atomic configuration in the chain is called an image. In the NEB method, the images are joined by a series of fictitious springs of zero natural length. The MEP is then determined by minimizing a fictitious objective function that accounts for both the real interactions due to the gradient of the potential field and the fictitious spring interactions. The objective function defined this way is

$$S(\mathbf{R}_1, \mathbf{R}_2, \ldots, \mathbf{R}_P) = \sum_{i=0}^{P} \mathcal{V}(\mathbf{R}_P) + \sum_{i=1}^{P} \frac{k_i}{2}(\mathbf{R}_i - \mathbf{R}_{i-1})^2, \tag{3.2}$$

where $\mathbf{R}_i = \mathbf{q}^{(i)}$, the vector specifying the configuration of the ith image, and k_i is the fictitious spring constants.

A schematic energy contour of two reaction coordinates, i.e. $\mathbf{R}_i = (q_1^{(i)}, q_2^{(i)})$ is displayed in Figure 3.1. The contour contains two minima and a saddle point. The optimal chain connecting the two minima passes through the saddle point as shown. By optimizing the objective function, the MEP can be determined.
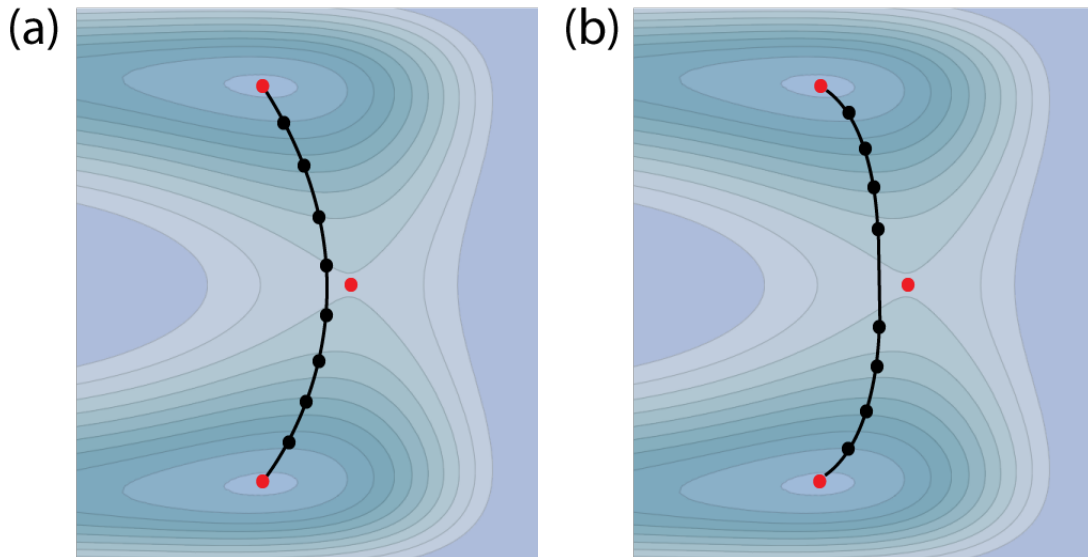
Figure 3.2: (a) The images cut the corner at the transition state due to the component of the spring forces perpendicular to the path, and (b) the images are sagging due to the component of the true forces $\nabla\mathcal{V}(\mathbf{R}_i)$ parallel to the path

However, by the softness of the potential and the strength of the springs, a direct optimization scheme may lead to an incorrect transition state energy. If the stiffness of the potential is too soft the resultant transition-energy may be underestimated. On the other hand, if the arbitrary spring constants are too strong, the transition-energy may be overestimated. These effects are illustrated in Fig.3.2. The underestimation is due to the sagging of the images into the potential wells, while the overestimation is from the corner cutting of the springs.

A cure to the overestimation and underestimation is first suggested by Jonsson *et al.* [10]. They propose a straightforward elimination of the corner cutting and image sagging by projecting out the forces causing the two effects. Generally, the force on the ith image is

$$\vec{\chi}_o^{(i)} = \vec{\chi}_t^{(i)} + \vec{\chi}_s^{(i)}, \tag{3.3}$$

where $\vec{\chi}_t^{(i)} = -\nabla\mathcal{V}(\mathbf{R}_i)$ is the true force representing the stiffness of the interatomic potential and $\vec{\chi}_s^{(i)}$ is the spring force. Like a general spring theory, the spring forces are given by

$$\vec{\chi}_s^{(i)} = k_{i+1}(\mathbf{R}_{i+1} - \mathbf{R}_i) - k_i(\mathbf{R}_i - \mathbf{R}_{i-1}). \tag{3.4}$$

Corner cutting and imaging sagging of the chain of states can be avoided by projecting out the parallel component of the true forces, and the perpendicular component of the spring forces while optimizing the objective function. This scheme is given the name *nudged elastic*

band method. The forces driving the chain of states to MEP become

$$\vec{\chi}^{(i)} = \vec{\chi}_{\perp}^{(i)} + \vec{\chi}_{\parallel}^{(i)}, \tag{3.5}$$

where

$$\begin{aligned}
\vec{\chi}_{\perp}^{(i)} &= \vec{\chi}_t^{(i)} - \left(\vec{\chi}_t^{(i)} \cdot \hat{l}_{\parallel} \right) \hat{l}_{\parallel}^{(i)}, \qquad \text{and} \\
\vec{\chi}_{\parallel}^{(i)} &= \left(\vec{\chi}_s^{(i)} \cdot \hat{l}_{\parallel}^{(i)} \right) \hat{l}_{\parallel}^{(i)}.
\end{aligned} \tag{3.6}$$

The tangent $\hat{l}^{(i)}$ to the ith image in the present work is approximated by parameterizing the reaction coordinates by a cubic spline function of a new parameter ψ as $\mathbf{R}_i = \mathbf{R}_i(\psi)$, so that $\hat{l}^{(i)} = \mathrm{d}\mathbf{R}(\psi)/\mathrm{d}\psi$.

Once the parallel true forces and the perpendicular spring forces are projected out, the optimized chain is believed to provide a better approximation to the saddle point energy. The objective function can be minimized by several numerical methods. One possible choice is the velocity Verlet integration scheme. The path dynamics is determined by the equations of motion:

$$\begin{aligned}
\mathbf{R}_i(t + \Delta t) &= \mathbf{R}_i(t) + \dot{\mathbf{R}}_i(t)\Delta t + \frac{1}{2}\frac{\vec{\chi}^{(i)}(t)}{m}\Delta t^2 \\
\dot{\mathbf{R}}_i(t + \Delta t) &= \dot{\mathbf{R}}_i(t) + \frac{\vec{\chi}^{(i)}(t + \Delta t) + \vec{\chi}^{(i)}(t)}{2m}\Delta t.
\end{aligned} \tag{3.7}$$

The optimal chain is the stationary solution to the above equations. Another possible optimization scheme is the steepest descent method. This method is equivalent to the velocity Verlet scheme when setting $\dot{\mathbf{R}}_i = 0$ in every time step. The key updating equations for the steepest descent method becomes

$$\mathbf{R}_i(\tau + \Delta\tau) = \mathbf{R}_i(\tau) + \vec{\chi}^{(i)}(t)\Delta\tau. \tag{3.8}$$

where $\Delta\tau$ is an arbitrary incremental step. The MEP is achieved when the stationary state is reached. The optimal chain has no true forces $\vec{\chi}_{\perp}$ at the saddle point. This condition is required for the saddle point to separate two nearby energy minima.

The remaining challenge to find the stationary solution of the chain is to determine the generalized forces $\vec{\chi}$. Since this work ultimately looks for the MEP of solid-solid transformations on some potential surfaces, the generalized forces must be defined consistent with the first-principles calculations. The next section demonstrates that, by a suitable choice of $\mathbf{R}_i$, the generalized forces can be obtained straightforwardly from the Kohn-Sham electronic ground state.

3.2 Quantum Mechanics of Forces and Stresses

The generalized forces required for the NEB method can be computed directed from first principles by the elementary Euler method. However, depending on the size of the unit cell this simple scheme may not be effective. The remaining of this chapter demonstrates that by choosing a particular set of the reaction coordinates, the forces can be computed effectively within a reasonable period of time. The key concept is to define generalized forces in connection with the quantum mechanical stresses [31] and the Hellman-Feynman forces [32], subjects which are discussed in the following sections.

3.2.1 Some Backgrounds on The Quantum Mechanical Stresses

The quantum-mechanical stress can be obtained by a scaling argument. The original work on this subject is given by Fock [31]. More modern reviews, extending the same argument to the quantum-mechanical stresses, are discussed extensively in [33, 34, 35, 36]. Here, we rederive the principles in order to develop the relationship of the stresses to the generalized forces in the NEB calculations.

The Hamiltonian of a many-body system of electrons and nuclei is given by

$$\hat{\mathcal{H}} = \hat{T} + \hat{V} = \sum_i \frac{\hat{p}_i^2}{2m_i} + \hat{V}_{\text{int}} + \hat{V}_{\text{ext}}. \tag{3.9}$$

where $\hat{p}_i$ is the momentum of the particle i, $\hat{V})_{int}$ is the intrinsic potential energy which is a function of the positions $\mathbf{r}^{(i)}$ of all the particles (including electrons and nuclei), and $\hat{V}_{\text{ext}}$ is the potential arisen from the externally applied forces.

As usual, the ground state can be estimated by the variational method. The ground state wavefunction $\Psi(\mathbf{r})$ is determined by minimizing $\langle \Psi | \hat{\mathcal{H}} | \Psi \rangle$ with respect to normalizing condition $\langle \Psi | \Psi \rangle = 1$. The vector $\mathbf{r}$ contains a list of all particle coordinates including both the electrons and nuclei, i.e.

$$\begin{aligned}
\mathbf{r} &= \{\mathbf{r}^{(1)}, \mathbf{r}^{(2)}, \dots \mathbf{r}^{(N)}\} \\
&= \{x^{(1)}, y^{(1)}, z^{(1)}, x^{(2)}, y^{(2)}, z^{(2)}, \dots, x^{(N)}, y^{(N)}, z^{(N)}\}.
\end{aligned} \tag{3.10}$$

That is N is the total number of all the electrons and nuclei.

In deriving the quantum mechanical stress, the function $\Psi(\mathbf{r})$ is stretched by a small and *symmetric* strain tensor $\boldsymbol{\varepsilon}$ as

$$r'^{(i)}_\alpha = r^{(i)}_\alpha + \sum_\beta \varepsilon_{\alpha\beta} r^{(i)}_\beta, \quad \text{or} \quad \mathbf{r}' = (\mathbf{I} + \boldsymbol{\varepsilon})\mathbf{r} \tag{3.11}$$

where the index i and α label the particles and the component on the Cartesian axes respectively. The wavefunction is scaled as

$$\Psi_\varepsilon(\mathbf{r}') = \frac{1}{\det(\mathbf{I} + \boldsymbol{\varepsilon})^{N/2}} \Psi\left((\mathbf{I} + \boldsymbol{\varepsilon})^{-1}\mathbf{r}'\right). \tag{3.12}$$
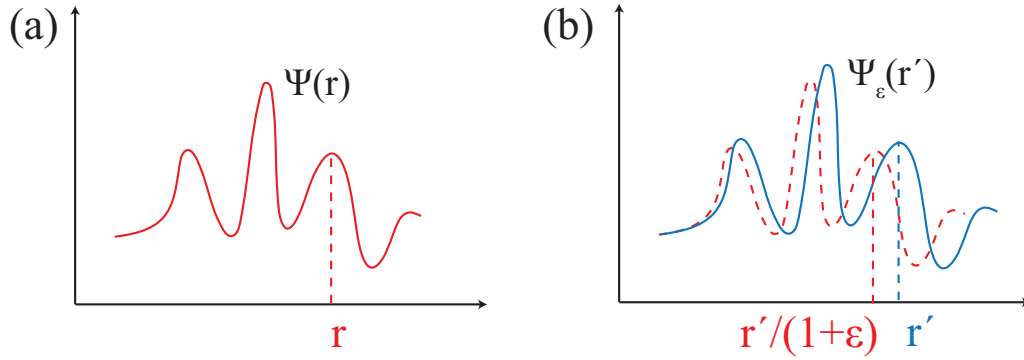
Figure 3.3: Rescaling of the wavefunction under a homogeneous stretching of $\Psi(\mathbf{r})$.

The above scaling of the wavefunction is illustrated diagrammatically as shown in Fig. 3.3 The additional factor of $\det(1 + \boldsymbol{\varepsilon})^{-N/2}$ is for preserving normalization of the functional:

$$\langle \Psi_\varepsilon | \Psi_\varepsilon \rangle = \int dx'^{(1)} dy'^{(1)} dz'^{(1)} \dots dx'^{(N)} dy'^{(N)} dz'^{(N)} \Psi_\varepsilon^*(\mathbf{r}') \Psi_\varepsilon(\mathbf{r}'). \tag{3.13}$$

By changing the variables $\mathbf{r}' \mapsto (\mathbf{I} + \varepsilon)\mathbf{r}$,

$$\langle \Psi_\varepsilon | \Psi_\varepsilon \rangle = \frac{1}{\det(I + \boldsymbol{\varepsilon})^N} \int dx^{(1)} dy^{(1)} dz^{(1)} \dots dx^{(N)} dy^{(N)} dz^{(N)} J \Psi^*(\mathbf{r}) \Psi(\mathbf{r}) \tag{3.14}$$

where J is the Jacobian,

$$J = \frac{\partial \left(x'^{(1)}, y'^{(1)}, z'^{(1)}, \dots, x'^{(N)}, y'^{(N)}, z'^{(N)} \right)}{\partial \left(x^{(1)}, y^{(1)}, z^{(1)}, \dots, x^{(N)}, y^{(N)}, z^{(N)} \right)} = \det(\mathbf{I} + \boldsymbol{\varepsilon})^N. \tag{3.15}$$

Since $\langle \Psi | \Psi \rangle = 1$ in the neutral state, it follows that $\langle \Psi_\varepsilon | \Psi_\varepsilon \rangle = 1$ in the stretched state.

Considering the stretched state Ψ_ε, the Hamiltonian becomes $\hat{\mathcal{H}}' = \hat{T}' + \hat{V}'$ where the vector $\mathbf{r}^{(i)}$ in Eq.(3.9) are replaced by $\mathbf{r}'^{(i)}$. The stationary Ψ_ε is determined by the variational principle that minimizes

$$E[\Psi_\varepsilon] = \frac{I[\Psi_\varepsilon]}{J[\Psi_\varepsilon]}, \tag{3.16}$$

where

$$I[\Psi_\varepsilon] = \langle \Psi_\varepsilon | \hat{\mathcal{H}}' | \Psi_\varepsilon \rangle, \quad \text{and} \quad J[\Psi_\varepsilon] = \langle \Psi_\varepsilon | \Psi_\varepsilon \rangle. \tag{3.17}$$

The average energy over the state Ψ_ε is

$$\langle \Psi_\varepsilon(\mathbf{r}') | \hat{\mathcal{H}}' | \Psi_\varepsilon(\mathbf{r}') \rangle = \langle \Psi_\varepsilon | (\hat{T}' + \hat{V}') | \Psi_\varepsilon \rangle. \tag{3.18}$$

Consider first the kinetic energy term:

$$
\begin{aligned}
\langle \Psi_\varepsilon | \hat{T}' | \Psi_\varepsilon \rangle &= \int \mathrm{d}^3 \mathbf{r}'^{(1)} \ldots \mathrm{d}^3 \mathbf{r}'^{(N)} \Psi_\varepsilon^*(\mathbf{r}') \hat{T}' \Psi_\varepsilon(\mathbf{r}') \\
&= \frac{1}{\det(\mathbf{I}+\boldsymbol{\varepsilon})^N} \int \mathrm{d}^3 \mathbf{r}'^{(1)} \ldots \mathrm{d}^3 \mathbf{r}'^{(N)} \Psi^*((\mathbf{I}+\boldsymbol{\varepsilon})^{-1}\mathbf{r}') \hat{T}' \Psi((\mathbf{I}+\boldsymbol{\varepsilon})^{-1}\mathbf{r}').
\end{aligned}
\tag{3.19}
$$

By making the change of variable $\mathbf{r}' \mapsto (\mathbf{I}+\boldsymbol{\varepsilon})\mathbf{r}$, the kinetic energy becomes

$$
\langle \Psi_\varepsilon | \hat{T}' | \Psi_\varepsilon \rangle = \sum_i \int \mathrm{d}^3 \mathbf{r}^{(1)} \ldots \mathrm{d}^3 \mathbf{r}^{(N)} \Psi^*(\mathbf{r}) \frac{\hat{\mathbf{p}}'^{(i)} \cdot \hat{\mathbf{p}}'^{(i)}}{2m} \Psi(\mathbf{r})
\tag{3.20}
$$

The momentum in the stretched coordinates is

$$
\hat{\mathbf{p}}'^{(i)} = -i\hbar \frac{\partial}{\partial \mathbf{r}'^{(i)}} = -i\hbar(\mathbf{I}+\boldsymbol{\varepsilon})^{-1} \frac{\partial}{\partial \mathbf{r}^{(i)}} = (\mathbf{I}+\boldsymbol{\varepsilon})^{-1} \hat{\mathbf{p}}^{(i)}
\tag{3.21}
$$

and

$$
(\mathbf{I}+\boldsymbol{\varepsilon})^{-1}(\mathbf{I}+\boldsymbol{\varepsilon})^{-1} \approx (\mathbf{I} - 2\boldsymbol{\varepsilon} + 3\boldsymbol{\varepsilon}^2 + \ldots),
\tag{3.22}
$$

for small $\boldsymbol{\varepsilon}$. By keeping the terms of order $\mathcal{O}(\varepsilon^2)$, the kinetic term becomes

$$
\langle \Psi_\varepsilon | \hat{T}' | \Psi_\varepsilon \rangle = (\mathbf{I} - 2\boldsymbol{\varepsilon} + 3\boldsymbol{\varepsilon}^2) : \sum_i^N \int \mathrm{d}^3 \mathbf{r}^{(1)} \ldots \mathrm{d}^3 \mathbf{r}^{(N)} \Psi^* \frac{\hat{\mathbf{p}}^{(i)} \otimes \hat{\mathbf{p}}^{(i)}}{2m} \Psi,
\tag{3.23}
$$

where the sign ' : ' implies double-indices contraction.

Next, consider the potential energy

$$
\begin{aligned}
\langle \Psi_\varepsilon | \hat{V}' | \Psi_\varepsilon \rangle &= \int \mathrm{d}^3 \mathbf{r}^{(1)} \ldots \mathrm{d}^3 \mathbf{r}^{(N)} \Psi^*(\mathbf{r}) \left[\hat{V}_{\text{int}}((\mathbf{I}+\boldsymbol{\varepsilon})\mathbf{r}) + \hat{V}_{\text{ext}}((\mathbf{I}+\boldsymbol{\varepsilon})\mathbf{r}) \right] \Psi(\mathbf{r}) \\
&= \int \mathrm{d}^3 \mathbf{r}^{(1)} \ldots \mathrm{d}^3 \mathbf{r}^{(N)} \Psi^*(\mathbf{r}) \left[\hat{V}_{\text{int}}(\mathbf{r}) + \sum_i \boldsymbol{\varepsilon} : \mathbf{r}^{(i)} \otimes \nabla \hat{V}_{\text{int}} + \hat{V}_{\text{ext}}(\mathbf{r}) + \sum_i \boldsymbol{\varepsilon} : \mathbf{r}^{(i)} \otimes \hat{V}_{\text{ext}} \right] \Psi(\mathbf{r}).
\end{aligned}
\tag{3.24}
$$

The functional $E[\Psi_\varepsilon]$ can be written as

$$
\begin{aligned}
E[\Psi_\varepsilon] =& \langle \Psi_\varepsilon | \hat{T}' + \hat{V}' | \Psi_\varepsilon \rangle \\
=& \langle \Psi | \hat{T} | \Psi \rangle + \langle \Psi | \hat{V} | \Psi \rangle - (2\varepsilon - 3\varepsilon^2) \sum_i \int \mathrm{d}^3 \mathbf{r}^{(1)} \dots \mathrm{d}^3 \mathbf{r}^{(N)} \Psi^* \frac{\hat{\mathbf{p}}^{(i)} \otimes \hat{\mathbf{p}}^{(i)}}{2m} \Psi \\
& + \sum_i \int \mathrm{d}^3 \mathbf{r}^{(1)} \dots \mathrm{d}^3 \mathbf{r}^{(N)} \Psi^* \left[\boldsymbol{\varepsilon} : (\mathbf{r}^{(i)} \otimes \nabla^{(i)} \hat{V}_{\mathrm{int}}) \right] \Psi \\
& + \sum_i \int \mathrm{d}^3 \mathbf{r}^{(1)} \dots \mathrm{d}^3 \mathbf{r}^{(N)} \Psi^* \left[\boldsymbol{\varepsilon} : (\mathbf{r}^{(i)} \otimes \nabla^{(i)} \hat{V}_{\mathrm{ext}}) \right] \Psi \\
=& E[\Psi] + \boldsymbol{\varepsilon} : \sum_i \int \mathrm{d}^3 \mathbf{r}^{(1)} \dots \mathrm{d}^3 \mathbf{r}^{(N)} \Psi^* \left[-\frac{\hat{\mathbf{p}}^{(i)} \otimes \hat{\mathbf{p}}^{(i)}}{m} + \mathbf{r}^{(i)} \otimes \nabla^{(i)} \hat{V}_{\mathrm{int}} + \mathbf{r}^{(i)} \otimes \nabla^{(i)} \hat{V}_{\mathrm{ext}} \right] \Psi \\
& + \mathcal{O}(\varepsilon^2).
\end{aligned}
\tag{3.25}
$$

The difference δE is in the second order $\mathcal{O}(\varepsilon^2)$. The stationary state is achieved when

$$
\frac{\partial E}{\partial \varepsilon_{\alpha\beta}} \bigg|_{\varepsilon=0} = \sum_i \left\langle \Psi \left| \frac{\hat{p}_\alpha^{(i)} \hat{p}_\beta^{(i)}}{m} - r_\beta^{(i)} \nabla_\alpha^{(i)} (\hat{V}_{\mathrm{int}} + \hat{V}_{\mathrm{ext}}) \right| \Psi \right\rangle = 0.
\tag{3.26}
$$

Eq.(3.26) constitutes an analogy to the continuum stress. The mechanical stress exerted by the external environment is defined as

$$
\sigma_{\alpha\beta}^{\mathrm{ext}} = -\frac{1}{\Omega} \sum_i \left\langle \Psi \left| r_\beta^{(i)} \nabla_\alpha^{(i)} \hat{V}_{\mathrm{ext}} \right| \Psi \right\rangle,
\tag{3.27}
$$

for a structure with volume Ω. For the internal stress from the interacting electrons and nuclei, it is

$$
\sigma_{\alpha\beta}^{\mathrm{int}} = \frac{1}{\Omega} \sum_i \left\langle \Psi \left| \frac{\hat{p}_\alpha^{(i)} \hat{p}_\beta^{(i)}}{m} - r_\beta^{(i)} \nabla_\alpha^{(i)} \hat{V}_{\mathrm{int}} \right| \Psi \right\rangle.
\tag{3.28}
$$

It can be seen that Eq.(3.26) is nothing but the quantum mechanical equilibrium condition.

$$
\sigma_{\alpha\beta}^{\mathrm{ext}} + \sigma_{\alpha\beta}^{\mathrm{int}} = 0.
\tag{3.29}
$$

in agreement with the analogous picture in continuum theory. It should be note that the quantum mechanical stress derived this way is automatically symmetric.

In the case of zero external field ($\hat{V}_{\mathrm{ext}} = 0$), a total-energy calculation packages like Quantum Espresso, the internal stress is calculated using Eq.(3.28) over the Kohn-Sham
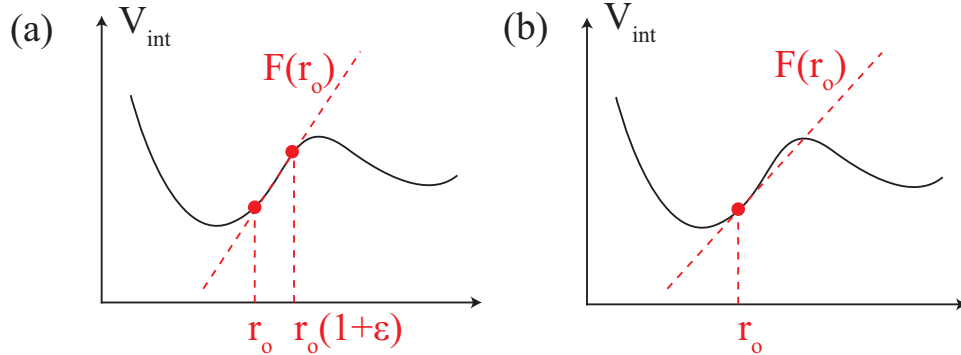
Figure 3.4: The forces $F(r_o)$ due to the interacting potential V_{int} at r_o computed by (a) two eigenvalue problems at r_o and and $(1+\varepsilon)r_o$, and (b) the variational principle.

self-consistent ground states Ψ, determined by the density-functional method [5]. The stress of an unrelaxed structure is

$$\sigma_{\alpha\beta}^{\text{int}} = -\frac{1}{\Omega}\frac{\partial E}{\partial \varepsilon_{\alpha\beta}}\bigg|_{\boldsymbol{\varepsilon}=0} = \frac{1}{\Omega}\sum_i \left\langle \Psi \left| \frac{\hat{p}_\alpha^{(i)}\hat{p}_\beta^{(i)}}{m} - r_\beta^{(i)}\nabla_\alpha^{(i)}\hat{V}_{\text{int}} \right| \Psi \right\rangle. \tag{3.30}$$

Eq.(3.30) is one form of the stress theorem which expresses the total macroscopic stress in terms of the internal operators. The origin of the stress is apparent in Eq.(3.30) as the first term represents the kinematic stress arises from the momentums of the particles, and the second term involves the position atomic position $\mathbf{r}^{(i)}$ and the gradients of the interactions caused by other particles. The stress theorem like in Eq.(3.30) is particularly useful because it allows the force calculations from the current configuration of an $N-$particles system, without solving another $N-$particle eigenvalue problem of a nearby configuration. This idea is shown diagrammatically in Fig. (3.4).

3.2.2 The Quantum Mechanical Stresses and The Generalized Forces in the NEB method

To make the above remark practical in terms of the NEB calculations, we introduce the unit cell structure into the formulation. For a calculating cell structure with the lattice vector $\mathbf{a}$, $\mathbf{b}$, and $\mathbf{c}$, one may define an associating shape tensor $\mathbf{h}$ as

$$\mathbf{h} = \begin{pmatrix} a_1 & b_1 & c_1 \\ a_2 & b_2 & c_2 \\ a_3 & b_3 & c_3 \end{pmatrix}. \tag{3.31}$$

For an atom located at $\mathbf{r} = s_1\mathbf{a} + s_2\mathbf{b} + s_3\mathbf{c}$, the vector $\mathbf{r}$ can be written as

$$\mathbf{r} = \mathbf{hs}, \tag{3.32}$$

where $\mathbf{s} = \{s_1, s_2, s_3\}$ is the vector of the fractional coordinates. Any atomic cell structures can be quantified in terms of a set of fractional vectors $\{\mathbf{s}\}$ and a shape tensor $\mathbf{h}$.

Let assume for the moment that a homogeneous strain ε is applied to the structure. Such transformation does not introduce any internal relaxations; that is the distortion is uniform down to the atomic scale. The homogeneous distortion moves $\mathbf{r}$ to $\mathbf{r}'$ (changes $\mathbf{h}$ to $\mathbf{h}'$, while maintaining $\mathbf{s}$). With the definitions of the shape tensors, the vector $\mathbf{r}$ and $\mathbf{r}'$ can be written as,

$$\mathbf{r} = \mathbf{h}\mathbf{s}, \quad \text{and} \quad \mathbf{r}' = \mathbf{h}'\mathbf{s}. \tag{3.33}$$

The uniform displacement introduced by the ε is

$$\mathbf{u} = \mathbf{r}' - \mathbf{r} = (\mathbf{h}'\mathbf{h}^{-1} - \mathbf{I})\mathbf{r}. \tag{3.34}$$

The forces arising from the internal relaxation which changes the vector$\mathbf{s}$ will be discussed in the Section 3.2.3.

For this homogeneous deformation, the corresponding symmetric strain tensor is [37, 38]

$$\varepsilon = \frac{1}{2}\left[\left(\frac{\partial \mathbf{u}}{\partial \mathbf{r}}\right) + \left(\frac{\partial \mathbf{u}}{\partial \mathbf{r}}\right)^T + \left(\frac{\partial \mathbf{u}}{\partial \mathbf{r}}\right)^T \left(\frac{\partial \mathbf{u}}{\partial \mathbf{r}}\right)\right]. \tag{3.35}$$

Using the above definitions of $\mathbf{h}$ and $\mathbf{h}'$, the symmetric strain tensor is straightforwardly evaluated to

$$\varepsilon = \frac{1}{2}\left(\mathbf{h}^{-T}\mathbf{h}'^T\mathbf{h}'\mathbf{h}^{-1} - \mathbf{I}\right). \tag{3.36}$$

Hence, the strain tensor ε and $\mathbf{h}$ are related by

$$\frac{\partial \varepsilon}{\partial \mathbf{h}'} = \frac{1}{2}\mathbf{h}^{-T}\frac{\partial}{\partial \mathbf{h}'}(\mathbf{h}'^T\mathbf{h}')\mathbf{h}^{-1}, \tag{3.37}$$

where $\mathbf{h}^{-T} = \left(\mathbf{h}^T\right)^{-1}$. The derivative in the above expression can be evaluated using indices notation:

$$\sum_{\nu}\frac{\partial(h'_{\nu\alpha}h'_{\nu\beta})}{\partial h'_{\gamma\kappa}} = \delta_{\alpha\kappa}h'_{\gamma\beta} + \delta_{\beta\kappa}h'_{\gamma\alpha} \tag{3.38}$$

which results in a forth-ranked tensor. The derivative of the strain in Eq.(3.37) becomes

$$\begin{aligned}
\frac{\partial \varepsilon_{\lambda\mu}}{\partial h'_{\gamma\kappa}} &= \frac{1}{2}\left[\sum_{\alpha,\beta}h^{-T}_{\lambda\alpha}\left(\delta_{\alpha\kappa}h'_{\gamma\beta} + \delta_{\beta\kappa}h'_{\gamma\alpha}\right)h^{-1}_{\beta\mu}\right] \\
&\quad \frac{1}{2}\left[h^{-T}_{\lambda\kappa}\sum_{\beta}h'_{\gamma\beta}h^{-1}_{\beta\mu} + h^{-1}_{\gamma\mu}\sum_{\alpha}h^{-T}_{\lambda\alpha}h'_{\gamma\alpha}\right]
\end{aligned} \tag{3.39}$$

Both terms in the right-hand side are equivalent, hence

$$\frac{\partial \varepsilon}{\partial \mathbf{h}'} = \mathbf{h}^{-T} \otimes \mathbf{h}' \cdot \mathbf{h}^{-1}. \tag{3.40}$$

$\vec{\chi}^{\mathbf{h}} = -\mathrm{d}E/\mathrm{d}\mathbf{h}$ computed by the Euler method	$\vec{\chi}^{\mathbf{h}} = \Omega\sigma\mathbf{h}^{-T}$
$\begin{pmatrix} 3.12 & 0.22 & 0.20 \\ -1.4 & 4.49 & -0.13 \\ 0.44 & -0.32 & 3.37 \end{pmatrix}$	$\begin{pmatrix} 3.11 & 0.21 & 0.21 \\ -1.42 & 4.49 & -0.13 \\ 0.43 & -0.32 & 3.36 \end{pmatrix}$
$\begin{pmatrix} -1.13 & -0.09 & -0.15 \\ 2.94 & -6.61 & -0.2 \\ -0.07 & -0.38 & -1.95 \end{pmatrix}$	$\begin{pmatrix} -1.12 & -0.08 & -0.14 \\ 2.92 & -6.60 & -0.19 \\ -0.06 & -0.37 & -1.94 \end{pmatrix}$

Table 3.1: Comparisons of the energy gradients computed by the Euler method and from the quantum mechanical stress, both using Quantum Espresso packages.

Finally, the quantum-mechanical stress in Eq.(3.30) in terms of the change in the cell shape and size is

$$
\begin{aligned}
\sigma &= -\frac{1}{\Omega}\frac{\partial E}{\partial \boldsymbol{\varepsilon}}\Big|_{\boldsymbol{\varepsilon}=0} = -\frac{1}{\Omega}\left(\frac{\partial E}{\partial \mathbf{h}'}\frac{\partial \mathbf{h}'}{\partial \boldsymbol{\varepsilon}}\right)\Big|_{\mathbf{h}'=\mathbf{h}} \\
&= -\frac{1}{\Omega}\left(\frac{\partial E}{\partial \mathbf{h}'}\mathbf{h}^T \otimes \mathbf{h}'^{-1}\mathbf{h}\right)\Big|_{\mathbf{h}'=\mathbf{h}} \\
\sigma &= -\frac{1}{\Omega}\frac{\partial E}{\partial \mathbf{h}}\mathbf{h}^T.
\end{aligned}
\tag{3.41}
$$

Note that the stress is symmetric. Eq.(3.41) constitutes an important relation between the generalized forces $\vec{\chi}^{\mathbf{h}}$ and the mechanical stress σ as

$$
\vec{\chi}^{\mathbf{h}} = -\frac{\partial E}{\partial \mathbf{h}} = \Omega\sigma\mathbf{h}^{-T}
\tag{3.42}
$$

By parameterizing the cell shape by the tensor $\mathbf{h}$, rather that the actual atomic coordinates, the generalized forces can be read directly from the quantum mechanical stress. Numerical results show that the Euler method is more inefficient.

The stresses on variable and anisotropic cells molecular dynamics also take this form [39, 40]. Comparisons between the energy gradients computed by the method of Euler and those obtained from the quantum-mechanical stress are displayed in Table 3.1. Excellent agreement between the generalized forces computed in both methods validates the proceeding theory.

In the case of a solid under a hydrostatic pressure P, the energy of the solid is replaced by the enthalpy $H = E + PV$. The generalized forces are then

$$
\vec{\chi}^{\mathbf{h}} = -\frac{\partial H}{\partial \mathbf{h}} = -\frac{\partial E}{\partial \mathbf{h}} - P\frac{\partial V}{\partial(\mathbf{h})}
\tag{3.43}
$$

The volume of the cell is can be written as $V = \Omega(\mathbf{a} \cdot (\mathbf{b} \times \mathbf{c})) = \Omega \det(\mathbf{h})$. The derivative of the determinant is given by Jacobi formula $\partial \det \mathbf{h}/\partial \mathbf{h} = (\det \mathbf{h})\mathbf{h}^{-T}$. The generalized forces of a solid under an applied hydrostatic stress then becomes

$$\vec{\chi}^{\mathbf{h}} = \Omega(\sigma + P\mathbf{I})\mathbf{h}^{-T}. \tag{3.44}$$

The extension to the case of general stress is possible, and requires some extra care in obtaining the stable structure under the nonhydrostatic state.

These same results are used in the NEB study of the transformation of iron under hydrostatic pressure by Johnson and Carter [29]. However, the physical content of their generalized forces is not provided in their work. Here, we are able to state explicitly the motivation driving to correlate the generalized forces and the quantum mechanical stresses.

There are some remaining degree of freedom due to the internal relaxations which change fractional coordinates $\mathbf{s}$'s. The next section demonstrates that the generalized forces on $\mathbf{s}$'s can be determined directly from the Hellman-Feynman forces.

3.2.3 Quantum-Mechanical Forces

The motivation to evaluate the forces and stresses for a given configuration of nuclei without employing the method of Euler is the elegant work of Feynman [32]. There, it is shown that the problem of calculating the forces between atoms are as simple as calculating the energies by a variational method. The Hellman-Feynman F_α^{HF} force is derived in [32, 41]. For an atom located at $\mathbf{r} = \mathbf{hs}$, the generalized force with respect to $\mathbf{s}$ is

$$\chi_\alpha^{\mathbf{s}} = -\frac{\partial E}{\partial s_\alpha} = -\sum_\beta \frac{\partial E}{\partial r_\beta}\frac{\partial r_\beta}{\partial s_\alpha} = \sum_\beta F_\beta^{\mathrm{HF}} h_{\beta\alpha}. \tag{3.45}$$

The theoretical background to the NEB method and the generalized forces are now finished. From the quantum mechanical theory, it has been derived that the generalized forces in the updating NEB equations can be read directly from self-consistent total energy calculations. The key step is to parameterized the cell structure by the shape tensor $\mathbf{h}$ and the fractional vector $\mathbf{s}$, rather that the atomic positions. For solid-solid transformations, the generalized forces correlate with the stresses and the Hellman-Feynman forces.

In the next chapter, we explore several solid-solid transformations, and emphasize particularly on the BCC-to-HCP transformation in Gum Metal based on the model developed in this chapter.

Chapter 4

Solid-Solid Transformations

The aim of this chapter is to study the Burgers path [26] in Gum Metal. As mentioned in chapter 2, the formation of the giant faults and the nano shearbands are related to the transformation. The chosen computational tool, the nudged-elastic-band (NEB) method, is discussed in detail in chapter 3. In this chapter, we first seek some validations of the method by considering the Bain path in Gum Metal and the Burgers path in sodium (Na). The Bain path constitutes a good test case of the change in the overall shape of structure. The parent (BCC) and product (BCT) phases in such transformation are linked by a uniform deformation gradient, without the shuffling of the basis atoms [42]. For Na, there exists some early attempt to calculate the total-energy of the BCC-HCP transformation from first principles [43], where the energy landscape is described by five order parameters. Our model is less restrictive because the structural change is characterized by twelve parameters: nine for the shape tensor $\mathbf{h}$, and three for the fractional vector of the interior atom $\mathbf{s}$ (described in chapter 3). After these validations, the Burgers path in Ti-V approximants to Gum Metal is discussed.

4.1   The Bain Path in Ti-V Approximant to Gum Metal

The stresses of the Bain path (BCC→ FCC→BCT) in Ti-V approximants to Gum Metal are studied throughly in [6]. By examining the tensile stress associated with the Bain and orthorhombic path, it is reported that Ti-V alloys with less than 0.55 Ti (those with valence electron/atom ratio greater than 4.45) fail in shear along the orthorhombic path even though they initially deform along the Bain path. The maximum tensile stress of the Bain path of the alloys $Ti_{30}V_{70}$ and $Ti_{55}V_{45}$. are 10 GPa are 5 GPa respectively. The uniaxial stresses in [6] are obtained by holding the strain ε_{33} , while adjusting the other five strain components so that the Hellmann-Feynman stresses are less than 0.1 GPa, numerically.

In the BCC structure, the initial state is described by a two-atom conventional unit cell. The lattice vectors are simply $\mathbf{a} = a_{bcc}(1,0,0)$ $\mathbf{b} = a_{bcc}(0,1,0)$, and $\mathbf{c} = a_{bcc}(0,0,1)$. The

shape tensor is thus $\mathbf{h}_{bcc} = a_{bcc}\mathbf{I}$. The two atoms are located at the fractional coordinates $s^I_{bcc} = (0, 0, 0)$ and $s^{II}_{bcc} = (1/2, 1/2, 1/2)$. The fractional coordinates do not change as the structure moves from BCC to BCT. By this choice of the unit cells, the deformation gradient for the transformation simply represents a uniaxial transformation.

4.1.1 Computational Details

We consider the Bain path in $Ti_{25}V_{75}$ using the NEB method. A string of 15 images is constructed from the stable initial BCC and BCT structures. The total energy and generalized forces $\vec{\chi}_\perp + \vec{\chi}_\parallel$ (described in the previous chapter) are obtained from first principles using the Quantum Espresso packages [25]. The pseudopotentials of the Ti-V approximants are the virtual crystal potential [6]. To converge the energy, the k-point mesh of $12 \times 12 \times 12$ and the energy cutoff of 100 Ry are employed. In the final relaxation step, the energy converge to less than 0.007 mRy/atom, and the generalized forces $\left|\vec{\chi}_\perp + \vec{\chi}_\parallel\right|$ on the images are less than 0.01 mRy/au. The springs connecting the images have the strength of 0.15 Ry/au^2. The minimum forces are obtained by the steepest descent method, where the key quantity in updating and ultimately optimizing the band is the quantum-mechanical stress and the Hellman-Feynman forces. The tangents to coordinates describing the cell shape are parameterized by nine interpolating cubic spline functions, one for each component of the shape tensor $\mathbf{h}$.

4.1.2 Computer Results

To characterize the progress of the BCC-to-BCT transformation, a reaction coordinate ω_i is introduced as: $\omega_i = \left((\mathbf{X}_i - \mathbf{X}_o).(\mathbf{X}_f - \mathbf{X}_o)\right)^{1/2} / |\mathbf{X}_f - \mathbf{X}_o|$, where the nine-dimensional vector $\mathbf{X}_i$ contains the components of shape tensor $\mathbf{h}$ defined in chapter 3. Since the transformation is uniform, the fractional vector $\mathbf{s}$ does not vary with the images. By this definition, the BCC-BCT transformation is complete when $\omega_i = 1$.

The energies of the Bain path are displayed in Fig. 4.1. The energies are plotted against both the image labels and the reaction coordinates. Note that the shape of the curve shows a saddle point similar to energy function of the relaxed $\langle 001 \rangle$ tensile strain for Mo and Nb [42]. The activation energy from BCC to BCT is ~ 140 meV/atom, while for BCT to BCC it is ~ 60 meV/atom. The saddle point corresponds to the FCC structure. The the tensile stress σ_{33} as a function of the image labels and the elongation strain ϵ_{33} are displayed in Fig.(4.2). The maximum tensile stress is ~ 10 GPa, comparable to that of $Ti_{20}V_{80}$ in [6].
.
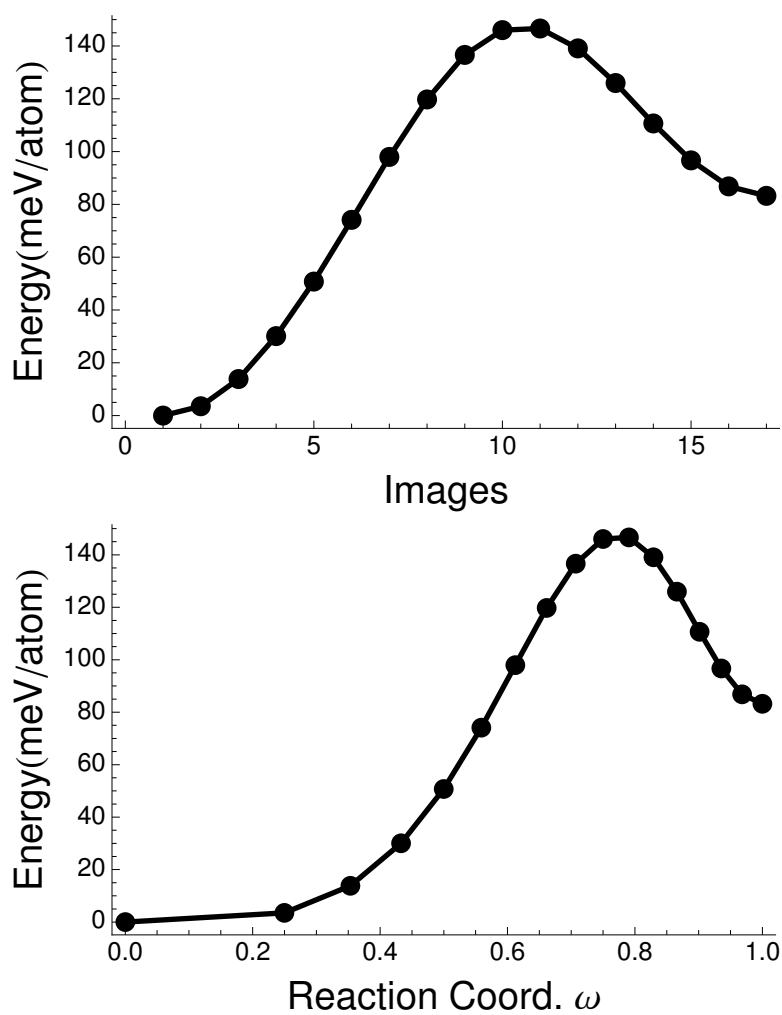
Figure 4.1: The energy of the bain path of $Ti_{25}V_{75}$ alloy as a function of (a) the image labels (b) the reaction coordinates ω as defined in the text.
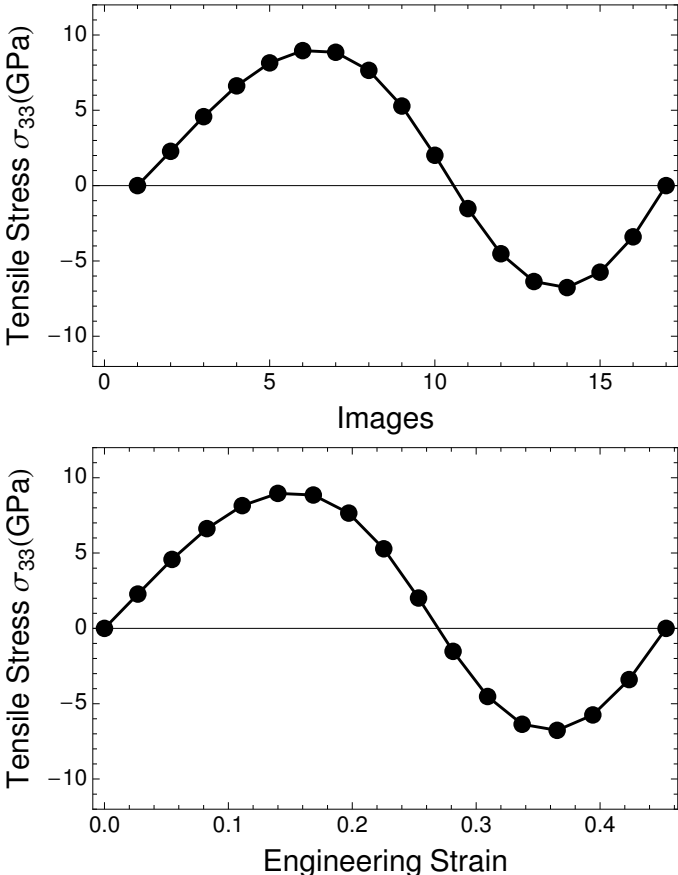
Figure 4.2: The tensile stress of the bain path of $Ti_{25}V_{75}$ alloy as a function of (a) the image labels (b) the engineering strain.
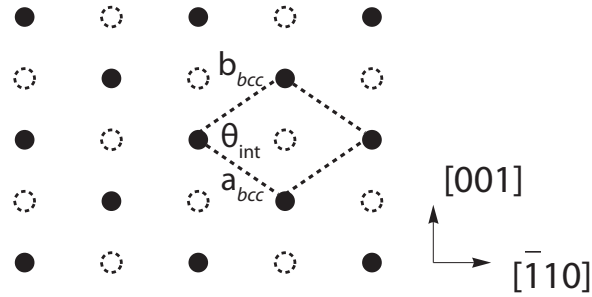
Figure 4.3: The unit cell for the BCC-to-HCP transformation.

4.2   The Burgers Path in Sodium

The pressure-temperature phase diagram of Na reveals the BCC-to-HCP transition at about 0.1-0.2 GPa at zero temperature [44]. The BCC structure is stable above 0.1 GPa. The BCC-to-HCP transformation result from the atomic shuffling and and a uniform deformation gradient [26]. From a first-principles calculations, Ye *et al* have shown that the HCP phase is lower than the BCC phase in energy by 1.0 meV/atom, with a barrier height of only 0.6 meV/atom [28]. It is also found the c/a ratio of the HCP phase is nearly the same as that of the BCC phase. Along the BCC→HCP transformation path, the value c/a grows rapidly, indicating that the distance between the horizontal planes of HCP cell increases, then returns to almost the original value when the transformation is complete. The atomic shuffle does not occur until *after* the c/a ratio reaches a plateau. The reported maximum value of c/a is ~ 1.655. Here, we consider these properties using the NEB method.

Unlike the BCC-BCT transformation, the BCC-HCP transformation cannot be be described within the conventional cubic cell. Instead, the transition is best represented by defining the unit cell of the BCC structure projected on a $\{110\}$ plane with the lattice vectors of $\mathbf{a}_{bcc} = a_o(1, 0, 0)$, $\mathbf{b}_{bcc}, a_o(1/3, 2\sqrt{2}/3, 0)$, and $\mathbf{c}_{bcc} = a_o(0, 0, 2\sqrt{6}/3)$, where $a_o = \sqrt{3}a_{bcc}/2$. An illustration of the basal plane of the unit cell is shown in Fig. 4.3.

In chapter 2, it is shown that the Burgers path is led by a pure shear close to $\langle 111 \rangle \{112\}$ slip system (Fig. 2.7). In addition to a pure shear, one may envision a complementary volume expansion and an elongation along the $z-$axis:

$$\mathbf{F}_\alpha = (1 + \alpha) \begin{pmatrix} 1 & 0 & 0 \\ 0 & 1 & 0 \\ 0 & 0 & 1 \end{pmatrix} \quad \text{and} \quad \mathbf{F}_\zeta = \begin{pmatrix} 1 & 0 & 0 \\ 0 & 1 & 0 \\ 0 & 0 & 1+\zeta \end{pmatrix}. \tag{4.1}$$

The remaining three degree of freedoms are the shuffle of the interior atom. By this choice

of the unit cell, the fractional coordinate of the BCC and HCP structures are

$$\mathbf{s}_{bcc}^{I} = (0,0,0) \quad \text{and} \quad \mathbf{s}_{bcc}^{II} = \left(\frac{1}{2}, \frac{1}{2}, \frac{1}{2}\right)$$

$$\mathbf{s}_{hcp}^{I} = (0,0,0) \quad \text{and} \quad \mathbf{s}_{hcp}^{II} = \left(\frac{1}{3}, \frac{1}{3}, \frac{1}{2}\right). \tag{4.2}$$

As discussed in chapter 2, the transformation $\mathbf{s}_{bcc}^{II} \to \mathbf{s}_{hcp}^{II}$ is led by the soft $N-$point phonon.

4.2.1 Computational Details

The structure of Na is obtained from first-principles calculations using the Quantum Espresso packages. The Perdew-Burke-Ernzerhof (PBE) pseudopotential is employed. To converge the energy, the k-point mesh is set to $16 \times 16 \times 10$, while the energy cutoff is 80 Ry. The total energy converges to less than 0.006 mRy/atom. In the final optimizing step, the generalized force $\vec{\chi}_{\perp} + \vec{\chi}_{\parallel}$ on each image converges to less than 0.1 mRy/au. The spring constants are 0.15 Ry/au². Here, we use the steepest descent method to search for the zero of $\left|\vec{\chi}_{\perp} + \vec{\chi}_{\parallel}\right|$. The tangents to the parameters describing the cell structures are represented by twelve interpolating cubic spline functions, one for each component of $\mathbf{h}$ and $\mathbf{s}$ (defined in chapter 3).

4.2.2 Computer Results

To characterize the progress of the BCC-to-HCP transformation, a new reaction coordinate ω_i is introduced as: $\omega_i = \left((\mathbf{X}_i - \mathbf{X}_o).(\mathbf{X}_f - \mathbf{X}_o)\right)^{1/2} / |\mathbf{X}_f - \mathbf{X}_o|$, where the twelve-dimensional vector $\mathbf{X}_i$ contains the components of shape tensor $\mathbf{h}$ and the shuffle $\mathbf{s}$ defined in chapter 3. The BCC-HCP transformation is complete when $\omega_i = 1$.

Predicted energies and other properties along the BCC-HCP transformation path under varying ambient pressure conditions are displayed in Fig. 4.4. Given that such transformation involves a collective motion of the transformation region, the small activation energy per atom allows such transformation to occur. Consistent with the *P-T* phase diagram, the HCP phase is found to to be at lower energy than the BCC phase. The energy of the HCP phase rises to the value comparable to that of the BCC structure as the ambient pressure increases.

The change of the c/a ratio along the entire minimum energy path indicates rather significant deviation from the ideal ratio. The BCC and HCP phases have almost the same c/a value. We see that the ratio grows rapidly, indicating that the distance between the horizontal atomic planes is increasing. It then returns to the value close to that of the BCC structure when the transformation is complete. The maximum value of c/a in this calculation is ~ 1.652, comparable to $(c/a)_{max} \sim 1.655$ in [28]. The maximum c/a reduces with the ambient pressure as expected.
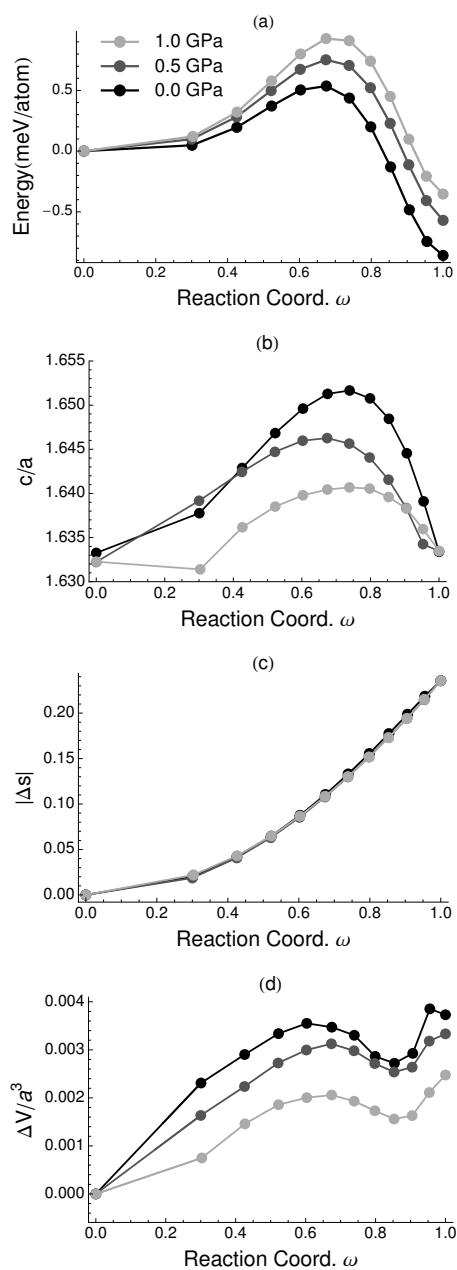
Figure 4.4: The energies and other properties of the Burgers path of sodium

Fig. 4.4 (c) show the magnitude of the change in fractional coordinate $\Delta \mathbf{s}$ as a function of the reaction coordinates. The atomic positions are located $\mathbf{r} = \mathbf{hs}$, where $\mathbf{h}$ quantifies the cells structure. The value $|\Delta \mathbf{s}|$ is measured from the BCC structure, hence representing the internal relaxations during the transformation. Fig. 4.4 reveals that $|\Delta \mathbf{s}|$ is independent to the amount of the ambient pressure. Furthermore, in contrast to [28], our result shows that the phonon displacements change from the beginning of the transformation This is due to the unconstraint volume in our calculations, as compared to the constraint ones in [28]. The change in volume of the structure is shown in Fig. 4.4.

4.3 The Burgers Path in a Ti-V Approximant to Gum Metal

4.3.1 Computational Details

The structure of Ti_{75} V_{25} (a Gum Metal approximant) is considered in this section. The total energy and generalized forces are obtained from first principles calculations using the Quantum Espresso packages [25]. The same pseudopoential as one in the study of the Bain path calculations is employed. To converge the energy, the k-point mesh of $21 \times 21 \times 13$ and the energy cutoff of 80 Ry are used. The total energy converges to less than 0.004 mRy/atom. In the relaxed chain, the force on each image converges to less than 1 mRy/au. The fictitious spring constants are 1 Ry/au^2. The forces on the images are optimized by the steepest descent method, while the tangential vectors are obtained as those for calculating the Burgers path of sodium.

Preliminary results reveal that the HCP phase is barely stable. This poses some challenge in searching for a minimum energy path. The issue is resolved by including more images into the calculations. Initial ten images are optimized by the steepest descent method, then other ten images are inserted close to the HCP configuration. The overall chain of images is then optimized again until the desired force convergence is achieved.

4.4 Computer Results

The reaction coordinates ω_i have the same meaning as in the previous section. The energies and other properties of the path at zero pressure are shown in Fig. 4.5. The insets magnify the curves near the HCP phase. Fig. 4.5(a) shows the energy per atom during transformation, where we see that the energy varies smoothly, with a large BCC→HCP activation energy ($\Delta E_{bcc \to hcp} \sim 57$ meV/atom), but extremely small for the HCP→BCC transformation ($\Delta E_{hcp \to bcc} \sim 0.45$ meV/atom). Note that the energy convergence in these calculations is better than 0.05 meV/atom. The energy of the path shows that the HCP phase is barely stable with respect to the BCC.

The internal relaxations $|\Delta\mathbf{s}|$ are shown in Fig. 4.5. The amplitudes increase smoothly from the BCC phase. As for HCP→BCC transformation, Fig. 4.5(b) and (c) reveal that the scaled amplitudes $|\Delta\mathbf{s}|$ do not change much until the shear reaches a certain value. The angle θ_{int} measures the basal plane angle between the vector $\mathbf{a}_{bcc}$ an $\mathbf{b}_{bcc}$ defined in Fig. 4.3. As the structure changes BCC to HCP, this angle varies from 70.53° to 60°. The HCP structure is slightly sheared prior to atomic relaxations to take effects. Much of the activation energy $\Delta E_{hcp\rightarrow bcc}$ goes into adjusting the overall shape of the HCP phase to initiate internal relaxations.

Fig. 4.5(b) shows the c/a ratio as a function of the reaction coordinates. Like the transformation path in Na, there is a maximum c/a ratio along the path. The value of $(c/a)_{\max}$ is 1.652. The relaxed HCP phase has a very different c/a compared to that of the BCC phase. The structure of the BCC phase adjusts so that its $c/a \sim 1.632$ reaches 1.641 in the HCP phase. The change in the c/a ratio also plays a role in initiating the internal relaxations when considering HCP→BCC transformation. After critical amounts of the changes in shear and c/a ratio are achieved, the scaled amplitudes start to change more dramatically.

It should be noted that our study neglects the finite-temperature effects and the entropic terms in the free energy. The activation energy reported here is the energy per atom. The collective motions of a many-atoms system ultimately represent the real activation energy for precipitating out a new phase.

In connection with our previous discussion of the formation of giant faults and nano shearbands in chapter 2, the HCP phase more easily flops into the the BCC phase, while the reverse transformation is harder. Our results reveal that only the changes in shear and c/a ratio of the overall structure constrain the HCP phase. Certain amounts of shear are required to maintain the HCP structure in this Ti-V approximant to Gum Metal. This finding agrees with our previous hypothesis that the structure of the giant faults and nano shearbands arise only because of the compatibility condition during deformations.

Furthermore, the structure of the α'' phase may be viewed as the transition state from the HCP (α') to the BCC structure (β phase) [45]. The energies along the Burgers path show that, in the Ti-V approximant to Gum Metal and at zero temperature, this phase is unstable. Within this first principles study, we conclude that the appearance of the α'' diffraction spots in Fig. 2.6 is caused by the $N-$point phonon vibrations.

In summary, we have shown that the HCP $Ti_{75}V_{25}$ is barely stable with respect to the BCC formation. Much of the consumed energy in the HCP→BCC transition goes into changing the overall shape and c/a ratio of the HCP phase before the internal relaxation starts to take effects. The microstructures of the giant faults and nano shearbands arise from this constraint to the HCP phase. Our theoretical findings are tested by comparative studies of the Bain path in Ti-V alloys and the Burgers path in sodium.
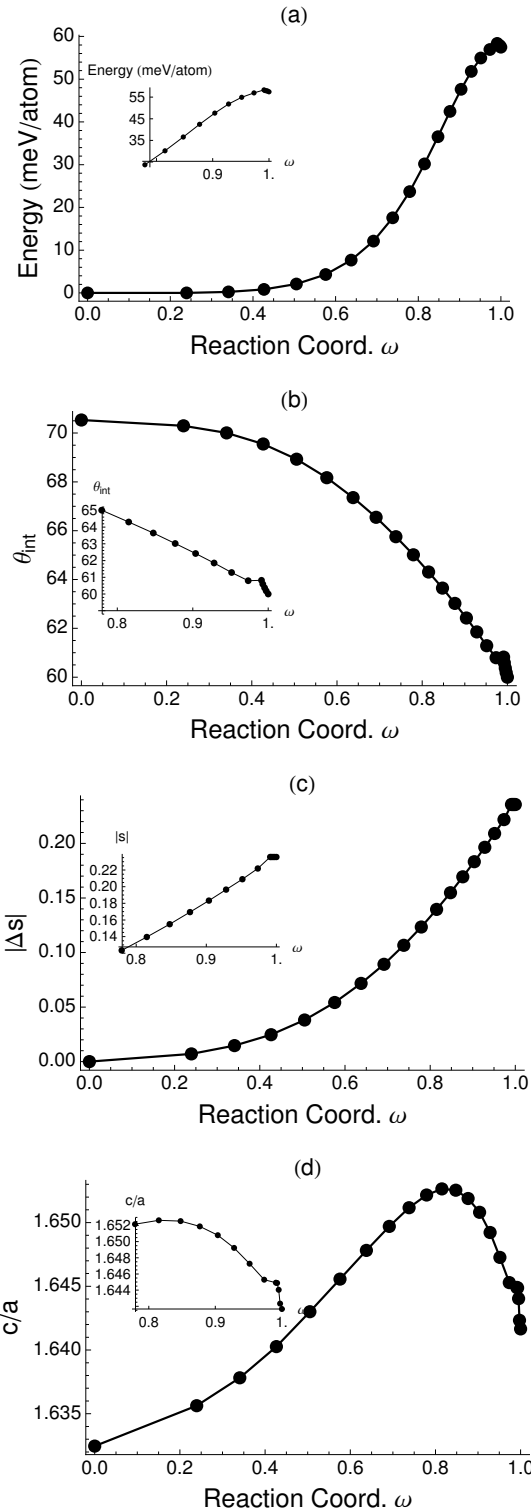
Figure 4.5: The energies and other properties of the Burgers path of Ti$_{75}$ V$_{25}$.

Chapter 5

Solute-Dislocation Interactions in Fe-C Alloys

5.1 Carbon-Dislocation Interaction in Steels

Imaging the solute atmosphere of carbon atoms in ferritic Fe-C alloys has been made possible only recently using atom probe tomography [9]. The extent of spreading of the solute atmosphere is on the order of 10 nm, while the enrichment factor, the ratio of the concentration of solute in the neighborhood of the dislocation over the matrix concentration, is approximately 7.7 (within the considered region). Both the extent of spreading and concentration of solute atoms implies that much of the atmosphere resides far from the elastic singularity of the core (the region within approximately one Burgers vector of the core, where bonding topology differs substantially from the bulk crystalline counterparts). In regions remote from the core, elasticity theory should be suitable for predicting defect interactions and carbon solute atmospheres.

Elasticity theory of carbon-solute/dislocation interactions has been extensively studied. Cochardt *et al* [46] studied the interaction using isotropic linear continuum elasticity theory to describe the dislocations. A similar theory was formulated by Bacon [47], where the tetragonal distortion of the interstitial solute was modeled as an elastic dipole tensor. Anisotropic linear continuum elasticity theory was later employed in the work by Douthwaite [48]. The most recent published work represents a conjunction of elasticity theory and atomic scale simulations [49].

The maximum solute-dislocation interaction energies from these models are summarized in Table 5.1. Note that the predicted maximum of the solute interaction energy with screw dislocations based on elasticity theory is about 75% of that for edge dislocations. Also, the variation of the maximum interaction energies within these studies varies by more than a factor of two. Clearly, further detailed theoretical studies of solute-dislocation interaction and solute atmospheres are still needed.

References	Dislocation Type	Dislocation Models	Distortion Type	Maximum Interaction Energy (eV)
[50]	Edge	Isotropic	Isotropic	-
[46]	Edge, screw	Isotropic	Tetragonal	0.75, 0.75
[47]	Edge, screw	Isotropic	Tetragonal	0.49, 0.37
[48]	Screw	Anisotropic	Tetragonal	0.60
[49]	Edge, screw	Anisotropic	Tetragonal	0.40, 0.30

Table 5.1: Elasticity theory predictions of solute-dislocation interaction energies. The maximum interaction energy is calculated at $r = |\mathbf{b}|$

Differences in the maximum interaction energies reported in Table 5.1 stem from two sources; variations in (1) the assumed elastic constants, and (2) the amount of distortion induced by a carbon interstitial.

Experimentally, there have been attempts to measure the lattice distortion induced by a single solute atom. Typically, the lattice parameter of Fe-C martensite is used to measure the strain. A large variation of data on lattice parameter changes with carbon content have been observed [51]. The scatter arises from experimental errors due to different methods employed for lattice parameter determination and the existence of residual stresses from quenching the austenite that might suppress lattice parameter changes. Another possible source of error is the effect of equivalent interstitial sites. Since carbon atoms can fill one of the three equivalent octahedral sites in the BCC iron, the resultant average deformation may trend toward isotropic, rather than tetragonal. Despite these issues, experimental results appear to have converged. Figure 5.1 replots the data from references [52, 53, 54] as considered and plotted by [51]. The experiments indicate that the lattice parameters of Fe-C alloys depend linearly on C composition for the studied range.

Theoretically, the most fundamental study of defect interactions is due to Eshelby [55, 56]. Eshelby has shown that the tetragonal solute-dislocation interaction energy is the product of the strength of the point source and the strain field produced at the point source by the dislocation. In this work, we revisit this model and show that Eshelby's formulation can be complemented by first principle calculations based on density functional theory (DFT) [5]. Specifically, the strength of the point source and the elastic constants entering Eshelby's expressions can be computed directly using electronic structure based total energy methods. Further, electronic structure methods can be used to compute the segregation energy directly. This more direct approach yields the correct continuum limit and can, potentially, reveal chemical and magnetic contributions to the interaction beyond those already reflected within the elastic constants and distortion tensor. Further, the direct approach may be extended to high strain situations, where linear elasticity theory may no longer be valid.

The theoretical basis of the calculations is developed in Section 5.2 and 5.3. The *ab initio* calculations and results for a dilute Fe-C alloy are described in Section 5.4. In Section 5.5,
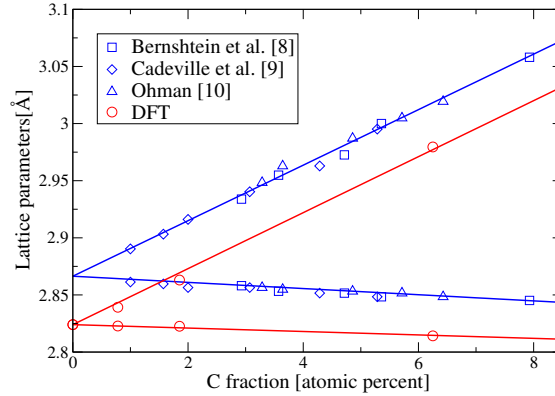
Figure 5.1: Least-square fits of lattice parameters(a and c) computed from first principles as functions of the number of carbon atoms. The least-square fits of experimental data are also plotted. The calculated and experimental data are not scaled to the same origin.

the theory is used to compute the distribution of carbon solute atoms around edge and screw dislocations in Fe.

5.2 Solute-Dislocaton Interactions from The Strength of Point Defects

Eshelby has shown that by regarding the solute atom as a point source of stress, particularly for one where the forces are unequal along the horizontal and vertical axes [55], the interaction energy of the solute and the dislocation is

$$F^{int} = -\Gamma^o_{ij} \Delta^d_{ij}, \tag{5.1}$$

where Γ^o_{ij} is the strength of the point source, and Δ^d_{ij} is the distortional field produced at the source by the dislocation. The strength of the source Γ^o_{ij} is sometimes refered to as elastic dipole moment [22, 57]. It is a function of the electronic structure differences and bonding between the host atoms and the solute atom.

In principle, computing Γ^o_{ij} using atomic scale approaches should be straightforward. One simply includes an interstitial atom within an Fe crystal, and measures the displacements of the atoms within the crystal. In practice, however, the procedure is more complex. The best electronic structure based total energy methods are computationally expensive and work best for periodic systems. Hence the computation of segregation energy is most conveniently carried out using supercells and periodic boundary conditions. The relationship between periodic supercells and the desired quantities, however, can be obtained readily. The remainder of this section demonstrates that strength of the point source can be computed using an *ab inito* total energy calculation using a periodic boundary condition.

Total energy calculations usually employ periodic boundary conditions. The elastic and chemical energy computed in this type of boundary conditions is discussed extensively in [58, 2, 59]. Consider a solid modeled using a supercell of volume Ω. If a stress-free boundary condition is imposed, and in the limit of large Ω, insertion of a solute atom into an interstitial site within the supercell approximates a dilute Fe-C alloy. Insertion of the solute atom while not allowing relaxation leads to an elastic stress. The subsequent structural relaxation reduces the elastic energy. The relaxed energy per unit volume, $\Delta\phi$, can be approximated as a Taylor series in the solute distortion $\Delta^c_{\alpha\beta}(\mathbf{r}) = \partial_\beta u^c_\alpha(\mathbf{r})$ as

$$\Delta\phi = \left(\frac{\partial\phi}{\partial\Delta^c_{\alpha\beta}}\right)_o \Delta^c_{\alpha\beta} + \frac{1}{2}\left(\frac{\partial\phi}{\partial\Delta^c_{\alpha\beta}\partial\Delta^c_{\gamma\kappa}}\right)_o \Delta^c_{\alpha\beta}\Delta^c_{\gamma\kappa} + \mathcal{O}(\Delta^3) \tag{5.2}$$

where the subscript o indicates the derivative at zero distortion, and the Einstein summation convention is adopted. By definition,

$$\sigma^o_{\alpha\beta} = \left(\frac{\partial\phi}{\partial\Delta^c_{\alpha\beta}}\right)_o, \quad \text{and} \quad c_{\alpha\beta\gamma\kappa} = \left(\frac{\partial\phi}{\partial\Delta^c_{\alpha\beta}\partial\Delta^c_{\gamma\kappa}}\right)_o, \tag{5.3}$$

where $\sigma^o_{\alpha\beta}$ is the strain-free stress required to restore the perfect crystal reference state and the $c_{\alpha\beta\gamma\kappa}$ are the elastic constants. The first term in the right hand side of Eq. (5.2) is the energy required to take a single solute from a standard state and insert it into Ω without displacement of the host atoms.

The net relaxation energy due to the presence of a solute is

$$\Delta F = \int_\Omega \mathrm{d}^3\mathbf{r}\Delta\phi = \int_\Omega \mathrm{d}^3\mathbf{r}\left(\sigma^o_{\alpha\beta}\Delta^c_{\alpha\beta} + \frac{1}{2}c_{\alpha\beta\gamma\kappa}\Delta^c_{\alpha\beta}\Delta^c_{\gamma\kappa}\right). \tag{5.4}$$

Defining a body force distribution $f^c_\alpha \equiv -\partial_\beta\sigma^c_{\alpha\beta}$, that is $f^c_\alpha = -c_{\alpha\beta\gamma\kappa}\partial_\beta\Delta^c_{\gamma\kappa} = \partial_\beta\sigma^o_{\alpha\beta}$ and employing the identities $\partial_\beta(\sigma^o_{\alpha\beta}u^c_\alpha) = \partial_\beta\sigma^o_{\alpha\beta}u^c_\alpha + \sigma^o_{\alpha\beta}\partial_\beta u^c_\alpha$, and $\int_{\partial\Omega}\mathrm{d}S(\sigma^o_{\alpha\beta}u_\alpha n_\beta) = 0$, the relaxation energy is

$$\Delta F = \int_\Omega \mathrm{d}^3\mathbf{r}\left(-f^c_\alpha u^c_\alpha + \frac{1}{2}c_{\alpha\beta\gamma\kappa}\Delta^c_{\alpha\beta}\Delta^c_{\gamma\kappa}\right). \tag{5.5}$$

For a repeating supercell structure or a dilute Fe-C concentration considered here

$$f^c_\alpha(\mathbf{r}) = \frac{1}{\Omega}\sum_\mathbf{K} \tilde{f}_\alpha(\mathbf{K})e^{i\mathbf{K}\cdot\mathbf{r}}, \tag{5.6}$$

where $\tilde{f}_i(\mathbf{K}) = \int_\Omega f^c_i(\mathbf{r})e^{-i\mathbf{K}\cdot\mathbf{r}}dV$, and $\mathbf{K}$ is a reciprocal lattice vector. For a large volume Ω, the magnitude of $\mathbf{K}$ is considered to be small. Hence $\tilde{f}_i(\mathbf{K})$ can be expanded to the first nonvanishing term in a Taylor series expansion in $\mathbf{K}$ as

$$\tilde{f}_\alpha(\mathbf{K}) = \int_\Omega \mathrm{d}^3\mathbf{r}f^c_\alpha(\mathbf{r})\left(1 - iK_\beta r_\beta + ...\right). \tag{5.7}$$

Since the crystal has inversion symmetry around the origin taken to coincide with the solute atom position, the body force $f_\alpha^c(\mathbf{r})$ acquires the symmetry $f_\alpha^c(-\mathbf{r}) = -f_\alpha^c(\mathbf{r})$, which enables us to write

$$\tilde{f}_\alpha(\mathbf{K}) = -iK_\beta \int_\Omega \mathrm{d}^3\mathbf{r} f_\alpha^c(\mathbf{r}) r_\beta + O(K^3) = -iK_\beta \Omega \bar{\Gamma}_{\alpha\beta} + O(K^3), \qquad (5.8)$$

where $\Omega\bar{\Gamma}_{\alpha\beta} \equiv \int_\Omega \mathrm{d}^3\mathbf{r} f_\alpha^c r_\beta$. The term $\Omega\bar{\Gamma}_{\alpha\beta}$ has appeared in the literature [22, 57] as the elastic dipole moment of a point source. It can be easily shown that the body force $f_\alpha^*(\mathbf{r}) = -\Gamma_{\alpha\beta}^o \partial_\beta \delta(\mathbf{r})$ yields same Fourier components as in Eq. (5.8), except only for the higher order terms [55]. By replacing $f_\alpha^c(\mathbf{r})$ with $f_\alpha^*(\mathbf{r})$, the relaxation energy is

$$\Delta F = \int_\Omega \mathrm{d}^3\mathbf{r} \left(-\Gamma_{\alpha\beta}^o \delta(\mathbf{r})\Delta_{\alpha\beta}^c + \frac{1}{2}c_{\alpha\beta\gamma\kappa}\Delta_{\alpha\beta}^c\Delta_{\gamma\kappa}^c \right), \qquad (5.9)$$

where the identity $\int_\Omega \mathrm{d}^3\mathbf{r}\partial_\alpha(\delta(\mathbf{r})u_\alpha^c) = \int_\Omega \mathrm{d}^3\mathbf{r}\partial_\beta\delta(\mathbf{r})u_\alpha^c + \int_\Omega \mathrm{d}^3\mathbf{r}\delta(\mathbf{r})\partial_\beta u_\alpha^c = 0$ is used. The relaxation energy then resembles relaxation of a concentrated stress source

$$\sigma_{\alpha\beta}^o = -\Gamma_{\alpha\beta}^o\delta(\mathbf{r}), \qquad (5.10)$$

located at the origin, as noted by Daw [59].

The distortional field can be written in terms of the Fourier summation

$$\Delta_{\alpha\beta}^c(\mathbf{r}) = \frac{1}{\Omega}\sum_\mathbf{K}\tilde{\Delta}_{\alpha\beta}^c(\mathbf{K})e^{i\mathbf{K}\cdot\mathbf{r}}, \qquad (5.11)$$

where $\tilde{\Delta}_{\alpha\beta}^c(\mathbf{K}) = \int_\Omega \mathrm{d}^3\mathbf{r}\Delta_{\alpha\beta}^c(\mathbf{r})e^{-i\mathbf{K}\cdot\mathbf{r}}$. In terms of the variable $\mathbf{K}$, the relaxed energy is

$$\Delta F = \frac{1}{2\Omega}\sum_\mathbf{K}c_{\alpha\beta\alpha\kappa}\tilde{\Delta}_{\alpha\beta}^c(\mathbf{K})\tilde{\Delta}_{\gamma\kappa}^{c*}(\mathbf{K}) - \frac{1}{\Omega}\sum_\mathbf{K}\Gamma_{\alpha\beta}^o\tilde{\Delta}_{\alpha\beta}^{c*}(\mathbf{K}). \qquad (5.12)$$

The considered supercell does not contain any dislocations, hence it is curl free. Daw [59] has shown that the solution of the distortional field for $\mathbf{K} \neq 0$ term has the form

$$\tilde{\Delta}_{\alpha\beta}^c = K_\alpha\left[\mathbf{A}^{-1}\right]_{\beta\kappa}\Gamma_{\gamma\kappa}^o K_\gamma, \qquad (5.13)$$

where $A_{\beta\kappa} = c_{\alpha\beta\gamma\kappa}K_\alpha K_\gamma$. For the $\mathbf{K} = 0$ term or $\tilde{\Delta}_{\alpha\beta}^o$, the solution can be determined by minimizing the relaxed energy with respect to $\tilde{\Delta}_{ij}^o$ yielding

$$c_{\alpha\beta\gamma\kappa}\tilde{\Delta}_{\gamma\kappa}^o = \Gamma_{\alpha\beta}^o, \quad \text{or} \quad \tilde{\Delta}_{\alpha\beta}^o = s_{\alpha\beta\gamma\kappa}\Gamma_{\gamma\kappa}^o. \qquad (5.14)$$

Eq. (5.14) shows that the strength of the elastic field of a point source of dilation is related to the shape and volume changes of the relaxed periodic structures. Therefore, it can be
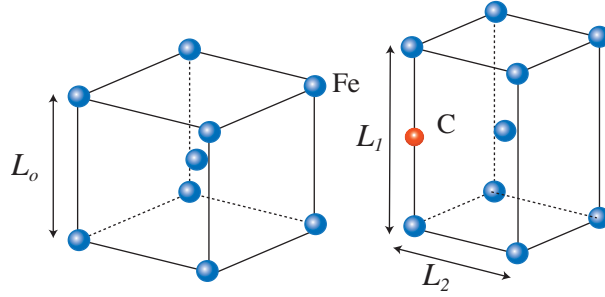
Figure 5.2: One of the three variants of the tetragonal distortion of Fe by a C atom.

determined from homogeneous relaxation of the supercell with respect to both the internal coordinates and the supercell dimensions.

Consider the first variant of the solute field as shown in Figure 5.2. The C atom is inserted into an x_1-type octahedral interstitial site ($\Gamma^o_{\alpha\beta} = \Gamma^{o(1)}_{\alpha\beta}$). The changes in supercell lattice parameters L_1, L_2, and L_3 are

$$\Delta L_1 = \int_0^{L_o} dx_1 \Delta^c_{11}(x_1, 0, 0), \quad \Delta L_2 = \int_0^{L_o} dx_2 \Delta^c_{22}(0, x_2, 0), \tag{5.15}$$

with $\Delta L_2 = \Delta L_3$ by symmetry. In terms of the Fourier-transform variable $\mathbf{K}$, Eq. (5.15) becomes

$$\Delta L_1 = \frac{L_o}{\Omega} \sum_{K_2, K_3} \tilde{\Delta}^c_{11}(0, K_2, K_3), \quad \Delta L_2 = \frac{L_o}{\Omega} \sum_{K_1, K_3} \tilde{\Delta}^c_{22}(K_1, 0, K_3). \tag{5.16}$$

It can be shown that the terms $\tilde{\Delta}^c_{11}(0, K_2, K_3)$ and $\tilde{\Delta}^c_{22}(K_1, 0, K_3)$ vanish for every $\mathbf{K} \neq 0$. The strength of the dipole moment thus relates to the relaxed strains ε^T_1 and ε^T_2 by

$$\varepsilon^T_1 = \frac{\Delta L_1}{L_o} = \frac{1}{\Omega} s_{11\alpha\beta} \Gamma^{o(1)}_{\alpha\beta}, \quad \text{, and} \quad \varepsilon^T_2 = \frac{\Delta L_2}{L_o} = \frac{1}{\Omega} s_{22\alpha\beta} \Gamma^{o(1)}_{\alpha\beta}. \tag{5.17}$$

Eq. (5.17) can be inverted to determine components of $\Gamma^{o(1)}_{\alpha\beta}$. Performing the inversion, one finds

$$\Gamma^o_{11} = \Omega \left[C_{11}\varepsilon^T_1 + 2C_{12}\varepsilon^T_2 \right], \quad \text{and} \quad \Gamma^o_{22} = \Omega \left[C_{11}\varepsilon^T_1 + C_{12}(\varepsilon^T_1 + \varepsilon^T_2) \right]. \tag{5.18}$$

If Vegard's law holds, the change of the supercell lattice parameters are linear in the interstitial mole fraction of the solute n or

$$
\begin{aligned}
L_1(n) &= L_o + n \frac{dL_1}{dn}\bigg|_{n=0} \\
L_2(n) &= L_o + n \frac{dL_2}{dn}\bigg|_{n=0}.
\end{aligned}
\tag{5.19}
$$

The relaxed strains are thus

$$\varepsilon_1^T = n\eta^c, \quad \text{and} \quad \varepsilon_2^T = n\eta^a, \tag{5.20}$$

where η^c and η^a are the relative changes in the supercell lattice parameters with respect to an insertion of a carbon solute atom, given by

$$\eta^c = \frac{1}{L_o}\frac{dL_1}{dn}\bigg|_{n=0}, \quad \text{and} \quad \eta^a = \frac{1}{L_o}\frac{dL_2}{dn}\bigg|_{n=0}. \tag{5.21}$$

Also, in BCC crystals the number of the host atoms is equal to the number of the primitive cells. An insertion of a single solute into one of the octahedral interstices leads to

$$n\Omega = v_o, \tag{5.22}$$

where v_o is the primitive cell volume. We now substitute Eq. (5.20) and (5.22) into Eq. (5.18) to find

$$\Gamma_{11}^o = v_o\left(C_{11}\eta^c + 2C_{12}\eta^a\right), \quad \text{and} \quad \Gamma_{22}^o = v_o\left(C_{11}\eta^c + C_{12}(\eta^c + \eta^a)\right). \tag{5.23}$$

Eq. (5.23) can be written more compactly by collecting η^c and η^a into a relative transformation tensor

$$\boldsymbol{\eta}^{(1)} = \begin{pmatrix} \eta^c & 0 & 0 \\ 0 & \eta^a & 0 \\ 0 & 0 & \eta^a \end{pmatrix}, \tag{5.24}$$

which, for a cubic material, enables us to write

$$\Gamma_{\alpha\beta}^{o(1)} = \Omega c_{\alpha\beta\gamma\kappa}\eta_{\gamma\kappa}^{(1)}n = v_o c_{\alpha\beta\gamma\kappa}\eta_{\gamma\kappa}^{(1)}. \tag{5.25}$$

Finally, substitution of Eq. (5.25) into Eq. (5.1) leads to

$$F^{int(1)} = -v_o c_{\alpha\beta\gamma\kappa}\eta_{\gamma\kappa}^{(1)}\Delta_{\alpha\beta}^d, \tag{5.26}$$

which relates the interaction energy directly to the lattice contraction and expansion of the relaxed structure.

The relative transformation tensors of the other two variants are

$$\boldsymbol{\eta}^{(2)} = \begin{pmatrix} \eta^a & 0 & 0 \\ 0 & \eta^c & 0 \\ 0 & 0 & \eta^a \end{pmatrix}, \quad \text{and} \quad \boldsymbol{\eta}^{(3)} = \begin{pmatrix} \eta^a & 0 & 0 \\ 0 & \eta^a & 0 \\ 0 & 0 & \eta^c \end{pmatrix}. \tag{5.27}$$

The interaction of the dislocation with these variants of the solute field is obtained by appropriately replacing $\eta_{\alpha\beta}^{(1)}$ with $\eta_{\alpha\beta}^{(2)}$ or $\eta_{\alpha\beta}^{(3)}$ in Eqn. (5.27).

5.3 Direct Calculations of Solute-Dislocation Interactions

Within the BCC structure there are three types of octahedral interstitials, indicated by the axis along which the primary axis of the octahedron lies. The respective Γ^o's are defined to be

$$\mathbf{\Gamma}^{o(1)} = \begin{pmatrix} \Gamma^o_{11} & 0 & 0 \\ 0 & \Gamma^o_{22} & 0 \\ 0 & 0 & \Gamma^o_{22} \end{pmatrix}, \quad \mathbf{\Gamma}^{o(2)} = \begin{pmatrix} \Gamma^o_{22} & 0 & 0 \\ 0 & \Gamma^o_{11} & 0 \\ 0 & 0 & \Gamma^o_{22} \end{pmatrix}$$

$$\mathbf{\Gamma}^{o(3)} = \begin{pmatrix} \Gamma^o_{22} & 0 & 0 \\ 0 & \Gamma^o_{22} & 0 \\ 0 & 0 & \Gamma^o_{11} \end{pmatrix}, \tag{5.28}$$

where the superscripts (i) indicate the dipole strength for an interstitial in the octahedral site with primary axis (*i.e.* the four-fold axis) along the ith direction.

As shown in previous section, the elastic dipole moment is related to the change in lattice parameters upon relaxing a periodic structure with one C atom per Fe supercell. For a carbon solute located along the x_1-axis of a simulation block defined by parameters L_1, L_2, and L_3, components of the elastic dipole moment are [Eq. (5.18)]

$$\Gamma^o_{11} = v_o \left(C_{11}\eta^c + 2C_{12}\eta^a \right), \quad \text{and} \quad \Gamma^o_{22} = v_o \left(C_{11}\eta^c + C_{12}(\eta^c + \eta^a) \right), \tag{5.29}$$

where v_o is the primitive cell volume, and C_{11} and C_{12} are two of the cubic elastic constants. The parameters η^c and η^a measure the relative changes in the supercell lattice parameters with respect to an addition of a carbon solute atom:

$$\eta^c = \frac{1}{L_o}\frac{dL_1}{dn}\bigg|_{n=0}, \quad \text{and} \quad \eta^a = \frac{1}{L_o}\frac{dL_2}{dn}\bigg|_{n=0}, \tag{5.30}$$

where η^c measures the expansion of the unit cell along the primary axis of the occupied octahedron, and η^a measures the contraction along the perpendicular axes. Here, n is the interstitial mole fraction of the carbon solute or the ratio between the number of carbon atoms to the host iron atoms. η^a and η^c are determined by considering the relaxation of supercells of varying compositions and plotting the observed lattice parameters as a function of n. These calculations are presented in Section 5.4.

In an alternate approach, the energy in Eq. (5.26) can be computed without the need to determine explicitly the η's. The solute-atom/dislocation interaction can be computed directly using periodic supercell calculations. Each supercell contains one solute atom, and the dislocation is assumed to strain the supercell homogeneously externally to the cell [2, 60, 61, 62]. The addition of the strain and stress fields of dislocation induces a variation in the strain energy. This variation defines the interaction energy between solute and dislocation.
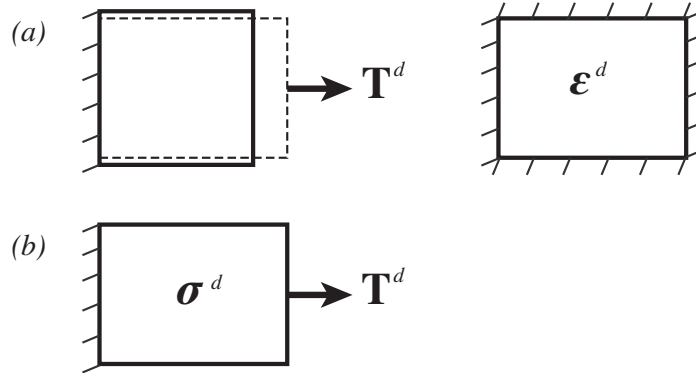
Figure 5.3: Schematic illustrations of two types of boundary conditions: (a)strain-controlled: changes in shape and volume of the body is produced by the the traction $\mathbf{T}^d$, and once the traction is removed the body is fixed by a constant strain $\boldsymbol{\varepsilon}^d$; (b)stress-controlled: a constant traction $\mathbf{T}^d$ is held constant while the boundary is not fixed.

The action of the dislocation on the solute is enforced using a fixed strain boundary condition. This choice is illustrated in in Fig. 5.3 along with a stress-controlled alternative. It is more convenient to perform atomic simulation using strain-controlled boundary conditions. In the case of strain-controlled boundary conditions, the boundary of the simulation supercell is fixed after applying a constant traction T_{ij}^d due to the dislocation stress field. The supercell (and its periodic images) is then held at a constant external dislocation strain field ε_{ij}^d (Fig. 5.3a). The supercell is brought in contact only with a thermal reservoir while remaining mechanically isolated. The governing thermodynamics potential is thus the Helmholtz free energy F.

To extract the interaction energy that, in the continuum limit, reduces to Eshelby's result in Eq. (5.1) and 5.16, the interaction is defined as the difference between the segregation energy of the solute in a strained versus an unstrained state $i.e.$,

$$F^{int} \;=\; \left[F(Fe:C,\boldsymbol{\varepsilon}^d) - F(Fe,\boldsymbol{\varepsilon}^d)\right] - \left[F(Fe:C) - F(Fe,ref)\right], \qquad (5.31)$$

where $F(Fe:C,\boldsymbol{\varepsilon}^d)$ is the energy of cells containing mostly Fe atoms and a single C atom with an imposed uniform dislocation strain $\boldsymbol{\varepsilon}^d$. $F(Fe,\boldsymbol{\varepsilon}^d)$ is the energy of cells containing only Fe under the strain $\boldsymbol{\varepsilon}^d$. $F(Fe:C)$ is the energy of the octahedral defect and $F(Fe,ref)$ is the energy of the reference perfect lattice.

Eq. (5.26) is the continuum linear elastic limit of Eq. (5.31). To see this, we define a new variable $\bar{\Delta}_{ij}^c = \partial_\beta \bar{u}_\alpha^c$ as the distortional field of the solute under the strain-controlled boundary conditions. The fixed strain boundary conditions imply that

$$\int_\Omega d^3\mathbf{r}\,\bar{\Delta}_{\alpha\beta}^c = 0, \qquad (5.32)$$

where the integral extends over the supercell volume, Ω.

The external dislocation field $\Delta^d_{\alpha\beta}$ simply adds to the solute fields $\bar{\Delta}^c_{\alpha\beta}$, and the relaxation energy from Eq. (5.31) becomes

$$
\begin{aligned}
\Delta F' &= F\left(Fe:C, \boldsymbol{\varepsilon}^d\right) - F\left(Fe, ref\right) \\
&= \int_\Omega d^3\mathbf{r} \left[\sigma^o_{\alpha\beta}\left(\bar{\Delta}^c_{\alpha\beta} + \Delta^d_{\alpha\beta}\right) + \frac{1}{2}c_{\alpha\beta\gamma\kappa}\left(\bar{\Delta}^c_{\alpha\beta} + \Delta^d_{\alpha\beta}\right)\left(\bar{\Delta}^c_{\kappa\gamma} + \Delta^d_{\kappa\gamma}\right)\right].
\end{aligned}
\tag{5.33}
$$

Applying Eq.(5.10) and (5.32), the relaxation energy can be written as

$$
\Delta F' = \int_\Omega d^3\mathbf{r} \left(\sigma^o_{\alpha\beta}\bar{\Delta}^c_{\alpha\beta} + \frac{1}{2}c_{\alpha\beta\kappa\gamma}\bar{\Delta}^c_{\alpha\beta}\bar{\Delta}^c_{\kappa\gamma}\right) + \frac{1}{2}\Omega c_{\alpha\beta\kappa\gamma}\Delta^d_{\alpha\beta}\Delta^d_{\kappa\gamma} - \Gamma^o_{\alpha\beta}\Delta^d_{\alpha\beta}.
\tag{5.34}
$$

Here, $\sigma^o_{\alpha\beta}$ is the strain-free stress required to maintain the reference structure upon an insertion of the carbon solute. The free energy of the system with constant external applied strain is

$$
\begin{aligned}
\Delta F^d &= F\left(Fe, \boldsymbol{\varepsilon}^d\right) - F\left(Fe, ref\right) \\
&= \frac{1}{2}\Omega c_{\alpha\beta\gamma\kappa}\Delta^d_{\gamma\kappa}\Delta^d_{\alpha\beta}.
\end{aligned}
\tag{5.35}
$$

The free energy of the solute in the absence of the dislocation traction field is

$$
\begin{aligned}
\Delta F^c &= F\left(Fe:C\right) - F(Fe, ref) \\
&= \int_\Omega d^3\mathbf{r} \left(\sigma^o_{\alpha\beta}\bar{\Delta}^c_{\alpha\beta} + \frac{1}{2}c_{\alpha\beta\kappa\gamma}\bar{\Delta}^c_{\alpha\beta}\bar{\Delta}^c_{\gamma\kappa}\right).
\end{aligned}
\tag{5.36}
$$

The interaction free energy approximated by linear elasticity theory is then given by

$$
F^{int} = \Delta F' - \Delta F^d - \Delta F^c = -\Gamma^o_{\alpha\beta}\Delta^d_{\alpha\beta},
\tag{5.37}
$$

which is in agreement with Eq. (5.26). Thus, within the strain-controlled boundary condition, the *ab initio* calculations are simple and also yields a continuum limit in agreement with Eshelby's result. Moreover, since the strain field can be chosen beyond those described by linear elasticity theory, Eq. (5.31) is a generic expression for the interaction of a defect with an arbitrary amplitude applied field (admittedly within a uniform strain approximation). Further, contributions of magnetism and higher order elastic moduli to interactions, commonly ignored in the elasticity theory, are intrinsically included in Eq. (5.31). Comparisons of the results derived from Eq. (5.31) with those derived from Eqn. (5.1) enable assessment of the influence of magnetic and electronic effects beyond those already reflected in the elastic constants. The elastic constants of Fe are certainly impacted by the fact that Fe is ferromagnetic. Hence the Γ^o_{ij}'s appearing in Eq. (5.1) already reflect, to a certain extent, the importance of magnetism. The implementation in Eq. (5.31), however, allows the magnetic and electronic structure to change with local changing strains, and thereby enables further assessment.

	PAW (this work)	EAM (this work)	PAW [64]	Exp. [65, 51]
$a_o(\text{A}^o)$	2.824	2.856	2.830	2.86
$C_{11}(\text{GPa})$	282	244	286	245
$C_{12}(\text{GPa})$	153	144	147	139
$C_{44}(\text{GPa})$	99	116	99	122
η^a	-0.053	-0.087		-0.094
η^c	0.867	0.550		0.847

Table 5.2: Bulk properties of pure iron and the relative lattice expansion and contraction due to a carbon atom located at an octahedral interstitial site

As a final step in the analysis, the solute atmosphere of a dislocation is determined using the computed energies and a simple statistical mechanics model. The predicted solute atmospheres around edge and screw dislocations along with experimental comparison are presented in Section 5.5.

5.4 Computer Results

In this section, first-principles electronic-structure-based total energy methods are applied to calculate the solute atom/dislocation interaction energy. These calculations make use of the approaches described above, and the predictions from both methods are compared. It is important to note that these electronic structure calculations do not include an explicit dislocation core. Consequently, total energy calculations based on empirical interatomic potentials are used to assess the range of validity for the methods.

Electronic-structure-based total energy calculations are performed using the Vienna *Ab initio* Simulation Package (VASP) [63]. The pseudopotentials describing the electron-ion interaction are generated by the projector augmented wave (PAW) method within the spin polarized generalized gradient approximation (GGA).

Elastic moduli and bulk structural properties are computed using a plane-wave expansion with an energy cutoff of 370 eV. A $17 \times 17 \times 17$ symmetrized Monkhorst-Pack grid is used for all integrations. This energy cutoff and grid sufficiently converge the total energy to better than 0.06 meV/atom. The values reported by Clatterbuck *et al.* [64], the present results, and experimental results [65, 51] are summarized in Table 5.2. The present results agree well with prior calculations.

Previous theoretical determinations of the solute-dislocation interaction energy have been done using the experimental values of the lattice parameter changes in Fe-C martensitic transformations [46, 47, 48]. The lattice parameters reported in these efforts were obtained from X-ray measurements of the mean tetragonal distortion of martensite. Clouet *et al.*[49],

on the other hand, computed the interaction energy using the lattice parameters from atomic simulation based on empirical potentials. Here, the relative lattice contraction and expansion, η^a and η^c, are computed by relaxing supercells containing host iron atoms and a carbon interstitial atom with respect to changes in volume and internal coordinates. The calculations are performed with supercells containing 16, 54, and 128 Fe atoms. To converge the total energy of the Fe-C alloy structures, the energy cutoff for all cells is set to 400 eV. (This cutoff is greater than the 370 eV used in determining the elastic constants mainly because of the carbon atom in the structure.) The k-point grids are adjusted so that the reciprocal volume per k-point for different sized supercells remains approximately unchanged. Specifically, the grid of $6 \times 6 \times 6$, $4 \times 4 \times 4$, and $3 \times 3 \times 3$ are used for the 16, 54, and 128 Fe atoms supercells, respectively. This number of k-point and energy cutoff sufficiently converge the total energy of the relaxed Fe-C alloy structure better than 0.06 meV/atom, and forces on the atoms are converged to less than 0.001 eV/Å. The concentration dependence of the lattice parameter predictions is shown also shown in Fig. 5.1. Note that the predicted equilibrium lattice parameter for Fe is less than that measured experimentally. The dependence of the lattice parameter on composition, however, tracks the experimental data compiled by Cheng *et al.* [51]. The resulting values of η_c and η_a are shown in Table 5.2. The computed values for η_c, η_a and the elastic moduli are then incorporated into Eq. (5.1) and (5.31) to compute the C solute atom/dislocation interaction.

In evaluating the atomistic interaction energy of a carbon solute with an edge dislocation of type $\langle 111 \rangle \{011\}$ based on Eq. (5.31), the local change in concentration $\Delta n^{(m)}$ is fixed by the size of the supercell. In the present study, the supercells of 54 iron atoms and one carbon interstitial are employed, hence the local composition is $n^{(m)} = 1/54$. Total energy calculations are performed using k-point $5 \times 5 \times 5$ Monkhorst-Pack k-point mesh and a 400 eV energy cutoff. For the Fe-C alloy structure in the strain-controlled boundary conditions, this k-point mesh and energy cutoff converge the total energy better than 0.06 meV/atom. The calculating cell volumes and lattice vectors are fixed by the anisotropic dislocation strain [66, 1]. Internal atomic positions are fully relaxed.

Figure 5.4 shows the angular dependence of the solute-dislocation interaction energies computed using Eq. (5.31) together with predictions from periodic elasticity theory, Eq. (5.1). The energies are evaluated at a radial distance of 12 Å from the dislocation core. A general trend of solute attraction (repulsion) below (above) the dislocation slip plane is observed. Both the tetragonality of the solute and the anisotropicity of the elastic fields give rise to the angular dependence of the amplitude of the interaction. Excellent agreement between atomistic and periodic elasticity theory predictions confirms (in part) the applicability of the periodic elasticity theory at distances of 12 Å from the core and greater.

A remaining issue is to evaluate the minimum extent to which first principle calculations and the periodic elasticity theory are valid in the core region. This is a non-trivial question. The dislocation core represents extremes in both stresses and stress gradients, as well as altered bonding topology. Since the periodic elasticity approach necessarily excludes stress gradients and altered bonding topologies, the theory is unlikely to be applicable at the core
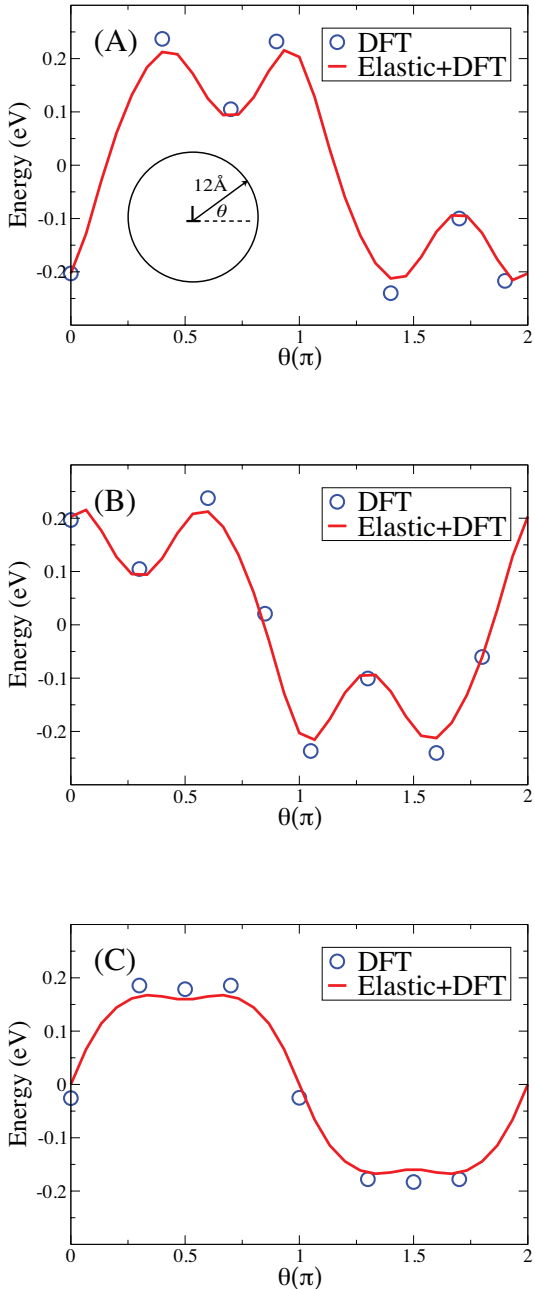
Figure 5.4: Continuum and DFT based interaction energy between a carbon solute and a $[111](1\bar{1}0)$ dislocation in Fe at 12 Å. The solute atom is located on x_1, x_2, and x_3-type sites in (A), (B), and (C) respectively.
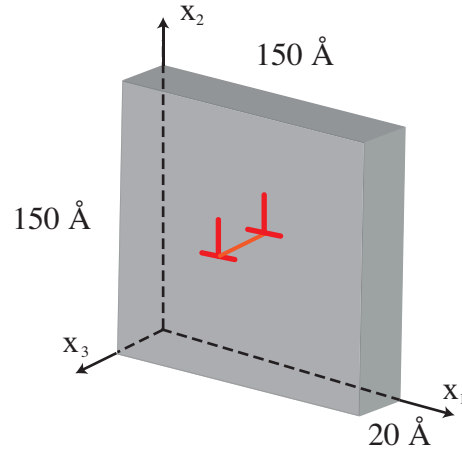
Figure 5.5: A simulation cell for EAM calculations. The size of the cell is $150 \times 150 \times 20$ Å, containing approximately 40,000 Fe atoms. The center of the cell contains an edge dislocation threading the bending axis.

itself. Further, numerical limitations only enable the study of relatively small supercells using electronic-structure-based total-energy methods. Consequently, it is difficult to study the interaction of a single solute atom with an extended dislocation using these methods. An alternate approach is to use empirical interatomic potential based methods to assess the extent of defect separations amenable to linear elasticity theory.

The extent of defect separations at which the elasticity is valid is examined by similar calculations employing embedded atom method (EAM) [67, 68] empirical potentials. Bulk properties obtained from this EAM empirical potential are summarized in Table 5.2. Similar studies of solute-dislocation interactions based on empirical potentials have been carried by several authors [69, 70, 71, 72, 49].

In computing an interaction energy using EAM empirical potentials, four independent calculations are necessary. The interaction energies extracted are similar to ones comprising Eqn. (5.31), where $F(Fe : C, \varepsilon^d)$ and $F(Fe, \varepsilon^d)$ are replaced by energies of nonuniform strained cells. The calculation cell is oriented such that its x_1-axis is parallel to [111] and the x_2-axis to [1$\bar{1}$0]. Periodic boundary conditions are applied along the dislocation line, and the dislocation is placed on the neutral bending axis. Stationary boundary conditions are imposed in the x_1 and x_2-direction. Image effects are minimized by employing large calculation cells containing approximately 40,000 atoms with a dimension of $150 \times 150 \times 20$ Å, as illustrated in Figure 5.5.

Figure 5.6 shows interactions between a $\langle 111 \rangle \{110\}$ edge dislocation and a carbon solute atom computed from atomic simulations using the Fe-C empirical potential developed by Becquart *et al.* [73]. The energies are plotted at constant θ while varying the distance from the dislocation core. The angle θ is measured from the $\langle 111 \rangle$ axis. Solid lines are
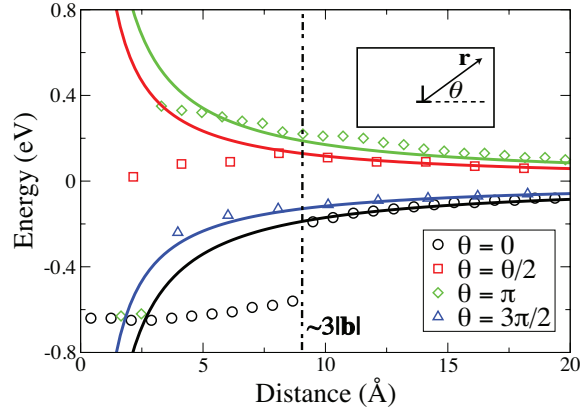
Figure 5.6: Interaction energies between a carbon solute atom and a $\langle 111 \rangle \{110\}$ edge dislocation in Fe computed from atomic simulation based on empirical potentials. The energies are measured as a function of distance from the dislocation core as depicted in the inset.

the interaction energies predicted from periodic elasticity theory. Excepting the case $\theta = 0$, the energy interactions show continuous deviations from the elasticity theory at about three burger vectors from the dislocation core. In the case $\theta = 0$, the discontinuous variation of the energy is caused by the dislocation core shifting toward the solute. The high strain region around the solute in this case enables total energy reduction by inducing motion of dislocation. However, no similar results are observed at the other angles. The minimum defect separation to both the homogeneous strain approximation and the periodic elasticity theory is approximately $3b$.

Since stress and strain field gradients are incorporated to the explicit solute-dislocation atomistic simulation, comparison between interactions computed from atomic simulations and the periodic elasticity theory enable an assessment of the importance of these gradients. As is shown in Figure 5.7, the agreement between elasticity theory and the direct atomistic results is excellent beyond $3b$. The agreement demonstrates the unimportance of strain gradients to solute-atom/dislocation interactions, at least in the far-field as represented by EAM.

5.5 Solute Atmosphere

Solutes and dislocation mapping within atom probe tomography provides, perhaps, the most direct information regarding solute-atom/dislocation interactions [9]. First principles calculations aid tomographic experiments by providing theoretical prediction of solute atmospheres.
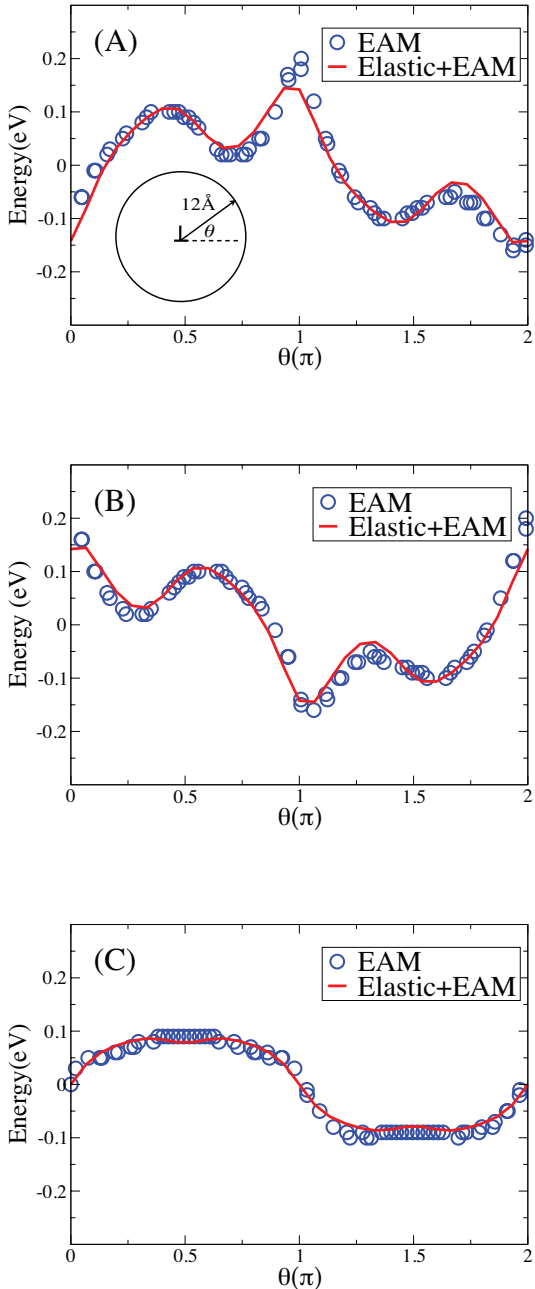
Figure 5.7: Continuum and EAM based interaction energy between a carbon solute and a $[111](1\bar{1}0)$ dislocation in Fe at 12 Å. The solute atom is located on the x_1, x_2, and x_3-type sites in (A), (B), and (C) respectively.

As found by experiments [9], much of the solute atmosphere is distributed far from the dislocation core. In this far-field, the assumptions entering the periodic elasticity theory developed above should be acceptable.

Theoretical studies of solute-atom distributions is rooted in a statistical mechanics model already pursued by several authors [74, 75]. Since the occupancy state of the interstitial site by a solute atom is either zero or unity, Fermi-Dirac statistics are proper for quantifying solute concentrations. Assuming solutes are non-interacting particles, the thermal average value of the occupancy of the interstitial sites is given by

$$n^{(m)}(\mathbf{r}) = \frac{\exp\left[-\frac{\mu+F_{int}^{(m)}(\mathbf{r})}{kT}\right]}{1 + \exp\left[-\frac{\mu+F_{int}^{(m)}(\mathbf{r})}{kT}\right]}, \tag{5.38}$$

where μ is the chemical potential of the solute. Away from the dislocation where the interaction energy is negligible, the occupancy of the interstitial sites is

$$n_o^{(m)} = \frac{\exp\left[-\frac{\mu}{kT}\right]}{1 + \exp\left[-\frac{\mu}{kT}\right]}. \tag{5.39}$$

By eliminating μ in Eq. (5.38) and (5.39), the fraction of occupied interstices is given by

$$\frac{n^{(m)}(\mathbf{r})}{1 - n^{(m)}(\mathbf{r})} = \frac{n_o^{(m)}}{1 - n_o^{(m)}} \exp\left[-\frac{F_{int}^{(m)}(\mathbf{r})}{kT}\right], \tag{5.40}$$

where the elastic interaction energy term is computed from Eqn.(5.1).

The net accumulation of solute is

$$\Delta n = \left(n^{(1)} + n^{(2)} + n^{(3)}\right) - n_o \tag{5.41}$$

where in this work the background concentration n_o is assumed to be Fe-0.11 wt%C or 0.5 at%C as in the experiment in [9].

The first principles predictions of solute atmospheres Δn are shown in Figure 5.8 and 5.9. The edge dislocation in Figure 5.8 is of type $\frac{1}{2}[111](1\bar{1}0)$. There is a net accumulation of solute in the tensile region under the dislocation. The size of the solute cluster also depends on the temperature. A denser cluster of solutes is observed at the temperature 300 K. Figure 5.9 shows a net concentration profile around a $\frac{1}{2}[111](11\bar{2})$ screw dislocation at room temperature. Since screw dislocations exert shear forces in the crystal, the change in solute concentration around them is less than that around edge dislocations. A 3-fold symmetry of solute distribution around the screw dislocation arises from a 3-fold crystal symmetry along [111] direction of a cubic crystal and the tetragonality of the solutes.

To a good approximation, carbon atoms are bound to the dislocation only when their interaction energy is larger than $k_B T$. Thermal fluctuation may take away carbon atoms
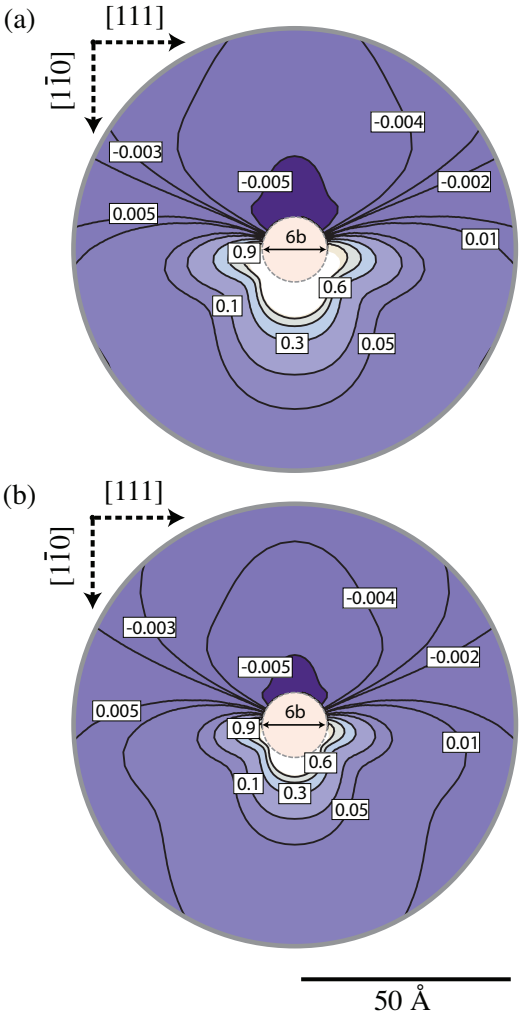
Figure 5.8: Solute distributions around a [111] (1$\bar{1}$0) edge dislocation at temperature (a) 300 K and (b) 400 K.
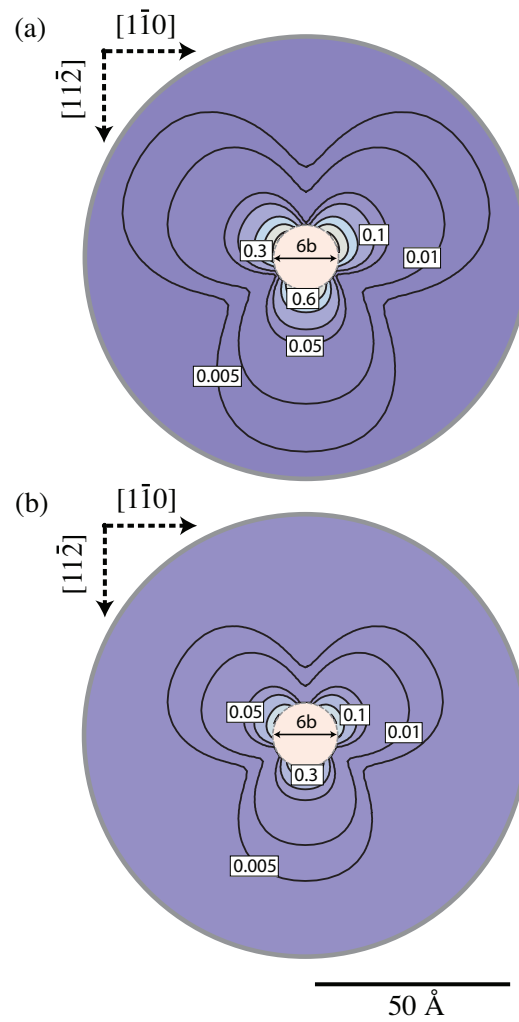
Figure 5.9: Solute distributions around a $[111]\,(11\bar{2})$ screw dislocation at temperature (a) 300 K and (b) 400 K.

References	Dislocation Type	Extent (nm)	Enrichment Factor
This work	Screw	12	4.4
This work	Edge	20	5.3
[9]	Unknown	10	7.7

Table 5.3: Extent and enrichment of solute atoms around dislocations. The diameter $6b$ around the dislocation core is excluded in the prediction.

at the distance when the interaction is small compared to the thermal energy. Setting the interaction energy equal to $k_B T$ defines a region over which solute concentration may be enhanced, and enables the definition of an enrichment factor. Table 5.3 reports this size for both edge and screw dislocations at 300 K. Quantitatively, the theoretical solute atmosphere spreads about 100-200 Å from the dislocation core in agreement reported values ($\sim$100Å) from atom probe experiments [9].

In the atom probe literature, the ratio of the number of the solute atoms to those of the background atoms is known as the enrichment factor. The predicted and experimental enrichment factors for 300 K are shown in Table 5.3. The theoretical value of the enrichment is most likely underestimated because the core region $6b$ in diameter is excluded in the calculation. If the solute segregation energies predicted by the theory are used to predict the carbon concentration within the core region, the predicted enrichment factors for both screw and edge dislocation rise to approximately 6.7. The resulting predictions of the theory are in reasonable agreement with experimental observations.

In summary, from an intermediate scale between the atomistic and contiuum limits, a periodic model for first principles calculations is developed to study the carbon solute atmosphere near dislocations in iron. The first principles calculations predict the solute-dislocation interactions accurately at the distance greater than about three times the Burgers vector from the dislocations. Our predicted solute atmospheres are in good agreement with the experiments when comparing the extent and enrichment of the solutes.

Appendix A

Symmetry of The Dynamical Matrix for BCC crystals

The pseudo Ti-V Gum Metal structure is body-centered-cubic. The nearest neightbors are located at

$$\mathbf{d}^{(1),(2)} = \pm\frac{a}{2}(1,1,1), \quad \mathbf{d}^{(3),(4)} = \pm\frac{a}{2}(-1,1,1), \quad \text{and}$$
$$\mathbf{d}^{(5),(6)} = \pm\frac{a}{2}(1,-1,1), \quad \mathbf{d}^{(7),(8)} = \pm\frac{a}{2}(-1,-1,1) \tag{A.1}$$

Suppose

$$\mathcal{K}(\mathbf{d}^{(1)}) = -\begin{pmatrix} \mathcal{A}_1 & \mathcal{B}_1 & \mathcal{C}_1 \\ \mathcal{B}_1 & \mathcal{D}_1 & \mathcal{E}_1 \\ \mathcal{C}_1 & \mathcal{E}_1 & \mathcal{F}_1 \end{pmatrix}, \tag{A.2}$$

where the elements in the matrix are some numbers. Applying a 3-fold rotation about the [111]-axis to $\mathbf{d}^{(1)}$ leaves $\hat{\mathcal{O}}_{2\pi/3}\mathbf{d}^{(1)} = \mathbf{d}^{(1)}$. The matrix representation of the rotation about the [111]-axis is

$$\hat{\mathcal{O}}_{2\pi/3} = \begin{pmatrix} 0 & 1 & 0 \\ 0 & 0 & 1 \\ 1 & 0 & 0 \end{pmatrix}. \tag{A.3}$$

It follows from Eq.(2.23) that $\mathcal{K}(\hat{\mathcal{O}}\mathbf{d}^{(1)}) = \mathcal{K}(\mathbf{d}^{(1)}) = \hat{\mathcal{O}}_{2\pi/3}\mathcal{K}(\mathbf{d}^{(1)})\hat{\mathcal{O}}_{2\pi/3}^T$, we have $\mathcal{A}_1 = \mathcal{D}_1 = \mathcal{F}_1$ and $\mathcal{C}_1 = \mathcal{B}_1 = \mathcal{E}_1$, i.e.

$$\mathcal{K}(\mathbf{d}^{(1)}) = -\begin{pmatrix} \mathcal{A}_1 & \mathcal{C}_1 & \mathcal{C}_1 \\ \mathcal{C}_1 & \mathcal{A}_1 & \mathcal{C}_1 \\ \mathcal{C}_1 & \mathcal{C}_1 & \mathcal{A}_1 \end{pmatrix} \tag{A.4}$$

Likewise, by the inversion symmetry

$$\hat{\mathcal{O}}_{-1} = \begin{pmatrix} -1 & 0 & 0 \\ 0 & -1 & 0 \\ 0 & 0 & -1 \end{pmatrix}, \tag{A.5}$$

we obtain $\hat{\mathcal{O}}_{-1}\mathbf{d}^{(1)} = -\mathbf{d}^{(1)} = \mathbf{d}^{(2)}$, hence $\mathcal{K}(\mathbf{d}^{(2)}) = \hat{\mathcal{O}}_{-1}\mathcal{K}(\mathbf{d}^{(1)})\hat{\mathcal{O}}_{-1}^T$ which yields

$$\mathcal{K}(\mathbf{d}^{(1)}) = \mathcal{K}(\mathbf{d}^{(2)}) \tag{A.6}$$

and similarly $\mathcal{K}(\mathbf{d}^{(3)}) = \mathcal{K}(\mathbf{d}^{(4)})$, $\mathcal{K}(\mathbf{d}^{(5)}) = \mathcal{K}(\mathbf{d}^{(6)})$, and $\mathcal{K}(\mathbf{d}^{(7)}) = \mathcal{K}(\mathbf{d}^{(8)})$. The vectors $\mathbf{d}^{(1)}$ and $\mathbf{d}^{(5)}$ are related by a 2-fold rotation about the z-axis, $\mathbf{d}^{(5)} = \hat{\mathcal{O}}_{2\pi/4}\mathbf{d}^{(1)}$, where rotation matrix $\hat{\mathcal{O}}_{2\pi/4}$ is

$$\hat{\mathcal{O}}_{2\pi/4} = \begin{pmatrix} 0 & 1 & 0 \\ -1 & 0 & 0 \\ 0 & 0 & 1 \end{pmatrix} \tag{A.7}$$

It follows that $\mathcal{K}(\hat{\mathcal{O}}_{2\pi/4}\mathbf{d}^{(1)}) = \mathcal{K}(\mathbf{d}^{(5)}) = \hat{\mathcal{O}}_{2\pi/4}\mathcal{K}(\mathbf{d}^{(1)})\hat{\mathcal{O}}_{2\pi/4}^T$, i.e.

$$\mathcal{K}(\mathbf{d}^{(5)}) = -\begin{pmatrix} \mathcal{A}_1 & -\mathcal{C}_1 & \mathcal{C}_1 \\ -\mathcal{C}_1 & \mathcal{A}_1 & -\mathcal{C}_1 \\ \mathcal{C}_1 & -\mathcal{C}_1 & \mathcal{A}_1 \end{pmatrix} \tag{A.8}$$

By appplying the analogous procedure to $\mathcal{K}(\mathbf{d}^{(3)})$, and $\mathcal{K}(\mathbf{d}^{(7)})$, similar reduced force constant matrics can be determined. The same procedure can be extended to the further neighboring atoms. For a bcc structure, the next nearest neightbors are located at

$$a(1,0,0),\ a(0,1,0),\ a(0,0,1),\ldots \tag{A.9}$$

and so on. The example of the fcc structure can be found in the manuscript by Brüesch [20].

Appendix B

Scattering in Solids

In this appendix, we review theory of scattering leading to the theoretical diffraction pattern in Fig.(2.6). We begin with an elementary theory of diffraction, which can be found in standard solid state physics textbooks [76, 23]. Then the scattering off vibrational modes in solid is then discussed. The excellent review of the later part can be found in [18].

B.1 Scattering of Ideal Solids

For a scattering potential $V(\mathbf{r})$, the differential cross-section $\mathrm{d}^2\sigma/\mathrm{d}\Omega$ per unit solid angle of the outgoing wave with the wave state $|\mathbf{k}'\rangle$ is

$$\frac{\mathrm{d}^2\sigma}{\mathrm{d}\Omega} \sim \frac{2\pi}{\hbar} \left| \langle \mathbf{k}|V(\mathbf{r})|\mathbf{k}'\rangle \right|^2. \tag{B.1}$$

For a crystal the potential has the periodicity of the lattice, i.e.

$$V(\mathbf{r}) = \sum_{m,n,o} V_a(\mathbf{r} - \mathbf{R}_{mmo}) = \sum_{\mathbf{R}} V(\mathbf{r} - \mathbf{R}), \quad \text{for some integers } m, n \text{ and } o, \tag{B.2}$$

where the lattice vectors are

$$\mathbf{R} = \mathbf{R}_{mno} = m\mathbf{a}_1 + n\mathbf{a}_2 + o\mathbf{a}_3. \tag{B.3}$$

For a scattering of an ideal crystal where the fluctuations are neglected,

$$
\begin{aligned}
\langle \mathbf{k}|V|\mathbf{k}'\rangle &= \int \mathrm{d}^3\mathbf{r}\, e^{-i\mathbf{k}'\cdot\mathbf{r}} \sum_{\mathbf{R}} V_a(\mathbf{r} - \mathbf{R}) e^{i\mathbf{k}\cdot\mathbf{r}} \\
&= \sum_{\mathbf{R}} \int \mathrm{d}^3\mathbf{r}\, e^{i(\mathbf{k}-\mathbf{k}')\cdot\mathbf{r}} V_a(\mathbf{r} - \mathbf{R}) \\
&= \sum_{\mathbf{R}} e^{i(\mathbf{k}-\mathbf{k}')\cdot\mathbf{R}} \int \mathrm{d}^3\mathbf{r}\, e^{i(\mathbf{k}-\mathbf{k}')\cdot(\mathbf{r}-\mathbf{R})} V_a(\mathbf{r} - \mathbf{R}).
\end{aligned}
\tag{B.4}
$$

The range of the integral is over the whole crystal. Introducing the *scattering* wave vector $\mathbf{q}$ as

$$\mathbf{q} = \mathbf{k}' - \mathbf{k}, \tag{B.5}$$

and change variable $\mathbf{r}' \mapsto \mathbf{r} - \mathbf{R}$, the Fourier amplitude of the atomic potential is

$$V_a(\mathbf{q}) = \frac{1}{v_a} \int \mathrm{d}^3\mathbf{r}' V_a(\mathbf{r}') e^{-i\mathbf{q}\cdot\mathbf{r}'}, \tag{B.6}$$

where v_a is the atomic volume, $v_a = V/N$ [1]. The matrix element entering the scattering cross-section becomes

$$\langle \mathbf{k}|V|\mathbf{k}'\rangle = V_a(\mathbf{q}) \sum_{\mathbf{R}} e^{-i\mathbf{q}\cdot\mathbf{R}}. \tag{B.7}$$

The differential cross-section is

$$\frac{\mathrm{d}^2\sigma}{\mathrm{d}\Omega} \propto v_a^2 |V_a(\mathbf{q})|^2 \left| \sum_{\mathbf{R}} e^{i\mathbf{q}\cdot\mathbf{R}} \right|^2. \tag{B.8}$$

that is the contributions are separated into two parts due to (1) the potential of an individual scatterer, and (2) the lattice structure. Consider a solid consisting of N lattice points and has a parallelpiped shape. There are L_1, L_2, and L_3 lattice points along the $x-$, $y-$ and $z-$axes respectively. The wavevector $\mathbf{q}$'s can be written as

$$\begin{aligned}
\mathbf{q} &= q_1\mathbf{b}_1 + q_2\mathbf{b}_2 + q_3\mathbf{b}_3 \quad \text{and} \\
\mathbf{R} &= m\mathbf{a}_1 + n\mathbf{a}_2 + o\mathbf{a}_3,
\end{aligned} \tag{B.9}$$

where $\mathbf{b}_i \cdot \mathbf{a}_j = 2\pi\delta_{ij}$. The argument of the structure term in Eq.(B.8) becomes

$$\begin{aligned}
\sum_{\mathbf{R}} e^{-i\mathbf{q}\cdot\mathbf{R}} &= \sum_{u,v,w} e^{-2\pi i(q_1 u + q_2 v + q_3 w)} \\
&= \left(\sum_{m=-L_1/2}^{(L_1-1)/2} e^{-2\pi i q_1 u} \right) \left(\sum_{n=-L_2/2}^{(L_2-1)/2} e^{-2\pi i q_2 v} \right) \left(\sum_{o=-L_3/2}^{(L_3-1)/2} e^{-2\pi i q_3 w} \right) \\
&= \frac{\sin(\pi L_1 q_1)}{\sin(\pi q_1)} \cdot \frac{\sin(\pi L_2 q_2)}{\sin(\pi q_2)} \cdot \frac{\sin(\pi L_3 q_3)}{\sin(\pi q_2)}.
\end{aligned} \tag{B.10}$$

Each term falls off rapidly for some large integers L_i, and highly peaks when q_i is an integer or $\mathbf{q}$ is a reciprocal vector $\mathbf{G}$. When $\mathbf{q} = \mathbf{G}$, both the numerator and denominator returns zero, hence by returning to the original sum $\exp(-i\mathbf{G}\cdot\mathbf{R}) = 1$

$$\sum_{\mathbf{R}} e^{-i\mathbf{G}\cdot\mathbf{R}} = \sum_{\mathbf{R}} (1) = N. \tag{B.11}$$

---

[1]The inverse Fourier transform is defined in this particular way so that $V_a(\mathbf{q})$ has the same unit as $V_a(\mathbf{r})$.

That is

$$\sum_{\mathbf{R}} e^{-i\mathbf{q}\cdot\mathbf{R}} = N \sum_{\mathbf{G}} \delta_{\mathbf{q},\mathbf{G}}, \tag{B.12}$$

The differential cross-section is thus

$$\frac{d\sigma}{d\Omega} \propto |V_a(\mathbf{q})|^2 \left|\sum_{\mathbf{R}} e^{i\mathbf{q}\cdot\mathbf{R}}\right|^2 = |V_a(\mathbf{q})|^2 N^2 \sum_{\mathbf{G}} \delta_{\mathbf{q},\mathbf{G}}. \tag{B.13}$$

which vanishes for every $\mathbf{q}$, except $\mathbf{q} = \mathbf{k} - \mathbf{k}' = \mathbf{G}$. This last expression holds two important information: (1) the brightness of the diffraction spot is in the order of N^2, and (2) no diffraction peaks are observed unless $\mathbf{q} = \mathbf{G}$. The disappearance of the diffraction spots by the term $|\sum_{\mathbf{R}} \exp(i\mathbf{q}\cdot\mathbf{r})|^2$ is purely due to the structure of the solid, hence it is named the *structure factor*.

B.2   Scattering of Vibrations in a Solid

The scattering of vibrational modes in a solid can be thought of as an extension of the scattering from an ideal solid. Due to the atomic vibrations, the intensities measured experimentally is no longer dictated by the structure factor, but its average, i.e.

$$I(\mathbf{q}) \propto \left\langle \left\|\sum_{\mathbf{R}} e^{i\mathbf{q}\cdot\mathbf{r}}\right\|^2 \right\rangle \tag{B.14}$$

where $\langle\ldots\rangle$ indicates the thermal average over a statistical distribution. Specifically for vibrations in solids, the distribution is of *Bose-Einstein*.

The positional vectors to the atoms are

$$\mathbf{r}(l,m,n) = \mathbf{R} + \mathbf{u}(l,m,n) = \mathbf{R} + \mathbf{u}(\mathbf{R}), \tag{B.15}$$

where $\mathbf{u}$'s are the displacement vectors measured from the mean $\mathbf{R}$'s. By separating out the lattice term,

$$I(\mathbf{q}) = \sum_{\mathbf{R},\mathbf{R}'} e^{i\mathbf{q}\cdot(\mathbf{R}-\mathbf{R}')} \left\langle e^{\mathbf{q}\cdot[\mathbf{u}(\mathbf{R})-\mathbf{u}(\mathbf{R}')]} \right\rangle. \tag{B.16}$$

Using the identity[2]

$$\begin{aligned}
\left\langle e^{ip} \right\rangle &= 1 + i\langle p \rangle - \frac{1}{2!}\left\langle p^2 \right\rangle - \frac{i}{3!}\left\langle p^3 \right\rangle + \frac{1}{4}\left\langle p^4 \right\rangle - \ldots \\
&= 1 - \frac{1}{2}\left\langle p^2 \right\rangle + \frac{1}{4!}\left\langle p^4 \right\rangle - \ldots \\
\left\langle e^{ip} \right\rangle &= e^{-\frac{1}{2}\langle p^2 \rangle},
\end{aligned} \tag{B.17}$$

---

[2]The proof of this identity from the Bose-Einstein distribution can be found in [18].

for small p, the exponent term in Eq.(B.16) becomes

$$\sum_{\alpha,\beta} q_\alpha q_\beta \left(u_\alpha(\mathbf{R}) - u_\alpha(\mathbf{R}')\right) \left(u_\beta(\mathbf{R}) - u_\beta(\mathbf{R}')\right) =$$
$$\sum_{\alpha,\beta} [q_\alpha q_\beta u_\alpha(\mathbf{R}) u_\beta(\mathbf{R}') + q_\alpha q_\beta u_\alpha(\mathbf{R}') u_\beta(\mathbf{R}') \quad\quad\text{(B.18)}$$
$$-q_\alpha q_\beta u_\alpha(\mathbf{R}) u_\beta(\mathbf{R}') - q_\alpha q_\beta u_\alpha \mathbf{R}') u_\beta(\mathbf{R})]\,,$$

or

$$\left\langle \left([\mathbf{q} \cdot (\mathbf{u}(\mathbf{R}) - \mathbf{u}(\mathbf{R}'))]^2 \right) \right\rangle = 2 \sum_{\alpha,\beta} q_\alpha q_\beta \left\langle u_\alpha(\mathbf{R}) u_\beta(\mathbf{R}) \right\rangle$$
$$- 2 \sum_{\alpha,\beta} q_\alpha q_\beta \left\langle u_\alpha(\mathbf{R}) u_\beta(\mathbf{R}') \right\rangle . \quad\quad\text{(B.19)}$$

From the quantum theory of vibrations in a solid, the displacement fluctiuation is given by [18],

$$u_\alpha(\mathbf{R}) = \frac{1}{\sqrt{Nm}} \sum_{\mathbf{k},r} Q_r(\mathbf{k}) a_\alpha^{(r)}(\mathbf{k}) e^{i\mathbf{k}\cdot\mathbf{R}}$$
$$= \sqrt{\frac{\hbar}{2Nm}} \sum_{\mathbf{k},r} \frac{a_\alpha^{(r)}}{\sqrt{\omega^{(r)}(\mathbf{k})}} e^{i\mathbf{k}\cdot\mathbf{R}} \left(\hat{a}_{-\mathbf{k}r}^\dagger + \hat{a}_{\mathbf{k},r} \right) , \quad\quad\text{(B.20)}$$

where $\hat{a}_{\mathbf{k},r}^\dagger$ and $\hat{a}_{\mathbf{k},r}$ are the creation and annihilation operators of the $\mathbf{k}$ mode phonon with the $r-$th polarization.

The *correlation function* of the displacement in Eq.(B.19) becomes

$$\langle u_\alpha(\mathbf{R}) u_\beta(\mathbf{R}') \rangle =$$
$$\frac{\hbar}{2Nm} \sum_{\substack{\mathbf{k},\mathbf{k}' \\ r,r'}} \frac{a_\alpha^{(r)}}{\sqrt{\omega^{(r)}(\mathbf{k})}} \frac{a_\beta^{()r;}}{\sqrt{\omega^{(r')}(\mathbf{k}')}} \quad\quad\text{(B.21)}$$
$$e^{i\mathbf{k}\cdot\mathbf{R}} e^{i\mathbf{k}'\cdot\mathbf{R}'} \left\langle (\hat{a}_{-\mathbf{k}r}^\dagger + \hat{a}_{\mathbf{k}r})(\hat{a}_{-\mathbf{k}'rr}^\dagger + \hat{a}_{\mathbf{k}'r'}) \right\rangle .$$

The average of the creation and annihilation terms can be simplified using as

$$
\begin{aligned}
\langle(\hat{a}^{\dagger}_{-\mathbf{k}r} + \hat{a}_{\mathbf{k}r})(\hat{a}^{\dagger}_{-\mathbf{k}'r'} + \hat{a}_{\mathbf{k}'r'})\rangle \\
= \left\langle \hat{a}^{\dagger}_{-\mathbf{k}r}\hat{a}^{\dagger}_{-\mathbf{k}'r'} + \hat{a}^{\dagger}_{-\mathbf{k}r}\hat{a}_{-\mathbf{k}'r'} + \hat{a}_{\mathbf{k}r}\hat{a}^{\dagger}_{-\mathbf{k}'r'} + \hat{a}_{\mathbf{k}r}\hat{a}_{\mathbf{k}'r'} \right\rangle \\
= \left\langle \hat{a}^{\dagger}_{-\mathbf{k}r}\hat{a}_{\mathbf{k}'r'} \right\rangle + \left\langle \hat{a}_{\mathbf{k}r}\hat{a}^{\dagger}_{-\mathbf{k}'r'} \right\rangle \\
= \delta_{\mathbf{k},-\mathbf{k}'}\delta_{rr'}\langle n_r(\mathbf{k})\rangle + \delta_{\mathbf{k},-\mathbf{k}'}\delta_{rr'}(1 + \langle n_r(\mathbf{k})\rangle) \\
= \delta_{rr'}\delta_{\mathbf{k},-\mathbf{k}'}\left(2\langle n_r(\mathbf{k})\rangle + 1\right) \\
= 2\delta_{\mathbf{k},-\mathbf{k}'}\delta_{rr'}\left(\langle n_r(\mathbf{k})\rangle + \frac{1}{2}\right) \\
= 2\delta_{\mathbf{k},-\mathbf{k}'}\delta_{rr'}\frac{E_r(\mathbf{k})}{\hbar\omega^{(r)}(\mathbf{k})}.
\end{aligned}
\tag{B.22}
$$

So that the correlation function of displacement is

$$
\begin{aligned}
\langle u_\alpha(\mathbf{R})u_\beta(\mathbf{R}')\rangle = &\frac{1}{Nm}\sum_{\substack{\mathbf{k},\mathbf{k}' \\ r,r'}} \frac{a_\alpha^{(r)}}{\sqrt{\omega^{(r)}(\mathbf{k})}}\frac{a_\beta^{(r')}}{\sqrt{\omega^{(r')}(\mathbf{k}')}} \\
&\delta_{\mathbf{k},-\mathbf{k}'}\delta_{rr'}\frac{E_r(\mathbf{k})}{\omega^{(r)}(\mathbf{k})}e^{i\mathbf{k}\cdot\mathbf{R}}e^{i\mathbf{k}'\cdot\mathbf{R}'} \\
= &\frac{1}{Nm}\sum_{\mathbf{k},r} a_\alpha^{(r)}(\mathbf{k})a_\beta^{(r)}(\mathbf{k})\frac{E_r(\mathbf{k})}{\omega^{2(r)}(\mathbf{k})}e^{i\mathbf{k}\cdot(\mathbf{R}-\mathbf{R}')}.
\end{aligned}
\tag{B.23}
$$

Inserting Eq.(B.23) into Eq.(B.19), one has

$$
\begin{aligned}
\sum_{\alpha\beta} q_\alpha q_\beta \langle u_\alpha(\mathbf{R})u_\beta(\mathbf{R}')\rangle = &\frac{1}{Nm}\sum_{\mathbf{k},r}\sum_{\alpha\beta} q_\alpha q_\beta a_\alpha^{(r)}(\mathbf{k})a_\beta^{(r)}(\mathbf{k}) \\
&\frac{E_r(\mathbf{k})}{\omega^{2(r)}(\mathbf{k})}e^{i\mathbf{k}\cdot(\mathbf{R}-\mathbf{R}')}.
\end{aligned}
\tag{B.24}
$$

That is,

$$
\sum_{\alpha\beta} q_\alpha q_\beta \langle u_\alpha(\mathbf{R})u_\beta(\mathbf{R}')\rangle = \frac{1}{Nm}\sum_{\mathbf{k},r}\left|\mathbf{q}\cdot\mathbf{a}^{(r)}(\mathbf{k})\right|^2 \frac{\langle E_r(\mathbf{k})\rangle}{\omega^{2(r)}(\mathbf{k})}e^{i\mathbf{k}\cdot(\mathbf{R}-\mathbf{R}')}.
\tag{B.25}
$$

Note that for convenient usages, correlation function may be written in terms of the Fourier summation as

$$
\langle u_\alpha(\mathbf{R})u_\beta(\mathbf{R}')\rangle = \sum_{\mathbf{k}} \mathcal{C}_{\alpha\beta}(\mathbf{k})e^{i\mathbf{k}\cdot(\mathbf{R}-\mathbf{R}')},
\tag{B.26}
$$

where the Fourier amplitudes $\mathcal{C}_{\alpha\beta}(\mathbf{k})$'s are

$$
\mathcal{C}_{\alpha\beta}(\mathbf{k}) = \frac{1}{Nm}\sum_{r} a_\alpha^{(r)}(\mathbf{k})a_\beta^{(r)}(\mathbf{k})\frac{\langle E_r(\mathbf{k})\rangle}{\omega^{2(r)}(\mathbf{k})}.
\tag{B.27}
$$

Next, consider the first term in Eq.(B.19). It is the *Debye-Waller* factor, informing about the spread of the Bragg's peaks due to the on-site correlation. This property will become clear in a moment. The Debye-Waller factor $W(\mathbf{q})$ is defined as

$$
2W(\mathbf{q}) = \sum_{\alpha\beta} q_\alpha q_\beta \langle u_\alpha(\mathbf{R}) u_\beta(\mathbf{R}) \rangle = \sum_{\alpha\beta} q_\alpha q_\beta \langle u_\alpha(0) u_\beta(0) \rangle
$$

$$
= \frac{1}{Nm} \sum_{\mathbf{k},r} \left| \mathbf{q} \cdot \mathbf{a}^{(r)}(\mathbf{k}) \right|^2 \frac{\langle E_r(\mathbf{k}) \rangle}{\omega^{2(r)}(\mathbf{k})}.
$$

(B.28)

The diffraction intensity due to vibrational modes is given by

$$
I(\mathbf{q}) = e^{-2W(\mathbf{q})} \sum_{\mathbf{R},\mathbf{R}'} e^{i\mathbf{q}\cdot(\mathbf{R}-\mathbf{R}')} \exp\left(\sum_{\mathbf{k},r} \mathcal{G}_r(\mathbf{k}) e^{i\mathbf{k}\cdot(\mathbf{R}-\mathbf{R}')} \right),
$$

(B.29)

where

$$
\mathcal{G}_r(\mathbf{k}) \equiv \frac{1}{Nm} \left| \mathbf{q} \cdot a^{(r)}(\mathbf{k}) \right|^2 \frac{\langle E_r(\mathbf{k}) \rangle}{\omega^{2(r)}(\mathbf{k})}.
$$

(B.30)

Note that $\mathcal{G}_r(\mathbf{k})$ defined this way is just for convenient use. By shifting the order of the summation such that $(\mathbf{R} - \mathbf{R}') \mapsto \mathbf{R}$, the intensity is

$$
I(\mathbf{q}) = N e^{-2W(\mathbf{q})} \sum_{\mathbf{R}} e^{i\mathbf{q}\cdot\mathbf{R}} \exp\left(\sum_{\mathbf{k},r} \mathcal{G}_r(\mathbf{k}) e^{i\mathbf{k}\cdot\mathbf{R}} \right).
$$

(B.31)

Eq.(B.31) is the fundamental equation of diffraction off a solid. It accounts for both the mean positions of the atoms and their displacements due to vibrations. From the expression above, it is clear that the Debye-Waller factor indeed causes the spreading of the Bragg's diffraction. Direct evaluation of Eq.(B.31) is however not a trivial task since it involves the exponents of a summation. However, since $\mathcal{G}_r(\mathbf{k})$ relates to the correlation function which is small for a large separation of atoms, we can introduce a Taylor series expansion as

$$
\exp\left(\sum_{\mathbf{k},r} \mathcal{G}_r(\mathbf{k}) e^{i\mathbf{k}\cdot\mathbf{R}} \right) = 1 + \sum_{\mathbf{k},r} \mathcal{G}_r(\mathbf{k}) e^{i\mathbf{k}\cdot\mathbf{R}}
$$

$$
+ \frac{1}{2} \sum_{\substack{\mathbf{k},\mathbf{k}' \\ r,r'}} \mathcal{G}_r(\mathbf{k}) \mathcal{G}_{r'}(\mathbf{k}') e^{i(\mathbf{k}+\mathbf{k}')\cdot\mathbf{R}}.
$$

(B.32)

The diffraction intensity is then contributed from terms of different order $\mathcal{O}(N)$ as

$$
I(\mathbf{q}) = I_o(\mathbf{q}) + I_1(\mathbf{q}) + I_2(\mathbf{q}) + \dots,
$$

(B.33)

where

$$I_o(\mathbf{q}) = Ne^{-2W(\mathbf{q})} \sum_R e^{i\mathbf{q}\cdot\mathbf{R}}$$

$$I_1(\mathbf{q}) = Ne^{-2W(\mathbf{q})} \sum_R e^{i\mathbf{q}\cdot\mathbf{R}} \sum_{\mathbf{k},r} \mathcal{G}_r(\mathbf{k})e^{i\mathbf{q}\cdot\mathbf{R}}$$

$$I_2(\mathbf{q}) = \frac{N}{2}e^{-2W(\mathbf{q})} \sum_{\mathbf{R}} e^{i\mathbf{q}\cdot\mathbf{R}} \sum_{\substack{\mathbf{k},\mathbf{k}'\\r,r'}} \mathcal{G}_r(\mathbf{k})\mathcal{G}_{r'}(\mathbf{k}')e^{i(\mathbf{k}+\mathbf{k}')\cdot\mathbf{R}}.$$

(B.34)

The first-oder term can be straightforwardly evaluated using the identity $\sum_{\mathbf{k}} f(\mathbf{k})\delta_{\mathbf{k}-\mathbf{q}} = f(\mathbf{q})$ as

$$
\begin{aligned}
I_1(\mathbf{q}) &= Ne^{-2W(\mathbf{q})} \sum_{\mathbf{k},r} \mathcal{G}_r(\mathbf{k}) \sum_{\mathbf{R}} e^{i(\mathbf{q}+\mathbf{k})\cdot\mathbf{R}} \\
&= N^2 e^{-2W(\mathbf{q})} \sum_{\mathbf{k},r} \mathcal{G}_r(\mathbf{k})\delta_{\mathbf{q}+\mathbf{k},\mathbf{G}} \\
&= N^2 e^{-2W(\mathbf{q})} \sum_r \mathcal{G}_r(\mathbf{q}-\mathbf{G}) \\
I_1(\mathbf{q}) &= \frac{N}{m}e^{-2W(\mathbf{q})} \sum_r \left|\mathbf{q}\cdot\mathbf{a}^{(r)}(\mathbf{q}-\mathbf{G})\right|^2 \frac{\langle E_r(\mathbf{q}-\mathbf{G})\rangle}{\omega^{2(r)}(\mathbf{q}-\mathbf{G})}.
\end{aligned}
$$

(B.35)

Similarly, the second-oder term is

$$
\begin{aligned}
I_2(\mathbf{q}) &= \frac{N}{2}e^{-2W(\mathbf{q})} \sum_{\substack{\mathbf{k},\mathbf{k}'\\r,r'}} \mathcal{G}_r(\mathbf{k})\mathcal{G}_{r'}(\mathbf{k}') \sum_R e^{i(\mathbf{k}+\mathbf{k}'+\mathbf{q})\cdot\mathbf{R}} \\
&= \frac{N^2}{2}e^{-2W(\mathbf{q})} \sum_{\substack{\mathbf{k},\mathbf{k}'\\r,r'}} \mathcal{G}_r(\mathbf{k})\mathcal{G}_{r'}(\mathbf{k}')\delta_{\mathbf{q}+\mathbf{k}+\mathbf{k}',\mathbf{G}} \\
&= \frac{N^2}{2}e^{-2W(\mathbf{q})} \sum_{\mathbf{k},r} \sum_{r'} \mathcal{G}_r(\mathbf{k})\mathcal{G}_{r'}(\mathbf{G}-\mathbf{k}-\mathbf{q}).
\end{aligned}
$$

(B.36)

That is

$$
\begin{aligned}
I_2(\mathbf{q}) = {}&\frac{1}{2m^2}e^{-2W(\mathbf{q})} \sum_{\mathbf{k},r} \sum_{r'} \left|\mathbf{q}\cdot\mathbf{a}^{(r)}(\mathbf{k})\right|^2 \left|\mathbf{q}\cdot\mathbf{a}^{(r)}(\mathbf{G}-\mathbf{k}-\mathbf{q})\right|^2 \\
&\frac{\langle E_r(\mathbf{k})\rangle}{\omega^{2(r)}(\mathbf{k})} \frac{\langle E_{r'}(\mathbf{G}-\mathbf{k}-\mathbf{q})\rangle}{\omega^{2(r)}(\mathbf{G}-\mathbf{k}-\mathbf{q})}.
\end{aligned}
$$

(B.37)

The evaluation of the second term is more complicated because it involves two nested summation over the Brillouin zone. However, the numerical calculation can be carried out

straightforwardly using modern mathematical software. The theoretical prediction of the diffraction pattern of Gum Metal in Fig.(2.6) is evaluated up to the first-oder term. Numerical results show that the second-order is small compared to the zero- and first-order term.

Bibliography

[1] J. P. Hirth and H. Lothe. *Theory of Dislocations*. John Wiley and Sons, 1971.

[2] A. G. Khachaturyan. *Theory of Structural Transformation in Solids*. John Wiley and Sons, 1983.

[3] T. Mura. *Micromechanics of Defects in Solids*. Springer, 1987.

[4] S. Li and G. Wang. *Introduction to Micromechanics and Nanomechanics*. World Scientific Publishing Company, 2008.

[5] W. Kohn and L. J. Sham. *Phys. Rev.*, 140:A1113, 1965.

[6] T. Li, J. W. Morris, Jr., N. Nagasako, S. Kuramoto, and D. C. Chrzan. *Phys. Rev. Lett.*, 98:105503, 2007.

[7] Y. Hanlumyuang, P. A. Gordon, T. Neeraj, and D. C. Chrzan. *Acta Mat.*, 58:5481, 2010.

[8] T. Saito, T. Furuta, J. H. Hwang, S. Kuramoto, K. Nishino, and et al. N. Suzuki. *Science*, 300:464, 2003.

[9] M. K Miller. *Micro. Res. and Tech.*, 69:359, 2006.

[10] H. Jónsson, G. Mills, and K.W. Jacobsen. *Classical and Quantum Dynamics in Condensed Phase Simulations*. World Scientific, 1998.

[11] J. W. Morris, Jr., Y. Hanlumyuang, M. Sherburne, E. Withey, D.C. Chrzan, S. Kuramoto, Y. Hayashi, and M. Hara. *Acta Mat.*, 59(9):3271, 2010.

[12] M. Y. Gutkin, T. Ishizaki, S. Kuramoto, and I. A. Ovid'ko. *Acta Mater.*, 54:2489, 2006.

[13] R. J. Talling, R. J. Dashwood, M. Jackson, and D. Dye. *Acta Mat.*, 57:1188, 2009.

[14] E. A. Withey, J. M. Minor, S. Kuramoto, D. C. Chrzan, and J.W. Morris, Jr. *Mater. Sci. Eng. A*, 493:26, 2008.

[15] E. A. Withey, A. M. Minor, D. C. Chrzan, J.W. Morris, Jr., and S. Kuramoto. *Acta Mater.*, 58:2652, 2010.

[16] R. M. Martin. *Electronic Structure: Basic Theory and Practical Methods.* Cambridge University Press, 2004.

[17] M. Born and K. Huang. *Dynamical Theory of Crystal Lattice.* Oxford University Press, 1954.

[18] A. A. Maradudin, E.W. Montroll, and G. H. Weiss. *Theory of Lattice Dynamics in The Harmonic Approximation.* Academic Press, 1963.

[19] D. De Fontaine. *Acta Met.*, 18:275, 1970.

[20] P. Brüesch. *Phonons: Theory and Experiement I.* Springer-Verlag, 1982.

[21] R. P. Feynman. *Statistical Mechanics.* Westview Press, 1998.

[22] D. DeFontaine. *Solid State Phys.*, 34:73, 1979.

[23] N. W. Ashcroft and N. D. Mermin. *Solid State Physics.* Thomson Learnin, Inc., 1976.

[24] K. M. Ho, C. L. Fu, and B. N. Harmon. *Phys. Rev. B*, 29:1575, 1984.

[25] P. Giannozzi, S. Baroni, N. Bonini, and et. al. *J. of Phys. Cond. Matt.*, 21:395502, 2009.

[26] W. G. Burgers. *Physica (Amsterdam)*, 1:561, 1934.

[27] A. F. Wright and D. C. Chrzan. *Phys. Rev. Lett.*, 70:1964, 1993.

[28] Y. Y. Ye, C. T. Chan, K. M. Ho, and B. N. Harmon. *Interational Journal of High Performace Computing Applications*, 4:111, 1990.

[29] D. F. Johnson and E. A. Carter. *The Journal of Chemical Physics*, 128:104703, 2008.

[30] L. Pizzagalli, P. Beauchamp, and H. Jonsson. *Phi. Mag.*, 91:88, 2008.

[31] V. Fock. *Z. Phys.*, 63:855, 1930.

[32] R. P. Feynman. *Phys. Rev.*, 56(4):340–343, 1939.

[33] O. H. Nielsen and Richard M. Martin. *Phys. Rev. Lett.*, 50(9):697–700, Feb 1983.

[34] O. H. Nielsen and Richard M. Martin. *Phys. Rev. B*, 32(6):3780–3791, Sep 1985.

[35] O. H. Nielsen and Richard M. Martin. *Phys. Rev. B*, 32(6):3792–3805, Sep 1985.

[36] S. Li. Class notes in computational statistical nao-mechanics. University of California, Berkeley, 2011.

[37] L. D. Landau and E. M. Lifshitz. *Theory of Elasticity.* Butterworth Heinemann, 1997.

[38] D. C. Wallace. *Thermodynamics of Crystals.* Dover, 1998.

[39] M. Parrinello and A. Rahman. *Phys. Rev. Lett.*, 45(14):1196–1199, 1980.

[40] M. Parrinello and A. Rahman. *Journal of Applied Physics*, 52:7182–7190, 1981.

[41] H. Hellmann. *Einföhrung in die Quantenchemie*, page 285, 1937.

[42] W. Luo, D. Roundy, M. L. Cohen, and J. W. Morris Jr. *Phys. Rev. B*, 66:094110, 2002.

[43] R. J. Gooding, Y. Y. Ye, C. T. Chan, K. M. Ho, and B. N. Harmon. *Phys. Rev. B*, 16:13626, 1991.

[44] E. Y. Tonkov and E.G. Ponyatovsky. *Phase Transformations of Elements Under High Pressure.* CRC press, 2004.

[45] D. L. Moffat and D. C. Larbalestier. *Met. Trans. A*, 19A:1677, 1987.

[46] A. W. Cochardt, G. Schoeck, and H. Wiedersich. *Acta Metall.*, 3:533, 1955.

[47] D. J. Bacon. *Script. Metall.*, 3:735, 1969.

[48] R. M. Douthwaite and J.T. Evans. *Script. Metall.*, 7:1019, 1973.

[49] Emmanuel Clouet, Sbastien Garruchet, Hoang Nguyen, Michel Perez, and Charlotte S. Becquart. *Acta Mat.*, 56(14):3450 – 3460, 2008.

[50] A. H. Cottrell and M. A. Jaswon. *Proc. R. Soc.*, A199:104, 1949.

[51] Liu Cheng, A. Bttger, Th.H. de Keijser, and E.J. Mittemeijer. *Script. Metall.*, 24(3):509 – 514, 1990.

[52] M. L. Bernshtein, L. M. Kaputkina, and S. D. Prokoshkin. *Phys. Met. Meall.*, 52:127, 1981.

[53] M. C. Cadeville, J. M. Friedt, and C. Lerner. *J. Phys. F: Metal Phys.*, 7:123, 1977.

[54] E. Ohman. *JISI*, 130:445, 1931.

[55] J. D. Eshelby. *Solid State Phys.*, 3:79, 1956.

[56] J.D. Eshelby. *Prog. in Solid Mech.*, 2:89, 1961.

[57] E. Kroner. *Physics of Defects*. North-Holland Pub. Co., 1981.

[58] T. Mura. *Adv. in Mat. Res.,*, 3:1, 1968.

[59] Murray S. Daw. *Com. Mat. Sci.*, 38(2):293 – 297, 2006.

[60] A. G. Khachaturyan, S. Semenovskaya, and T. Tsakalakos. Elastic strain energy of inhomogeneous solids. *Phys. Rev. B*, 52(22):15909–15919, Dec 1995.

[61] D. Y. Li and L. Q. Chen. *Acta Mat.*, 45(6):2435 – 2442, 1997.

[62] D. Y. Li and L. Q. Chen. *Acta Mat.*, 46(2):639 – 649, 1998.

[63] G. Kresse and J. Furthmuller. *Phys. Rev. B*, 54(16):11169–11186, Oct 1996.

[64] D. M. Clatterbuck, D. C. Chrzan, and J. W. Morris, Jr. *Acta Mat.*, 51(8):2271 – 2283, 2003.

[65] J. A. Rayne and B. S. Chandrasekhar. *Phys. Rev.*, 122(6):1714–1716, Jun 1961.

[66] A. N. Stroh. *J. Math. Phys.*, 41:77, 1962.

[67] Murray S. Daw and M. I. Baskes. *Phys. Rev. Lett.*, 50(17):1285–1288, Apr 1983.

[68] Murray S. Daw and M. I. Baskes. *Phys. Rev. B*, 29(12):6443–6453, Jun 1984.

[69] R. Chang. *Fundamental aspects of dislocation theory*, volume 317, page 299. NBS Special Publication, Gaithersburg, MD, 1970.

[70] J. T. M. De Hosson. *Solid State Commun.*, 17:747, 1975.

[71] X. Shu and C. Wang. *Mat. Sci. Forum*, 1865:561, 2007.

[72] K. Tapasa, Y. N. Osetsky, and D. J. Bacon. *Acta Mat.*, 93:55, 2007.

[73] C.S. Becquart, J.M. Raulot, G. Bencteux, C. Domain, M. Perez, S. Garruchet, and H. Nguyen. *Com. Mat. Sci.*, 40(1):119 – 129, 2007.

[74] N. Louat. *Proc. Phys. Soc. Lond.*, B69:459, 1956.

[75] D. N. Beshers. *Acta Metall.*, 6:521, 1958.

[76] J. M. Ziman. *Principles of the Theory of Soids*. Cambridge University Press, 1979.